THE ACOUSTIC WAVE SENSOR AND SOFT LITHOGRAPHY TECHNOLOGIES FOR CELL BIOLOGICAL STUDIES

by

Fang Li

BS, Tsinghua University, P.R. China, 1999

MS, Tsinghua University, P.R. China, 2002

MS, University of Pittsburgh, 2004

Submitted to the Graduate Faculty of

the Swanson School of Engineering in partial fulfillment

of the requirements for the degree of

Doctor of Philosophy

University of Pittsburgh

2008

UNIVERSITY OF PITTSBURGH

SWANSON SCHOOL OF ENGINEERING

This dissertation was presented

by

Fang Li

It was defended on

May 27, 2008

and approved by

Co-Director: Dr. James H.-C. Wang, Associate Professor, Orthopeadic Surgery and Mechanical Engineering and Material Science

Dr. William S. Slaughter, Associate Professor, Mechanical Engineering and Material Science

Dr. Patrick Smolinski, Associate Professor, Mechanical Engineering and Material Science

Dissertation Director: Dr. Qing-Ming Wang, Associate Professor, Mechanical Engineering and Material Science

THE ACOUSTIC WAVE SENSOR AND SOFT LITHOGRAPHY TECHNOLOGIES FOR CELL BIOLOGICAL STUDIES

Fang Li, PhD

University of Pittsburgh, 2008

Recently, cell-based biosensors have attracted many attentions because of their potential applications in fundamental biological research, drug development, and other fields. Acoustic wave biosensors offer powerful tools to probe cell behaviors and properties in a non-invasive, simple, and quantitative manner. Current studies on cell-based acoustic wave sensors are focused on experimental investigation of thickness shear mode (TSM) sensors for monitoring cell attachment and spreading. There are no theoretical models for cell-based TSM biosensors. No studies on other cell biological applications of TSM sensors or on surface acoustic wave cell-based biosensors have been performed. The reliability and sensitivity of current cell-based biosensors are low. Improving them requires studies on engineering cells and understanding the effects of cell morphology on cell function.

The overall objective of this dissertation is to develop acoustic wave sensor systems for cell biological studies and to determine the effects of cell shape on cell function. Our study includes three parts: (1) Development of cell-based TSM sensor system; (2) Studies of Love mode devices as cell-based biosensors; (3) Studies of the effects of cell shape on cell function. In the first part, a theoretical model was developed, changes in cell adhesion were monitored and cell viscoelasticity was characterized by TSM sensor systems. The TSM sensor systems were demonstrated to provide a non-invasive, simple, and reliable method to monitor cell adhesion and characterize cell viscoelasticity. In the second part, a theoretical model was developed to

determine signal changes in Love mode sensors due to cells attaching on their surface. Experimental results validated the model. In the third part, cell shape was patterned to different aspect ratios. Elongated tendon cells were found to express higher collagen type I than shorter cells. Changes in cell shape induced alterations in cytoskeleton, focal adhesions, and traction forces in cells, which may collectively prompt the observed differential collagen type I expression in cells with different shapes. Overall, our research expanded the applications of acoustic wave cell-based biosensors. Studies on cell shape control and the effects of cell shape on cell function will be useful for increasing the sensitivity of cell-based biosensors in future research.

TABLE OF CONTENTS

LIST OF TABLES

LIST OF FIGURES

PREFACE

During my study at the University of Pittsburgh, I have received a lot of support and help from many people. I would like to take this opportunity to thank them.

First and foremost, I would like to thank my advisers, Prof. Qing-Ming Wang and Prof. James H.-C. Wang, for offering me such a great interdisciplinary project and giving me a unique training in the fields of mechanical engineering and cell biology. They always support and help me in every possible way professors can help their students. From them, I not only learned how to do excellent research, but also be a nice person. It is really a great experience to work with them. Thank you very much! I would like to thank my other committee members, Prof. William S. Slaughter and Prof. Patrick Smolinski, for their being on my committee, their support and all the useful discussions. I would like to thank Dr. Minking K. Chyu for his support and advice in my job search.

Special thanks to Dr. Bin Li in the mechanobiology laboratory for giving me so much help and support on cell patterning project. Mr. Lifeng Qin helped me a lot in terms of the testing of acoustic wave sensors. I appreciate it very much! I also would like to thank other members in Microsensor and Microactuator Laboratory for their help and discussion regarding the fabrication and testing of sensors and actuators and other members in Mechanobiology Laboratory for giving me so much support in learning cell culture, RT-PCR, immunoassaying and other cell biology techniques.

I would like to thank all the friends I have made at the University of Pittsburgh for their wonderful friendship.

At last, I would like to thank the most important people in my life: my father Li Xuelin, my mother Shuai Yeying, my sister Li Hui and my husband Mao Wei. Thank you so much for everything you have done for me. Without you, I could accomplish nothing.

1.0 BACKGROUND

Due to the potential applications in various areas and advantages over non-living sensors, cell-based biosensors attract more and more attentions. However, current research on cell-based biosensors is still in the early stage. The promise of cell-based sensing for drug discovery, diagnostics, tissue engineering and pathogen detection is far from being realized [1]. In this dissertation, we did two parts of work on the development of cell-based biosensors. First, we developed acoustic wave sensor systems for cell biological studies. Second, we precisely controlled cell shape using soft lithography techniques and investigated the effect of cell shape on cellular function, which provides insight into the "design criteria" for engineering of a hybrid interface that preserves biological responses of interest and is crucial to increasing the sensitivity of cell-based biosensors. In this chapter, background information on these two topics will be reviewed first.

1.1 SENSORS, BIOSENSORS AND CELL-BASED BIOSENSORS

A sensor is a device that responds to a stimulus and generates a signal that can be measured [2]. The stimulus could be physical, chemical or biological and the output signal is usually electrical one that can be processed by electrical devices, such as an analog current or voltage, a stream of digital voltage pulses, or an oscillatory voltage with amplitude, frequency and phase related to

the value of input quantity [2]. Sensors can be categorized into different classes, based on different standards. For example, according to the applications or the physical quantities that can be measured by sensors, they can be classifies as position sensors, force sensors, strain sensors, pressure sensors, temperature sensors, chemical sensors, biosensors, etc. According to the type of energy transfer they detect, they can be classified as mechanical sensors, optical sensors, magnetic sensors, thermal sensors, radiant sensors, acoustic sensors, etc [3]. In this dissertation, our research focus is on biosensors.

Biosensors (**Figure 1**) are those devices combining the biological sensing elements (such as microorganisms, enzymes, antibodies, antigens, nuclear acids, cells, etc) with physicochemical transducers (including optical, electrochemical, thermometric, piezoelectric or magnetic transduction systems) to detect biological events/elements (e.g., cell behavior, enzymes, antigens, and nuclear acids) [4]. In the past twenty years, biosensor research has grown rapidly with the development of the biochemistry, molecular biology, immunochemistry, and the development in fiber optics and microelectronics [5]. Biosensors have exhibited potential applications in the areas of biomedicine, bacterial and viral analysis, and cellular and molecular pharmacology. Various sensor technologies can be used to implement the biosensor platforms, including microelectronics and electrical technology, optical technology, acoustic wave technology, electrochemical technology, etc [3].

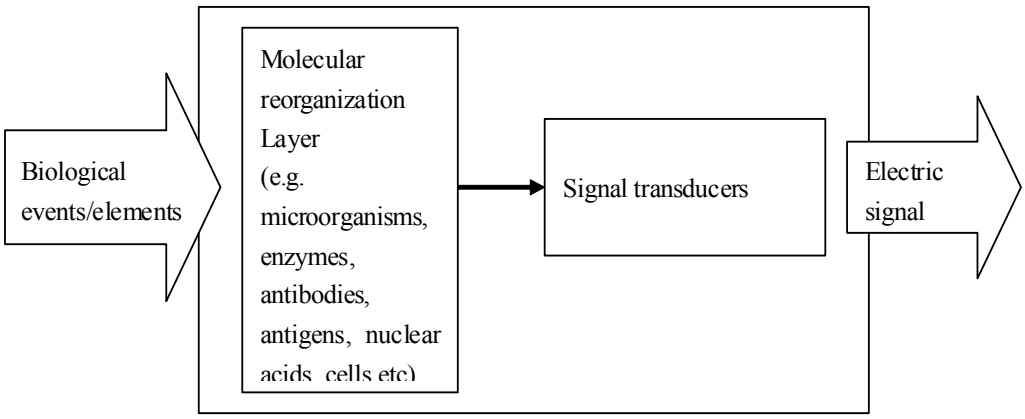

Figure 1. Principle of biosensors.

Cell-based biosensors are sensors combined with living cells. Compared with non-living sensors, cell-based sensors offer a lot of potential advantages. For example, they are able to detect unanticipated threats; they can relate the measurement data to cell pathology and physiology; they enhance the stability of enzymes, receptors, or antibodies in biological systems. The applications of cell-based biosensors are potentially extensive. First, by treating cells as the research objectives, cell-based biosensors can be used in a lot of fundamental biological research. Second, cells are the sensitive elements that are able to sense various biophysical or biochemical signals and transduce them into changes in cell behaviors or properties that can be measured by biosensor systems. So cell-based biosensors can be used for drug development (assess the efficacy and toxicity of candidate drugs), medical diagnostics (predict clinical outcome), cell-based therapy, detection of chemical and biological agents, etc [1]. Current research on cell-based biosensors is still in the early stage. There are a lot of challenges on the development of cell-based biosensors: (1) Cells are environmentally sensitive. Cells must be cultured in the viable and sterile environment. (2) The inherent viability in cells is large. Even for the genotypically identical organisms, they differ from each other. The variability could be induced

by differences in the cellular micro-environment, protein expression, receptor number and other factors. Therefore, in order to obtain producible results, engineering the living/non-living interface is crucial. (3) The relationship between input and output signals is hard to define. Controlling over variability in the microenvironment of cells preserves biological responses of interest and is crucial to increasing the sensitivity of cell-based biosensors. (4) Transduction of cellular output to the signals that can be measured and analyzed is complex. Therefore, development of innovative sensing technologies is crucial. Based on the above challenges, in this dissertation, we applied acoustic wave devices for cell biological studies and precisely controlled the adhesive islands' shape using soft lithography techniques.

1.2 ACOUSTIC WAVE SENSORS

As its name implies, an acoustic wave sensor is based on the transduction mechanism between electrical and acoustic energies [2]. In acoustic wave devices, the acoustic waves propagate through or on the surface of the device. The velocity and amplitude of the acoustic wave can be altered by the changes in the acoustic wave propagation pathway, including the mass changes and viscoelasticity changes in materials bounded on the device surface, and force changes applied on the device surface. Therefore, acoustic wave devices as sensors have been used to measure gas or protein concentration, the thickness of thin film, liquid viscosity, polymer viscoelasticity, etc [6, 7]. The acoustic waves can be generated by piezoelectric, magnetostrictive, electrostrictive, photothermal, and other mechanisms, but most acoustic wave devices are based on piezoelectric crystals, such as quartz crystal and ZnO [8]. In this section, first, a brief overview of the fundamental background on acoustic wave devices will be given, including

piezoelectricity, acoustic wave in elastic media, device configurations and the measuring techniques. Then, classification and comparison of acoustic wave sensors will be described. Finally, the TSM and Love mode acoustic wave sensors that will be used in this study will be reviewed.

1.2.1 General Background

Piezoelectricity

Most of the acoustic wave sensors are based on piezoelectric mechanism. The piezoelectricity exists in the crystals that lack a center of inversion symmetry. The definition of piezoelectricity is that the electrical charges on opposing surfaces of a solid material are generated when torsion, pressure, bending, etc. are applied along an appropriate direction. Conversely, the application of the polarizing electric field may cause mechanical deformations, which is called the "converse piezoelectric effect". The piezoelectric effect reflects the coupling between the mechanical energy and the electric energy domain of the material.

Piezoelectric constitutive equations are developed to describe the electrical and mechanical interactions in piezoelectric materials. Four sets of piezoelectric constitutive equations are commonly used. In matrix notation, these equations can be written as follows [9]:

$$\begin{cases} T = c^D S - h^{'} D \\ E = -hS + \beta^s D \end{cases} \tag{1.1a}$$

$$\begin{cases} S = s^E T + d^{'} E \\ D = dT + \varepsilon^T E \end{cases} \tag{1.1b}$$

$$\begin{cases} S = s^D T - g^{'} D \\ E = -gT + \beta^T D \end{cases} \tag{1.1c}$$

$$\begin{cases} T = c^E S + e^{'} E \\ D = eS + \varepsilon^S E \end{cases} \tag{1.1d}$$

where the matrixes with superscript "'" are transpose of these matrixes, T is stress tensor, S is strain tensor, D is electrical displacement tensor, and E is electric-field intensity tensor. In these constitutive equations, there are twelve different constants. Their physical meanings are as follows: c^D and c^E are the stiffness coefficient tensors under the condition of a constant electric displacement and electric-field intensity, respectively; s^D and s^E are compliance coefficient tensors under the condition of a constant electrical displacement and electric-field intensity, respectively; h is the piezoelectric charge coefficient tensor; d is the piezoelectric strain coefficient tensor; g is the piezoelectric voltage coefficient tensor; e is the piezoelectric stress coefficient tensor; ε^T and ε^S are permittivity tensors under the condition of a constant stress and strain respectively; and β^T and β^S are permittivity tensors under the condition of a constant stress and strain respectively.

Acoustic Wave in Elastic Media

A general approach to theoretically describe acoustic wave propagation is based on solving a set of wave equations by applying boundary conditions between different layers. It is necessary to describe the wave equations for non-piezo and piezoelectric materials here. Based

on the Newton's second law of motion and the elastic constitutive equation, the wave equation for a non-piezoelectric solid can be derived as follows [8]:

$$C_{ijkl}\, u_{k,li} + \eta_{ijkl}\, \dot{u}_{k,li} = \rho_m\, \ddot{u}_j \tag{1.2}$$

where C_{ijkl} and η_{ijkl} are the fourth-rank elastic coefficient tensor and the fourth-rank viscoelastic coefficient tensor. For piezoelectric materials, the wave equation becomes

$$e_{ijk}\, \phi_{,ki} + C_{ijkl}\, u_{k,li} + \eta_{ijkl}\, \dot{u}_{k,li} = \rho_m\, \ddot{u}_j \tag{1.3}$$

where e_{ijk} is the third-rank piezoelectric stress coefficient tensor.

According to the directions of particle displacement and wave propagating, acoustic waves are classified into shear wave and compressive wave. In a shear wave, the wave propagation is normal to the particle displacement, while in the compressive wave, the particle motion is in the same direction as the wave propagation [8].

Device Configurations

The configurations of acoustic wave devices include type and geometry of transducers and the electronic circuitry that is connected to the transducers. According to the number of the transducers, acoustic wave device can be classified into two main categories: one-port and two-port devices [2].

One common example of the one-port device is the bulk resonator **(Figure 2)**. Bulk waves are propagating through the whole substrate. They are generally excited by the parallel electrodes coated on both sides of the excited volume of a piezoelectric material. The input and output ports are both served by the parallel electrodes on both sides. The surface acoustic wave (SAW) resonators could be one-port device also. The details of the SAW resonators are given in the next paragraph.

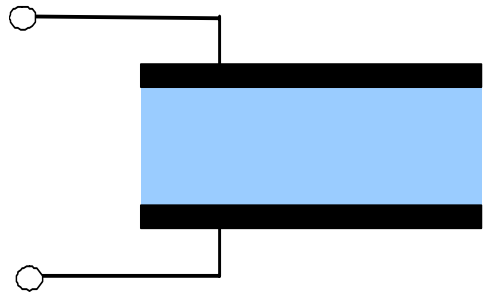

Figure 2. Structure of bulk acoustic wave resonator..

The examples of two-port devices are the SAW delay lines and resonators. In SAW device, the acoustic wave propagation is confined to the surface. Usually, a surface acoustic wave is excited on the piezoelectric crystal using lithographically patterned interdigital transducers (IDTs) (**Figure 3**). The relative signal levels and phase delay between input and output ports constitute two responses. When an alternative voltage is applied between alternately connected electrodes, a periodic strain field is generated in the piezoelectric crystal underneath. Thus, an acoustic wave perpendicular to the finger direction is excited by each finger pair. Interference results in a maximum SAW magnitude if

$$f_n = \frac{2n+1}{\lambda} v \tag{1.4}$$

with the excitation frequency f, and the acoustic wave velocity v of the particular mode.. Therefore, the frequency is determined by the geometry of IDTs.

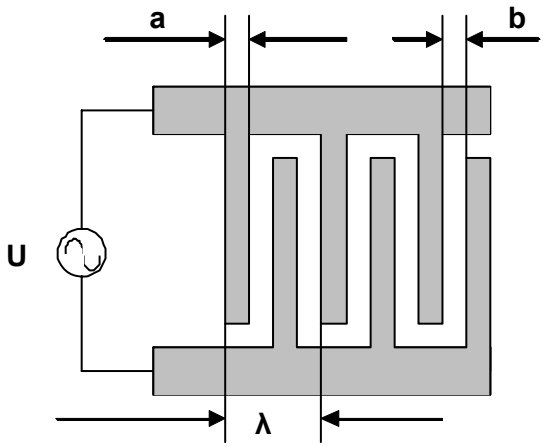

Figure 3. Interdigital transducer, formed by patterning electrodes on the surface of piezoelectric materials for the excitation of surface acoustic waves [2, 10]

The SAW resonators may be either one-port or two-port devices **(Figure 4A)**, in which one or two IDTs are enclosed between two reflectors [2, 10]. For the one-port resonator, its properties are much like those of the bulk resonators. Delay lines (**Figure 4B**) are always two-port devices having two IDTs deposited on the piezoelectric substrate with center to center distance equal to a whole number of wavelengths. Compared with delay lines, the advantage of resonators is that the insertion loss of the resonator is smaller, which decreases influence of the phase noise on the measurement and results in an improved sensor resolution. However, in contrast to delay lines, the phase characteristics of resonators are widely nonlinear and dependent on damping. In addition, the sensor reaction to different external signals is very complex. Hence it becomes difficult to separate the effects of different physical quantities. Another disadvantage of typical resonators is that additional device area is needed for the reflective elements. Therefore, in most cases, delay lines are used in sensing applications.

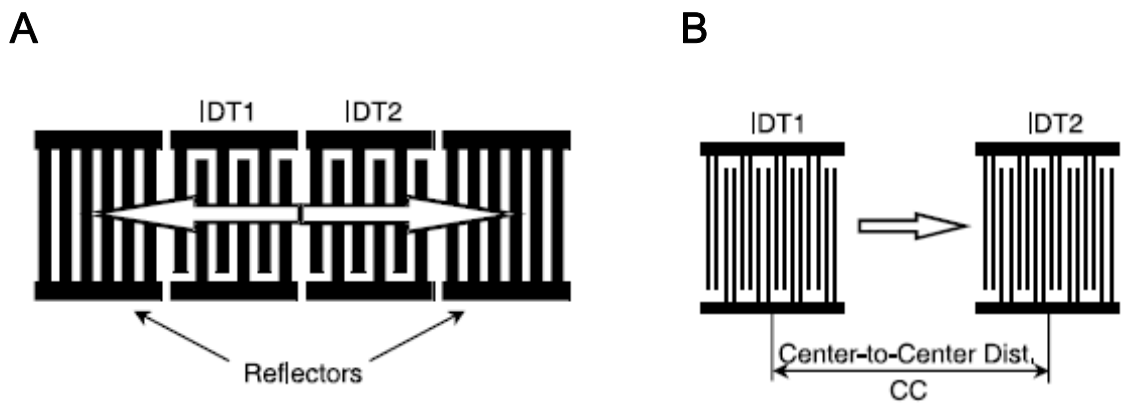

Figure 4. Geometry of two-port SAW devices: Two-port SAW resonator (A) and delay lines (B) [10].

Measurement Techniques

Basically, there are two kinds of techniques for measurements of acoustic wave devices: oscillator-based measurements and phase/amplitude-based measurements [8].

The oscillator circuit (**Figure 5**) has to be satisfied two conditions in order to maintain a continuous oscillation. If we assume the impedance of acoustic device is Z, the loop gain condition is as follows:

$$\left|\left(\frac{Z}{Z+R}\right)\cdot A\right| = |\beta A| = 1 \tag{1.5}$$

The loop phase condition for the oscillation is

$$\arg(\beta A) = 2n\pi \tag{1.6}$$

In real circuits, the loop gain may be larger than unity. An amplifier with automatic gain control (AGC) can adjust the loop gain to maintain a value of unity [11]. Moreover, changes in the insertion loss can be monitored by means of the AGC control voltage [9].

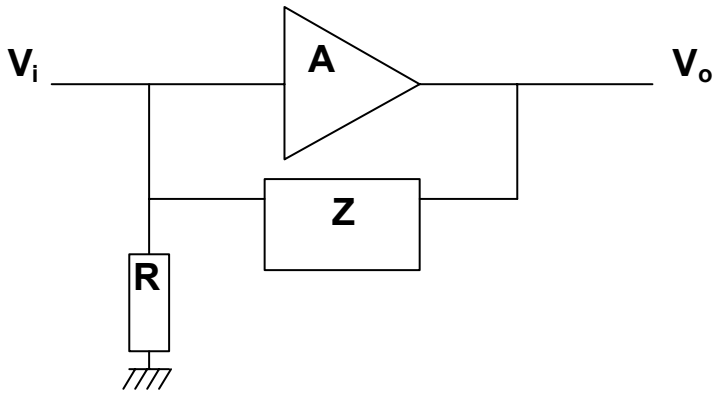

Figure 5. Oscillation circuit of bulk acoustic wave (BAW) and surface acoustic wave (SAW) devices.

In the SAW device, the dual delay line configuration is widely used. The signal of the sensor is mixed with a reference one through a mixer, resulting in a low-frequency signal. Therefore, common influences to both oscillators, such as temperature changes, are eliminated. The low-pass filter is required to eliminate the sum of the frequencies and other higher harmonic products after the mixer. Using this dual delay line configuration, the frequency shift of the sensor can be detected with eliminating the influences of temperature, aging etc.

For the in-depth device characterization, a network analyzer (NWA) is an ideal tool. Compared with an oscillator setup, the influence of an NWA itself on the measurement can be ignored. A measurement of the scattering parameters S_{ij} provides a complete characterization of two-port devices such as resonators or delay lines (scattering parameters S_{ij} are a set of parameters describing an electrical two-port device; *S* parameters give a measure of the ratio of the amplitudes of the incident and the reflected electromagnetic waves at both ports). The forward-scattering parameter S_{21} is a measure of the ratio of the outward traveling wave at port 2 to the incident voltage at the port 1 (**Figure 6A**). The reflection coefficient S_{11} describes the ratio of incident and reflected voltages at the port 1 (**Figure 6B**). In order to characterize a single IDT or a one-port resonator, e.g., TSM resonator, S_{11} may be transformed into the impedance or

admittance domain. To avoid unwanted influences of reflected acoustic waves from neighboring edges or transducers, those structures should be thoroughly covered with an absorbing material. In addition, a one-port resonator can be measured by impedance analyzer, shown in **Figure 6C**.

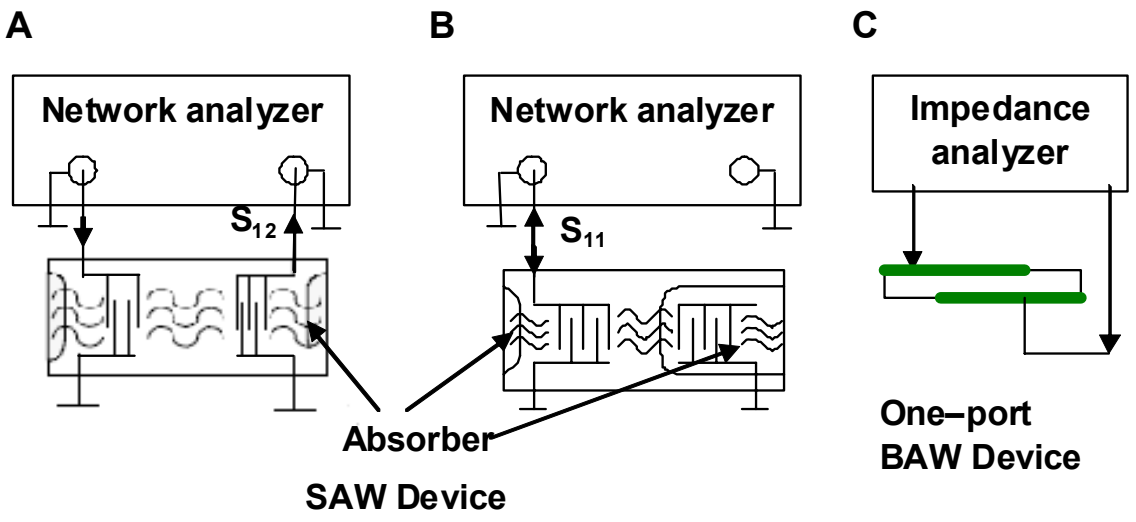

Figure 6. Devices characterized with network analyzer by measuring forward-scattering parameter S_{21} (A) the reflection coefficient S_{11} (B) and a one-port resonator is characterized by impedance analyzer (C) [10]

1.2.2 Classifications and Comparisons of Acoustic Wave Sensors

In the previous sections, we have discussed some general background on acoustic wave devices. In this section, the classifications of acoustic wave sensors will be discussed and we will compare the different acoustic wave sensors then. The acoustic wave sensors can be grouped into several classes according to different mechanisms. For example, according to the geometric shape of the sensor, one can differentiate between acoustic modes in a half-space (solid with one free boundary), a plate (solid with two boundaries), layered structures (half-space with parallel layers), and bulk modes (solid restricted in all dimensions), while according to the direction of

polarization of particle motion relative to the device surface, the acoustic wave sensors can be categorized into sagittal polarization, shear-horizontal polarization and longitudinal polarization sensors (**Table 1**).

Table 1. Classification of acoustic wave sensors [10]

	sagittal polarization	shear-horizontal polarization	longitudinal polarization
Half-space	Rayleigh waves	Leaky wave, surface skimming bulk wave (SSBW)	QLL-SAW
Plate	FPW(Lamb wave)	SH-APM	
Layered structures		Love waves	
Bulk mode		TSM	

The geometric shape of the sensor determines the sensitivity to mechanical interactions at the device surface, i.e. mass loading or viscous coupling, which is of primary interest in sensor applications. Generally, the sensitivity is related to the ratio of the square of surface particle velocity to the average density of acoustic energy within the device. Therefore, Rayleigh waves are extremely sensitive since the acoustic energy is essentially confined within a surface region less than one wavelength thick. Furthermore, plate modes tend to become more sensitive with decreasing plate thickness.

The polarization mode determines the possibility of acoustic wave sensors in liquid applications. For example, the well-known Rayleigh waves with the sagittal polarization are not suitable for liquid sensing in most cases since strong attenuation occurs due to the generation of

compression waves into the liquid because of the vertical component of particle motion. This compression wave excitation can be avoided if the wave mode used is slow enough to allow only evanescent waves in the adjacent liquid. Flexural plate mode (FPW) is an example of such waves. Since liquids do not support shear waves, modes exhibiting shear-horizontal polarization can be used in liquid sensing applications. In isotropic materials, there is no shear-polarized true surface wave. However, in the case of a strongly anisotropic piezoelectric crystal, as well as layered structures, surface-localized shear modes can exist, such as Leaky wave, surface skimming bulk wave, Love waves, shear horizontal acoustic plate wave (SH-APM) and so on. Thickness shear mode (TSM) wave, which is a shear-horizontal polarized bulk wave, is widely used in liquid and gas sensing applications.

Table 2 lists selected properties of several acoustic sensors for liquid sensing applications. As discussed, the sensitivity of the devices is related to the geometric shape of the sensor. For the devices with a plate structure or bulk mode, such as Lamb mode, SH-APM and TSM devices, the operating frequency and the sensitivity are relative low. The reason is that improvement of frequency therefore increasing sensitivity demands reducing the membrane thickness, thereby also reducing the mechanical robustness. For half-space structures, the sensitivity is only determined by the working frequency. Although increasing frequency can be obtained by decreasing the IDTs periods, it simultaneously demands more complex RF electronics. However, layered structure, such as Love mode sensor, shows its advantage on the device sensitivity since its sensitivity can be increased up to a certain limit by optimizing the waveguide thickness. This does not affect the mechanical robustness.

Another important properties of devices are the cross sensitivities with respect to changes of other physical quantities, such as pressure or temperature. High mechanical robustness of

devices can reduce pressure-sensitivity. Therefore, the devices with layered or half-space structure have low pressure sensitivity. Temperature sensitivity can be reduced either by choosing a proper crystal cut (TSM, Rayleigh, SSBW) or material system (Love mode). To avoid electrode directly exposed to the liquids, in some devices, e.g. SH-APM, Lamb mode, the electrodes are situated on the surface opposite the liquid contact. Another method is the device surface is covered by an inert functional layer, such as Love wave.

Among these acoustic liquid sensors, TSM device is the simplest and the oldest. It has a simple structure, relatively low fabrication cost and easy measurements due to the low operating frequency. In addition, the theory of TSM device is relatively mature. Therefore, although TSM device has some intrinsic limits such as relatively low sensitivities, it has been widely used as sensors in gas and liquid phases. Love mode acoustic wave sensors have many advantages e.g. high sensitivity, mechanical robustness, and the protection of the IDTs due to the waveguide. Therefore, it is one of the most promising techniques used in liquid phase. However, there are still a lot of unsolved problems for Love mode devices as sensors, such as theoretical modeling, measurements etc. Therefore, in this study, we choose these two modes as cell-based biosensors for cell biological studies.

Table 2. Selected properties of acoustic wave sensors [10]

Property	Love	TSM	SH-APM	Lamb	SSBW, leaky wave
Mode	waveguide	Bulk	Reflected plate	plate	Surface
Polarization	Shear-hor.	Shear-hor.	Shear-hor.	Sagittal	Shear-hor.
Frequency (MHz)	50–500	2–20	50–200	1–10	50–500

Table 2 (continued)

Cross sensitivities	(Electrical liquid properties) (temp.)	Pressure (temp.) electrical liquid properties)	Pressure, electrical liquid properties (temp.)	Pressure, electrical liquid properties (temp.)	Electrical liquid properties (temp.)
Sensitivity determined by	Waveguide thickness Frequency	Plate thickness	Plate thickness	Membrane thickness	Frequency
Frequency determined by	IDT period	Plate thickness	Plate thickness IDT period	Membrane thickness, IDT period	IDT period
Fabrication cost	0	– to 0	+	+	–

–, none/small; 0, intermediate; +, large; ++, very large

1.2.3 Thickness Shear Mode (TSM) Devices

The thickness shear mode (TSM) devices (**Figure 7A**) commonly indicate a thin disk of the AT-cut quartz plate with metal electrodes on both sides. The AT-cut quartz slice is prepared by cutting a quartz crystal with an angle of 35.10 degrees to the optical z-axis (**Figure 7B**). Since the AT-cut quartz crystals show a high temperature stability, this particular cut has become the most suitable one for TSM resonators.

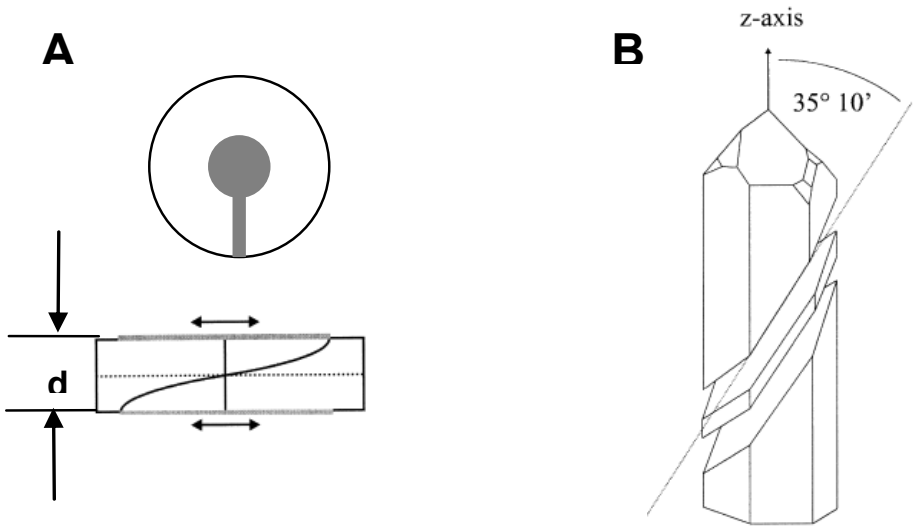

Figure 7. Circular TSM quartz resonator (A). A quartz plate is cut with an angle of 35.10 degrees with respect to the optical z-axis. (B) [10].

Because of the piezoelectricity and the crystalline orientation of the AT-cut quartz plate, the application of a voltage between the two electrodes produces a shear deformation in the plane with the crystal surface (**Figure 7A**). When an alternative voltage is applied between the two electrodes, shear waves of opposite polarity are generated at the either side of the crystal. The resonant condition for the TSM resonator can be determined by tracing the path of one propagating shear wave, which may be thought to start at the top electrode, propagate through the thickness of the quartz thickness, reflect at the bottom surface with phase shift of π, and then return to their origin where it reflects again with phase shift of π. Therefore, the total round-trip phase shift is

$$\phi_r = 2kh + 2\pi \tag{1.7a}$$

$$k = 2\pi / \lambda = \omega / v_s \tag{1.7b}$$

where h is the thickness of the crystal, λ is the acoustic wave length, v_s is the shear wave velocity. When the total phase shift is an integer multiple of 2π, constructive interference of

incident and return waves occurs and results in resonance. Therefore, the mechanical resonance occurs when the thickness of TSM resonator is an odd multiple of half of the acoustic wavelength.

$$h = N(\frac{\lambda}{2}) \tag{1.8}$$

Therefore, the resonant frequency is expressed as:

$$f_N = \frac{Nv_s}{2h} \tag{1.9}$$

TSM resonator can only excite the odd harmonics. At the resonance, a standing shear wave is established with the maximum values of the displacement occurring at the crystal surface, which makes the device sensitive to surface perturbations [2]. Using piezoelectric materials, the mechanical resonances of devices are electrically excited or detected. Therefore, it is necessary to look at the electrical characteristics of TSM resonators to describe the conversion between the mechanical and electric parameters. So far, two types of equivalent-circuit models are used to describe the resonators: the distributed (or transmission line) model and the lumped-element model.

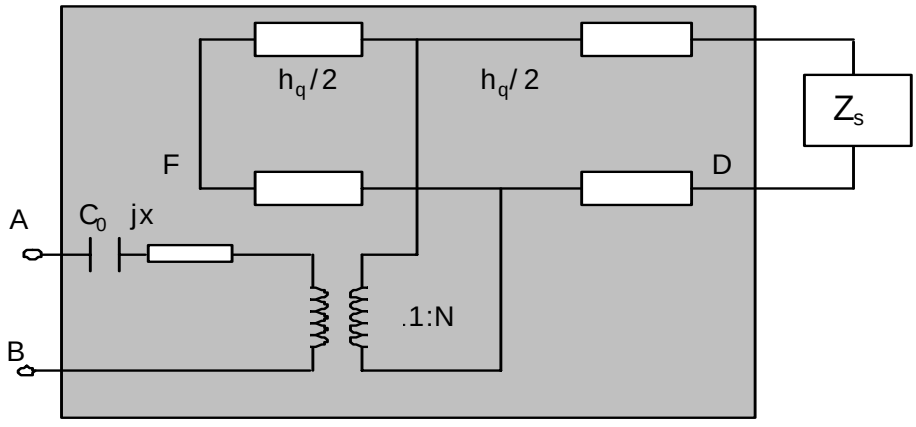

Figure 8. Transmission line model to describe the near-resonant electrical characteristics of the resonator

A transmission line model (TLM) **(Figure 8)** is based on a one-dimensional electromechanical model of acoustic wave generation and propagation in piezoelectric and non-piezoelectric layers [12]. In this model, a piezoelectric material is described by a three-port element, one electric port and two acoustic ports. In the case of the resonators with loading on one side, one acoustic port is considered as a short circuit and the other acoustic port is loaded with mechanical impedance Z_s, representing the surface "loading condition". Therefore, the generalized input electric impedance of resonator sensors can be obtained as

$$Z = \frac{1}{j\omega C_0}\left(1 - \frac{K^2}{\alpha}\frac{2\tan\frac{\alpha}{2} - j\frac{Z_L}{Z_q}}{1 - j\frac{Z_L}{Z_q}\cot\alpha}\right) \tag{1.10}$$

The abbreviations in equation (1.10) are calculated with the following equations:

$$K^2 = \frac{e_q^2}{\varepsilon_q c_q} \tag{1.11a}$$

$$\alpha = \omega h_q \sqrt{\rho_q / c_q} \tag{1.11b}$$

$$Z_q = \sqrt{\rho_q c_q} \tag{1.11c}$$

$$C_0 = \varepsilon_q \frac{A}{h_q} \tag{1.11d}$$

where K^2 is the electromechanical coupling coefficient of quartz, α is the acoustic phase shift in the quartz crystal and Z_{cq} is the characteristic acoustic impedance of the quartz crystal [12].

The electrical impedance can be separated into a parallel circuit consisting of the static capacitance C_o and motional impedance Z_m. According to equation (1.10), the motional impedance Z_m can be written as follows:

$$Z_m = \frac{1}{j\omega C_0}\left(\frac{\frac{\alpha}{K^2}}{2\tan\frac{\alpha}{2}} - 1\right) + \frac{1}{\omega C_0}\frac{\alpha}{4K^2}\frac{Z_L}{Z_q}\frac{1}{1 - j\frac{Z_L}{Z_q \times 2\tan\frac{\alpha}{2}}} = Z_m^0 + Z_m^L \tag{1.12}$$

$Z_m{}^0$ and $Z_m{}^L$ represent the unloaded quartz and the load respectively.

By taking the approximation of $\tan\frac{\alpha}{2} \approx 4\alpha/((N\pi)^2 - \alpha^2)$, the unloaded quartz near the resonant frequency is expressed as

$$Z_m{}^0 = \frac{1}{j\omega C_q} + j\omega L_q + R_q \tag{1.13}$$

For small loads ($\frac{Z_l}{Z_q} << 2\tan\frac{\alpha}{2}$), $Z_m{}^L$ simplifies to

$$Z_m{}^L = \frac{1}{\omega C_0}\frac{\alpha}{4K^2}\frac{Z_L}{Z_q} \tag{1.14}$$

Therefore, for resonators with small loadings, near the resonance frequency, TLM can be transformed into the equivalent circuit with lumped elements, which is called Butterworth-Van-Dyke circuit (**Figure 9**).

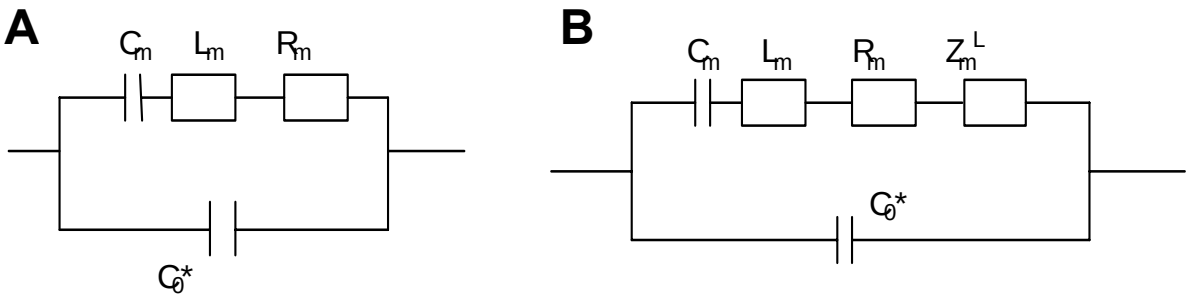

Figure 9. Butterworth-van-Dyke (BVD) equivalent circuit of unperturbed TSM resonator near the series resonant frequency (A); Modified Butterworth-van-Dyke equivalent circuit of TSM resonators with small loadings (B)

In case of the resonators as practical sensors, the parasitic capacitance not only includes the static capacitance C_0 in equation (1.11d), but also includes a capacitance C_p that arises in the test fixture. In the BVD circuits, we use C_0* to represent the parasitic capacitance. The resonance frequency is a critical parameter for TSM resonators in sensing applications. According to BVD circuits, the quartz resonator shows two different resonance frequencies [2]. The series resonant

frequency f_s is defined as the frequency at which the motional reactance is zero. According to the above criterion, for the unperturbed resonator, the series resonance frequency is given by

$$f_s = \frac{1}{2\pi(L_m C_m)^{1/2}} \tag{1.15}$$

The parallel resonance frequency f_p is defined as the frequency at which the total reactance is zero.

$$f_p = \frac{1}{2\pi}\left[\frac{1}{L_m}\left(\frac{1}{C_m} + \frac{1}{C_0 *}\right)\right]^{1/2} \tag{2.16}$$

In the measurement, the series resonance frequency is obtained by measuring maximum value of the in-phase electrical admittance of the resonator G_{max}, while the parallel resonance frequency is the characteristic frequency obtained by using the active oscillator. Equation (1.10) shows the relationship between the input electrical impedance of the resonator and the surface mechanical impedance of the loadings. Therefore, the input electrical impedance provides information about a variety of different material-specific properties, such as mass of thin films, viscoelasticity of liquids or shear moduli of viscoelastic materials. Different surface perturbations have different the surface mechanical impedance (Z_s) **(Table 3)**. According to expressions of the mechanical impedance for different loadings, the mechanical properties of the loading materials can be extracted from the input electrical impedance of the resonators near the resonance.

Table 3 Surface mechanical impedance (Zs) for different surface perturbations

Surface perturbation	Surface mechanical impedance (Z_s)
Unperturbed	0
Ideal mass layer	$j\omega\rho_s$
semi-infinite Newtonian liquid	$(\omega\rho_L\eta_L/2)^{1/2}(1+j)$
Rigid mass + semi-infinite Newtonian liquid	$j\omega\rho_s+(\omega\rho_L\eta_L/2)^{1/2}(1+j)$
semi-infinite viscoelastic layer	$(G\rho_f)^{1/2}$
Finite viscoelastic layer	$(G\rho_l)^{1/2}\tanh(\gamma h_f)$

In recent years, TSM resonator has became a versatile tool in bioanalysis. Monitoring the adsorption of proteins is the primary application area for TSM resonators. The proteins could be physically adsorbed onto the surface to form a monolayer, or protein multilayer deposited by the Langmuir-Blodgett techniques or self-organization processes [13-15]. Immunosensors are another important application for TSM resonators [16-19]. More recently, TSM resonators combined with cells have been used to monitor cell behaviors. Several types of cells were investigated in these studies, including endothelial cell, osteoblasts, MDCKI and II cells, 3T3 cells, VERO cells and CHO cells [20-23]. In most of studies, the dynamic processes of cell attachment and spreading on the resonator surface have been monitored. The results have demonstrated that resonant frequency shifts and motional resistance changes are related to the processes of cell attachment and spreading. However, the frequency shift due to cell monolayer attachment is significantly smaller than expected by the Sauerbrey equation for cell mass. Therefore, Redepenning et al. pointed out that cell layer attaching to the resonator cannot be

treated as a rigid mass [24]. Later, studies by Jansoff et al. and Fredriksson et al. showed that the present of a confluent cell layer attaching to the resonator increased both energy dissipation and energy storage on the resonator surface, which indicates that the cell has to be treated as a viscoelastic material [20, 25]. Recent studies by Wegener et al. demonstrated that the signals of TSM resonators are contributed to many factors, such as cell-substrate interactions, viscoelastic properties of cells, and the properties of the interfacial layer between cells and substrate [23]. Although previous studies have shown acoustic wave sensors can detect various changes in the acoustic wave propagation pathway, current research on acoustic wave devices as cell-based sensors is only focused on monitoring cell attachment and spreading. There is no theoretical model to describe the relationship between electrical measurements and cell behaviors as well as properties. No studies have been performed to characterize cell viscoelasticity by using TSM resonator sensors. Therefore, in this study, we developed a theoretical model to predict how electrical measurements of TSM resonators change with the cell layer and interfacial layer between the cell layer and sensor surface and studied the changes in cell-substrate distance and cell viscoelasticity during cell attachment and spreading, and formation of focal adhesion, as well as under cytoskeleton disruption. Using our theoretical model, we also characterized the viscoelasticity of cell monolayer by TSM resonators.

1.2.4 Love-mode Acoustic Wave Sensors

Since liquids do not support shear waves, modes can be used for liquid sensing if they exhibit shear-horizontal polarization. In isotropic materials, there is no true shear-polarized surface wave. However, for a strongly anisotropic piezoelectric crystal and layered structures, surface-localized shear modes can be obtained. In some anisotropic materials, a surface

skimming bulk wave (SSBW) occurs (**Figure 10A**) [10]. To satisfy the stress-free boundary condition, the SSBW is propagating into the bulk materials. Another mode supporting shear-horizontal waves is leaky SAW(**Figure 10B**) [10]. The wavevector and the direction of energy flow are not parallel to each other. Lithium tantalite ($LiTaO_3$) with the Y-rotated cut along the X-axis support the leaky SAWs.

For the surface skimming bulk wave and leaky SAWs, the acoustic waves are propagating deeper (1-5 wavelength) into the bulk material, which reduces the sensitivity to the surface perturbation. One approach to increase the sensitivity is to apply a dielectric layer onto the top of the propagating surface to trap the acoustic energy near the surface (**Figure 11**). This mode is called wave-guided SH-SAW or Love mode. Any materials that support shear wave shear waves such as SSBW, SH-SAW and leaky waves can be used as a substrate of Love mode devices. For example, as a standard material, Y-rotated quartz (ST-quartz) which supports SSBW has often been used. Furthermore, 36^o YX-$LiTaO_3$ that supports leaky SAWs is advantageous because of its very high electromechaical coupling coefficient and moderate temperature dependence. Amorphous silicon dioxide (SiO_2) and also polymers have been reported as overlay materials.

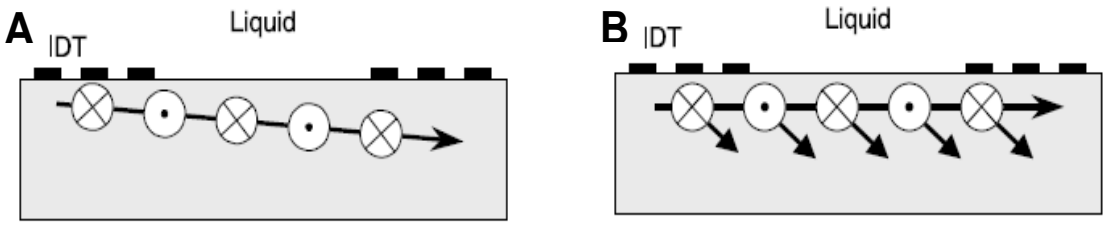

Figure 10. Two surface-localized shear modes in anisotropic materials (SSBW (A) and Leaky SAW (B)) [10]

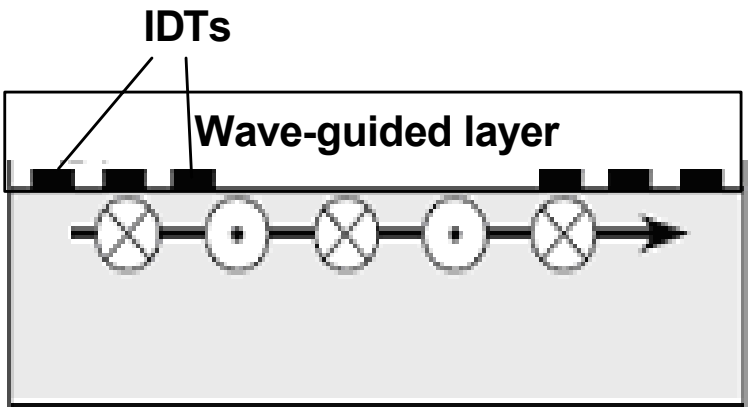

Figure 11. Love wave sensor. [10]

Although Love mode acoustic wave devices have a lot of advantages in terms of using in the liquid phase, current research on Love mode acoustic wave devices as biosensors is very limited due to complexity of theoretical modeling and experimental measurements. Theoretical modeling of Love mode devices is important to optimize the sensor performance and predict the electrical signals changes due to the perturbation on the sensor surface. The general method is based on seeking the solution of the wave equations that satisfies the boundary conditions between each layer. This method can accurately describe the acoustic waves. However, it is computationally intensive and difficult to relate physical changes to corresponding numerical changes in the model, especially in the case of considering the loss of materials. Therefore, this analytic method is usually used to predict the electrical signals changes induced by the mass changes in the loading layer. Perturbation theory has also been used in the theoretical modeling of Love mode devices to evaluate the effects of small system variations. Basically, the wave equation without perturbation is solved first and then the solutions are adapted to perturbation equations to solve the effect of small changes in the sensor system [3, 28, 29]. The assumption in perturbation theory is that the changes in the system parameters are very small. The perturbed

termed are often replaced by the exact, unperturbed solution and only the quantities of interest are unknown in the equations. Therefore, the perturbation method is limited on the modeling of the small changes of physical parameters in a system. Transmission line model is one method that has been widely used for the modeling of acoustic wave devices. An analogy between mechanical structures and transmission lines is used to describe the properties of propagation and attenuation along the acoustic devices in this method [30]. Recently, the transmission line model has been applied for the modeling of Love mode acoustic wave devices as sensors [31]. It has been demonstrated that this model provides an efficient way to describe the behavior of the sensor loaded by viscoelastic masses in a viscous liquid. However, this method is complex for modeling the complex loading on the device surface, such as the multilayer loadings in cell-based biosensors. Therefore, it is necessary to develop a simple and precise method to describe how the two characteristics of the Love mode acoustic wave device (e.g. phase velocity and insertion loss) change with multilayer loadings. The loading layers could be pure elastic, viscoelastic or viscous layers. In this dissertation, transfer matrix method will be used in modeling of Love mode devices as cell-based biosensors.

1.3 MICROFABRICATION AND SOFT LITHGRPAHY

Micro-fabrication or micromachining are the techniques for fabricating of miniature structures, at micron or smaller scales. It was originally used for semiconductor devices in integrated circuit fabrication. Now they are extended to be used for the fabrication of sensors, microreactors, microelectromehcanical systems (MEMS), microanalytical systems and micro-optical systems. The basic techniques include deposition of thin film, patterning, etching and so on. The thin film

deposition processes include the simple spin-on method, where a material in liquid form is deposited on the wafer and the wafer is spun at high speeds to evenly spread a thin film of material across the substrate, and more complex physical and chemical methods that utilize complex chemical reactions and physical phenomena to deposit films. Patterning techniques are used to create features on the micrometer or nanometer scales in the thin film layers. The most powerful of patterning techniques is the photolithographic (also optical lithography) process. It uses light to transfer a geometric pattern through a photomask to a light-sensitive chemical (photoresist) on the substrate. Usually, photolithography involves three primary steps: deposition of a photosensitive emulsion layer, ultraviolet exposure of photoresist to some pattern and subsequent develop of the wafer to remove unwanted photoresist and etching of materials in desired areas by physical or chemical means. The patterned photoresist serves as a material template for the definition of microstructures. Patterns can be etched directly into the silicon substrate, or into a thin film which in turn can be used as a mask for subsequent etches. Many etching forms including wet-chemical, dry-chemical, and physical etching techniques are used in MEMS processing.

Although photolithography is a dominant technology, it has some limitations in several applications. For example, it is poorly suited for patterning non-planar surfaces; it is relatively limited for the fabrication based on the materials other than photoresists; if working with other materials, it is necessary to attach photosensitizer, which is not convenient [32]. In 1990's, another type of patterning technique called "soft lithography" was developed by the George Whitesides Research Group at Harvard University [33]. Soft lithography uses soft, transparent and elastomeric polydimethylsiloxane (PDMS) "stamps" with patterned relief on the surface to generate features. The dimension of features generated by soft lithography is as small as 30nm.

Usually, the stamps can be prepared by molding prepolymers against masters by conventional lithographic techniques. Up to now, a lot of techniques have been developed, including micro-contact printing (μCP), replica molding [34], micro-transfer molding (uTM), micro-molding in capillaries(MIMIC), solvent-assisted micro-molding (SAMIM), and so on. In the following, I will briefly review several soft lithography techniques and their applications [32, 33].

Micro-contact printing technique uses the relief pattern on the surface of a PDMS stamp to form patterns of self-assembled monolayer (SAMs) on the surfaces of substrate by contact. For example, hexadecanethiol self-assembled monolayer (SAMs) can be patterned on the surface of gold by micro-contact printing method **(Figure 12)**. The patterned self-assembled monolayer can act not only as a resist against etching, but also as a template in selective deposition. Therefore, the materials that can be patterned using microcontact printing method are not limited to SAMs. A variety of materials can be patterned, including liquid prepolymers, conducting polymers, inorganic salts, metals, ceramics and proteins, by patterning SAMs at the molecular scale followed with the deposition of other materials on the patterned SAMs.

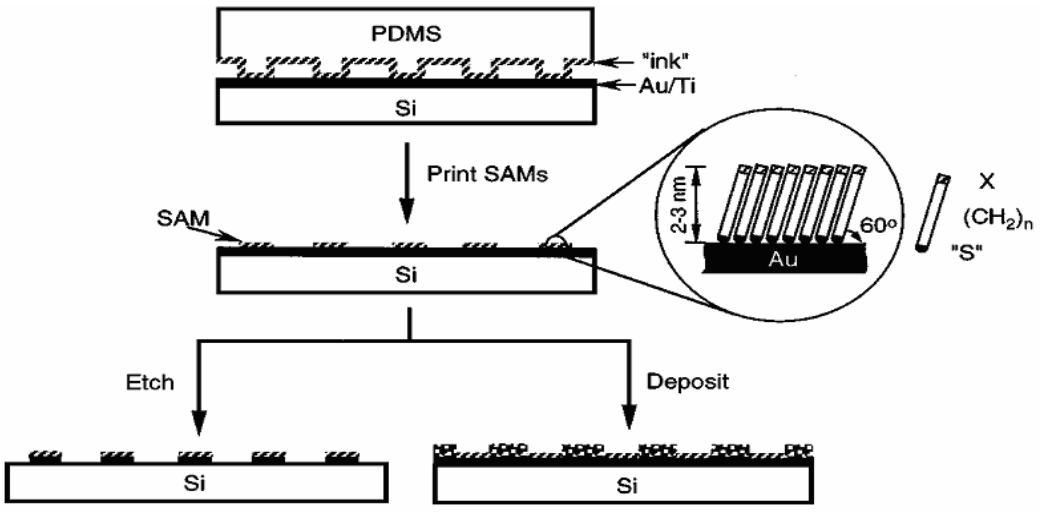

Figure 12 Schematic procedures for microcontact printing of hexadecanethiol on the surface of gold [32]

Other types of soft lithography methods that are widely used are micro-molding related techniques, including replica molding (REM) [34], microtransfer molding (μTM), micro-molding in capillaries (MIMIC) and solvent-assisted micro-molding (SAMIM) **(Figure 13)**. In replica molding, PDMS stamp is molded against a photolithographic patterned master. Polyurethane is then molded against the secondary PDMS master. In this way, multiple copies can be made without damaging the original master. The technique can replicate features as small as 30 nm [32]. In microtransfer molding (μTM), a PDMS stamp is filled with a prepolymer or ceramic precursor and placed on a substrate. The material is cured and the stamp is removed. The technique generates features as small as 250 nm and is able to generate multilayer systems [35]. In micro-molding in capillaries (MIMIC), continuous channels are formed when a PDMS stamp is brought into conformal contact with a solid substrate. Capillary action fills the channels with a polymer precursor. The polymer is cured and the stamp is removed. MIMIC is able to generate features down to 1 μm in size [36]. In Solvent-assisted Microcontact Molding (SAMIM), a small amount of solvent is spread on a patterned PDMS stamp and the stamp is placed on a polymer, such as photoresist. The solvent swells the polymer and causes it to expand to fill the surface relief of the stamp.

Soft lithography techniques have a lot of advantages over conventional patterning methods. First, this technique is low cost, easy to learn and accessible to a wide range of users. It has capacity of generating features on non-planar substrates. It can be used to pattern a wide variety of materials, such as metals and polymers [37, 38]. In addition, it can produce the patterns and structures with lateral dimensions from 30nm to 500μm, which extends the existing nanolithographic techniques. However, there are several unresolved problems such as distortions in the mask which induces the defects in patterns. Soft lithographic techniques have wide

potentials in fabrication of a variety of functional components and devices in the areas of optics, microanalysis, display, MEMS, microelectronics, and cell biology. Especially, in cell biological studies, soft lithography is well suited for generating micro-fluidic channels in PDMS, which is useful for the study of cells. The patterning of bacteria and cells on the surface by soft lithography provides new opportunities for sensing and detecting bimolecular as well as whole cells and studying cell-cell interaction and interactions between cells and their surroundings. For example, soft lithography can be used to immobilize the single-strained DNA on sensor surface (such as microcantilever) to detect the DNA hybridization. Using soft lithography, many studies have been performed to investigate the effects of cell spreading area and cell shape on cell function. Previous studies showed that the degree of cell spreading influences DNA synthesis [39], proliferation and apoptosis [40, 41], and focal adhesion assembly [42] in human and bovine capillary endothelial cells; differentiation in mesenchymal stem cells [43]; and gene expression and protein synthesis in primary rat bone cells [44].For a fixed spreading area, studies on cell shape regulation are mainly limited to cell motility, i.e., lamellipodia extension and direction of cell migration. For example, cells preferentially extended lamellipodia from their corners regardless of their geometric shapes [45, 46]. During migration, narrow teardrop-shaped or triangular cells moved predominantly toward the blunt end, while wide cells did not; rectangular cells migrated outward towards their two ends without bias for either one, but circular or square cells moved in random directions [33]. In this dissertation, using the soft lithography techniques, we studied the effects of the aspect ratio of cell shape on collagen type I synthesis in human tendon fibroblasts, examined the distribution of actin cytoskeleton, focal adhesions, and cell traction forces in human tendon fibroblasts of various shapes and correlated them to the expression of collagen type I in these tendon cells.

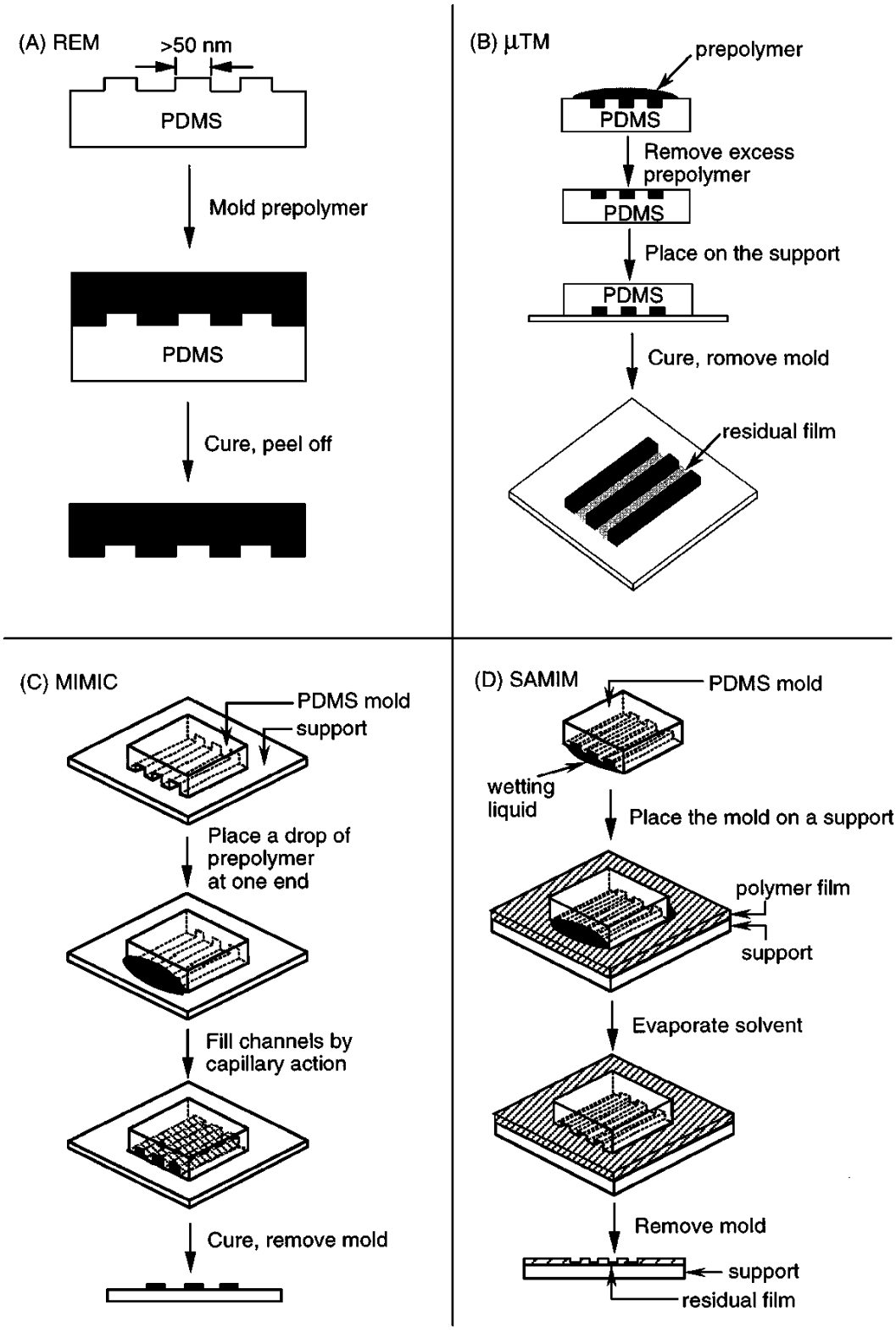

Figure 13 Schematic illustration of procedures for (a) replica molding [34], (b) microtransfer molding (μTM), (c) micromolding in capillaries (MIMIC), and (d) solvent-assisted micromolding (SAMIM)[32].

1.4 CELL BIOLOGICAL BACKGROUND

In this dissertation, we applied acoustic wave sensing and soft lithography technologies for cell biological studies. In this section, some background information on cell biology based on the scope of this dissertation will be introduced. The section will begin with a discussion of cellular architecture, especially for cell membrane and cytoskeleton that are associated with cell adhesions and viscoelastic properties. Extracelluar matrix (ECM), cell-ECM adhesion, cell traction force and cell viscoelastic properties will be explained then.

1.4.1 Cellular Structure

Plasma Membrane

The plasma membrane **(Figure 14)** consists of phospholipids and proteins. The phospholipids with a phosphate group attached to one end are arranged in two layers. The lipid part of the molecule is hydrophobic while the end with phosphate group is hydrophilic. In each layer, the hydrophobic part of the molecule faces toward the other layer, and the hydrophilic end of each molecule faces away from the membrane. The lipid bilayer is a basic structure of the membrane and prevents most water-soluble material from entering cells. This phospholipids bilayer is generally about 7.5 nm thick. Proteins in the membrane have hydrophobic and hydrophilic regions and orient themselves in the lipid layer accordingly. Hydrophobic parts of the protein associate with the interior of the membrane, while hydrophilic parts protrude to the outside of the membrane. These membrane proteins can be classified into two different types: the integral proteins that pass through the cell membrane and the peripheral proteins which stud the inside and outside of the membrane. On average, proteins constitute approximately 50% of the

mass of the cellular membrane and serve approximately seven different cellular functions: some proteins provide structural integrity to the cell membrane; some proteins serve as pumps to transport ions across the cell membrane; some proteins as carriers transport substances within the cell; integral proteins that form ion channels; receptor proteins that bind neurotransmitters and hormones; enzyme proteins that catalyze reactions at the membrane surface; and glycoproteins that are responsible for antibody processing and cellular adhesion to surfaces.

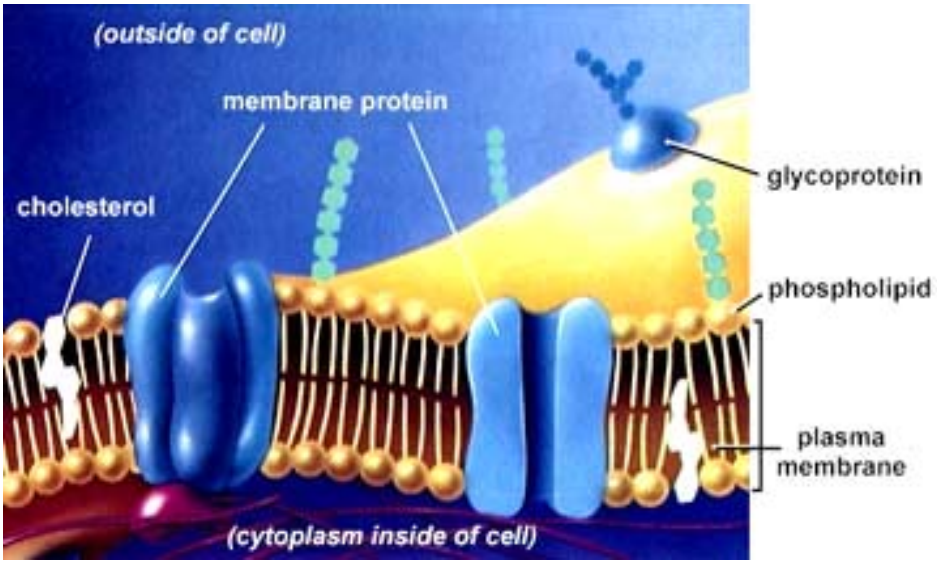

Figure 14 Cell plasma membrane consisting of phospholipids and proteins [47].

Cytoskeleton

Cytoskeleton is an internal three-dimensional network throughout the intracellular space. It helps establish and maintain cell shape, cell movement and cell division. In addition, the cytoskeleton allows positioning and moving organelles within the cytoplasm. It has been estimated that up to 80% of the proteins of the cytoplasm and 20-40% of the water in the cytoplasm are associated with the cytoskeleton [48]. Based on their diameter and their chemical

properties, the structural elements in the cytoskeleton are classified into three types: actin filaments, microtubules, and intermediate filaments **(Figure 15)**.

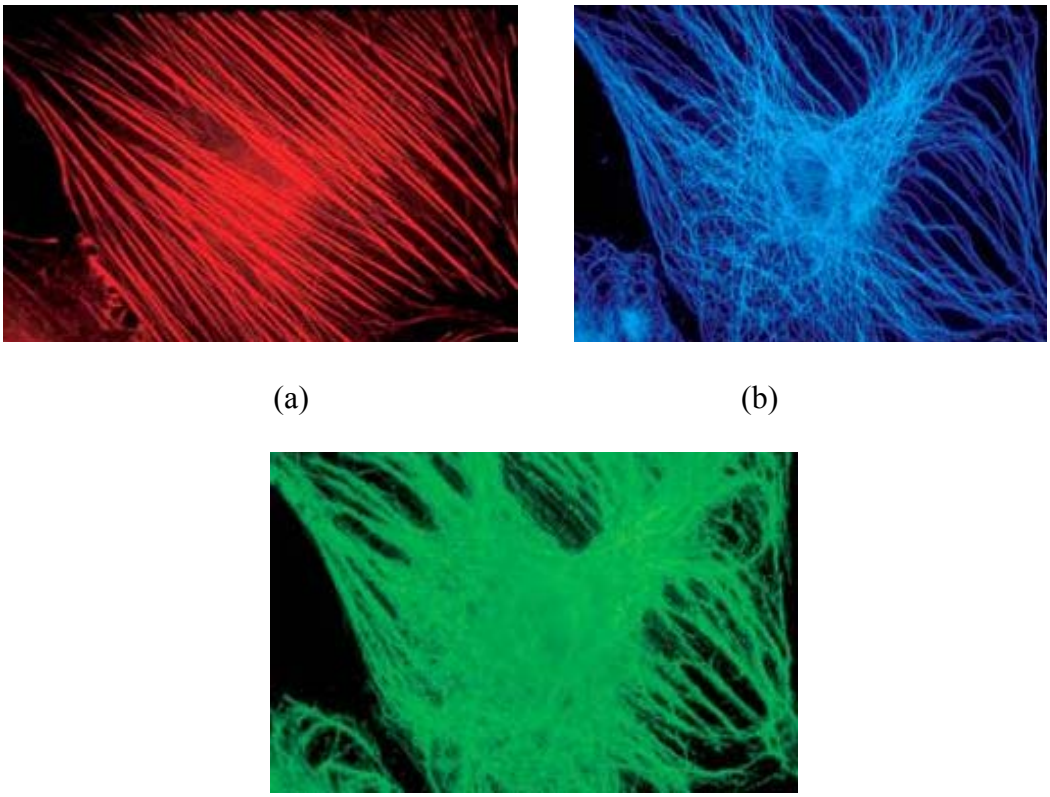

(a) (b)

(c)

Figure 15. Three types of cytoskeleton: (a) actin filaments, (b) microtubule and (c) intermediate filaments

Actin filaments are the smallest major cytoskeleton components, whose diameter is about 7nm. Actin filaments are polymers of protein actin. Normally, individual actin filaments organize themselves into actin bundles and networks. The bundles consist of closely packed arrays of parallel actin filaments and generally protrude from the cell surface, while the networks consist of loosely packed, crisscrossed actin filaments and are present in the interior cells. The actin bundle projections create fingers of membrane: microvilli and filopodia. The microvilli are responsible for transportation of nutrients from the surrounding media into the cell or tissue,

while filopodia are responsible for cell attachment.Both actin bundles and networks are connected to the plasma membrane via membrane-actin filament binding proteins [47]. Microtubules are the largest structures in the cytoskeleton and their diameter is approximately 25 nm. In contrast to actin filaments, these long microtubules never form two- or three-dimensional networks and have an inherent polarity. Their negatively charged ends make the microtubules radiate out from the nucleus of the cell while the positively charged ends elongate and make contact with the actin network associated with the plasma membrane. This allows the communication, transport and control from the center of the cell to the periphery. Microtubules are responsible for chromosomes movement, polarity and overall shape of cells, the spatial disposition of organelles, distribution of actin filaments and intermediate filaments etc. Intermediate filaments are 10 nm in diameters, smaller than the 25 nm microtubules but larger than the 8 nm microfilaments. The intermediate filaments are the most stable elements in cytoskeleton and are though as a scaffold to support the entire cytoskeleton framework. In addition, they are prominent in cells that withstand mechanical stress and are the most insoluble part of the cell [48].

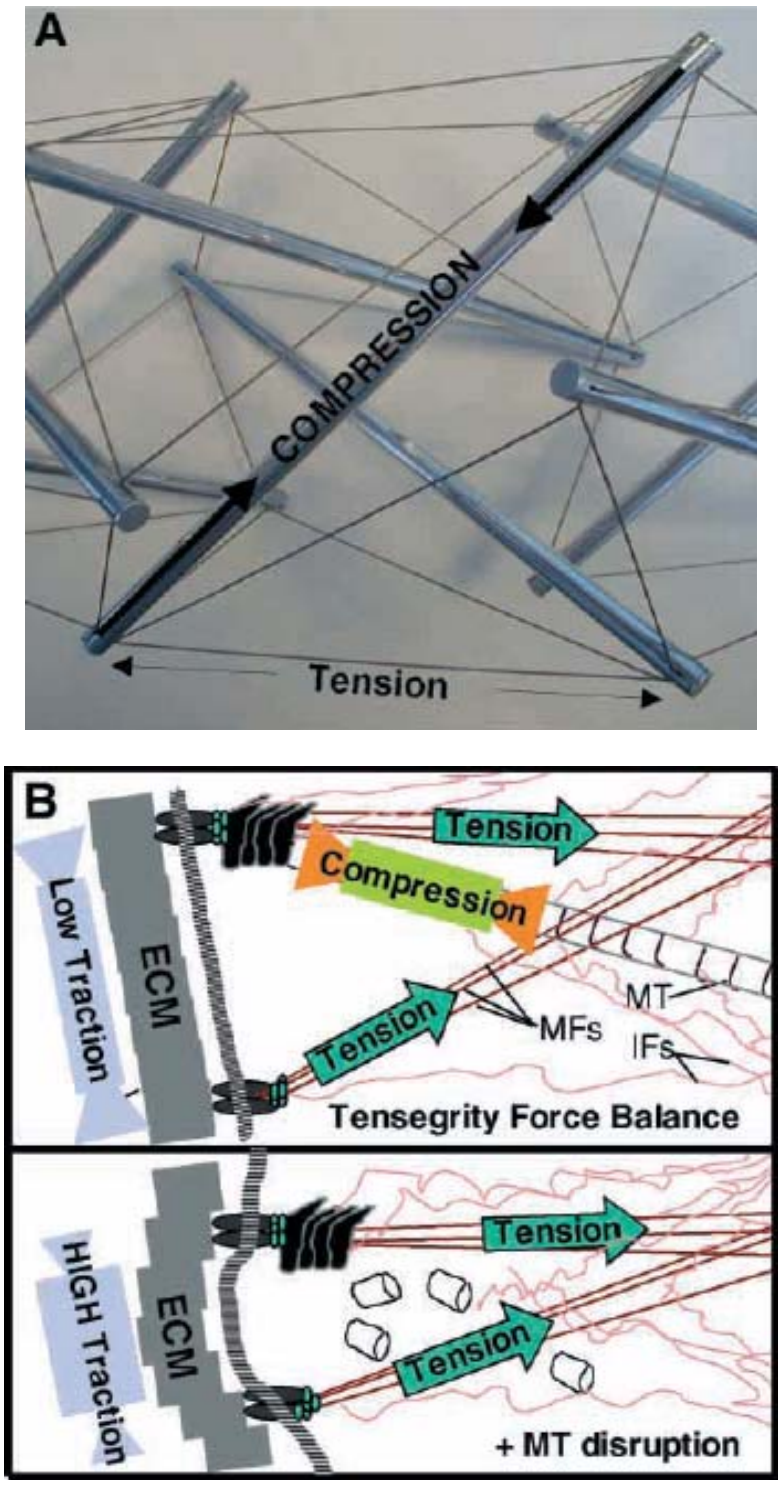

Figure 16. (A) Tensegrity model. (B) Force balance between tensed microfilaments (MFs), intermediate filaments (IFs), compressed microtubules (MTs) and the ECM in a region of a cellular tensegrity array. [49].

Previous studies show that cytoskeleton is not a passive gel. Cells generate tensile forces through actomypsin filament in their cytoskeleton. People used “tensegrity” model to predict the complex mechanical behaviors of mammalian cells **(Figure 16)** [49]. In the cellular tensegrity mode, the whole cell is described to be a prestressed tensegrity structure. Tensional forces are borned by actin microfilaments and intermediate filaments, and theses forces are resisted by the compression by internal microtubule and extracellular matrix (ECM).. Therefore, when cells are subjected to the mechanical forces or changes in mechanical properties of ECM (e.g. stiffness of ECM), the force balance between cells and ECM are altered. Cells sense the external mechanical signals at the adhesions between cells and ECM and change their cytoskeleton network structure and tensile forces in order to obtain new force balance with underlined ECM. For example, when large deforming forces are applied to the integrins, cytoskeletal filaments and linked intranuclear structure can be found to realign along the applied tension force direction [50, 51]. Changes in cytoskeleton structure and mechanics cause the global distortion of the whole cell shape. In the above example, cells will change to the elongated shape along the applied field line. As talked earlier, up to 80% of the proteins of the cytoplasm and 20-40% of the water in the cytoplasm are associated with the cytoskeleton, including a lot of enzymes and substrate that mediate cellular metabolism (e.g., protein synthesis, glycolysis, RNA processing, DNA replication) [52]. The changes in cytoskeleton structure and mechanics induce the stress and shape change in the molecules that are immobilized to the cytoskeletal scaffold. These shape changes of molecules alter the biophysical properties (thermodynamics, kinetics), and hence biochemistry (e.g. chemical reaction rates) will be altered [53]. Finally, these biochemistry changes will produce various effects on cell behaviors (e.g. proliferation, apoptosis, ECM production). So, because of this integrated structure, cytoskeleton governs how cells process and integrate locally-induced

signals. Through the tension-dependent changes in cytoskeleton structure and mechanics, cells respond globally [54]. Because of the specific structure and properties, cytoskeleton plays a critical role in regulating cell-ECM adhesion, determining cell mechanical properties and cell mechanotransduction.

1.4.2 Extracellular matrix (ECM)

In vivo, the cellular membrane is surrounded by the extracellular matrix (ECM), a collection of fibrous collagen proteins, proteoglycans (complexes of polysaccharides and proteins), and glycoproteins (proteins linked to chains of carbohydrates), and adhesive glycoproteins (fibronectin, laminin, vitronectin and tenascin). It can be found in the extracelluar environment of all tissues and organs. Its compositions are changed with different cell type, tissue type and culture conditions [55].

The ECM serves various functions [55, 56]. First, it provides cells the physical microenvironment. It allows cell attachment and serves as a scaffold, guides cell migration during embryonic development and wound repair. Second, the ECM contains many signaling molecules that regulate various cellular functions, such as proliferation, differentiation and death. In addition, previous studies have revealed that the molecular compositions of the ECM, the geometric presentation of adhesive proteins in ECM, as well as its topography and mechanical properties are important in cellular function [57]. Recent studies have demonstrated that the cytoskeleton organization and focal adhesions on soft substrates are different from those on hard substrates, which suggests that the cell probes the stiffness of the ECM and alters its structure and function accordingly [56, 58]. On the other hand, these features of the ECM are determined both by the cells that produce it and by the cells that grow on or inside the matrix.

1.4.3 Cell-ECM adhesion

In order to survive and grow, cells must attach to and spread on a substrate. When a cell contact with a solid surface, adhesions are formed with ECM at specific sites. These adhesions are mediated by integrins, which are transmembrane proteins with extracellular domains that bind with low affinity to fibronectin (or vitronectin, or some other component of the ECM) and intracellular domains that link to the cytoskeleton **(Figure 17)** [58, 59]. Before the activation, integrins are freely diffusive within the cell membrane. However, after they bind to the ECM, the integrins undergo a conformational change and cytoplasmic proteins (talin, vinculin, α-actin) are recruited to the adhesion site. Those cytoplasmic proteins connect the integrins to the cytoskeleton, or biochemically initiate or regulate intracellular signaling pathways. With physical clustering of multiple integrins and recruitment of more cytoplasmic proteins, the size, adhesion strength, and biochemical signaling activity of adhesions increase. These larger, clustered structures of integrins and cytoplasmic proteins are commonly called focal adhesions **(Figure 18)**. Focal adhesions are flat, elongated structures with several square microns in area and separated from the substrate by 1 to 15 nm. Normally, these focal adhesions are located near the periphery of cells. Development of focal adhesions is stimulated by the small GTPase Rho-A, and is driven by actomyosin contractility [58].

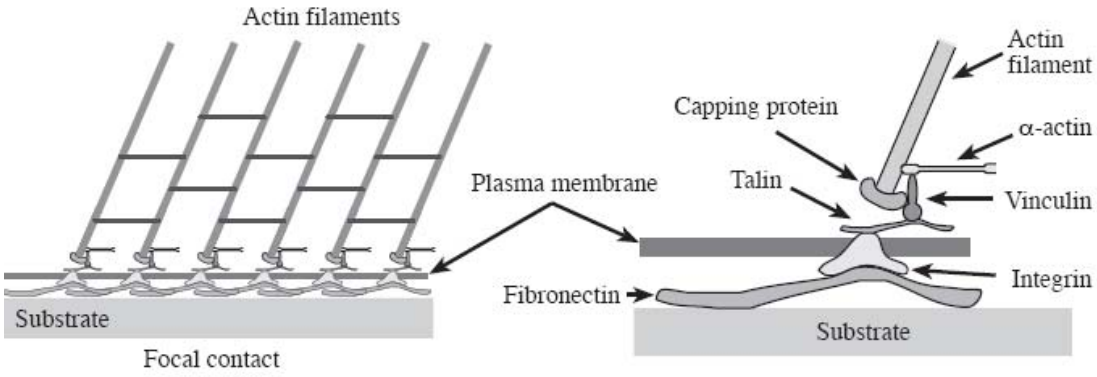

Figure 17. Focal contact or adhesion [47]

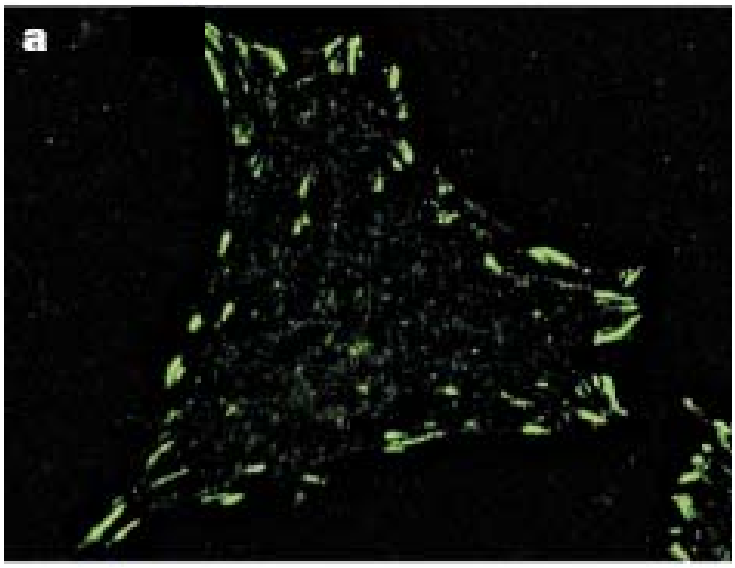

Figure 18. Immunofluorescence image of the focal adhesions [56].

Via the focal adhesions, cell-ECM adhesion provides a common pathway for the signals transmission. Through cell-ECM adhesion, ECM scaffold provides the mechanical support to balance the tension in adhering cells. So, mechanical properties, topology of ECM, and availability of adhesive proteins in ECM are critical determinations of cytoskeletal organization and cell morphology, which govern a lot of cell behaviors. Conversely, changes in cytoskeleton structure and mechanics alter the states of cell adhesion to ECM.

When cells contact to a solid surface, cells experience three stages: attachment, spreading and formation of focal adhesions and stress fibers **(Figure 19)**. The adhesive strength increases with each stage. The stage of attachment involves integrin–ECM binding. During this state, the binding between cells and ECM is very weak. With the binding of ECM components to integrins, integrin clustering is induced and the affinity for the ligand increases. After that, the contact area with substrates increases and actin microfilaments are developed. This state is considered as the intermediate state between weak adhesion and strong adhesion. During the third stage, cells organize their cytoskeleton and form actin-containing stress fibers. At the same time, the integrins cluster together and cytoplasmic proteins are recruited to the adhesion site to connect integrins to cytoskeleton to form focal adhesion. Focal adhesions enhance adhesion, functioning as structural links between the cytoskeleton and the extracellular matrix and triggering signaling pathways that direct cell function. After the formation of focal adhesion and stress fibers, a strong and steady adhesion between cells and ECM substrate is obtained [60]. Cells modulate the states of cell adhesion in many pathological and physiological processes, such as tissue remodeling during morphogenesis and wound healing, cellular metaplasia, cell proliferation, tumor cell matastasis, cytokinesis and cell apoptosis during tissue remodeling [60]. For example, the weak adhesive state is consistent with cells undergoing apoptosis during tissue remolding, or those undergoing cytokinesis. The intermediate state is characteristics of cells involved in the response to injury during wound healing or in tissue remodeling during morphogenesis. The strong adhesion shows cells are differentiated and quiescent.

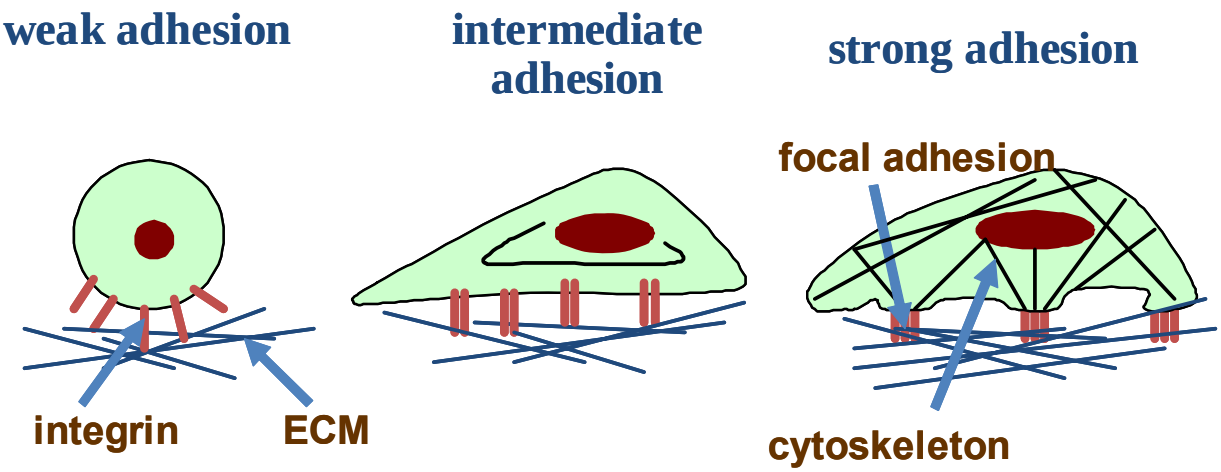

Figure 19. Three states of cell-ECM adhesion [60].

The existing methods for studying cell adhesion are very often based on the observation of cell morphology using time lapse videomicroscopy [25]. The limitations of this method are time consuming, labor intensive and qualitative in measurements. To overcome these limitations, methods for quantitatively monitoring cell adhesion in real time are highly desirable. Recently, a technique called electric cell–substrate impedance sensing (ECIS) was developed **(Figure 20)** [61, 62]. This technique is based on the electric impedance measurement between one large electrode and one small electrode. Cells are cultured on the small electrode and the large electrode is served as a reference. The cells block the current flow path and change the impedance, which is dependent on the cell-covered area, cell-substrate distance and electrical impedance of cell layers. So this method provides quantitative information on cell morphology and cell-substrate separation in real time. It can be used to measure cell attachment, motility, and membrane capacitance. The impedance measurement provide the electrical properties of cells, however, it cannot be used to measure cell mechanical properties.

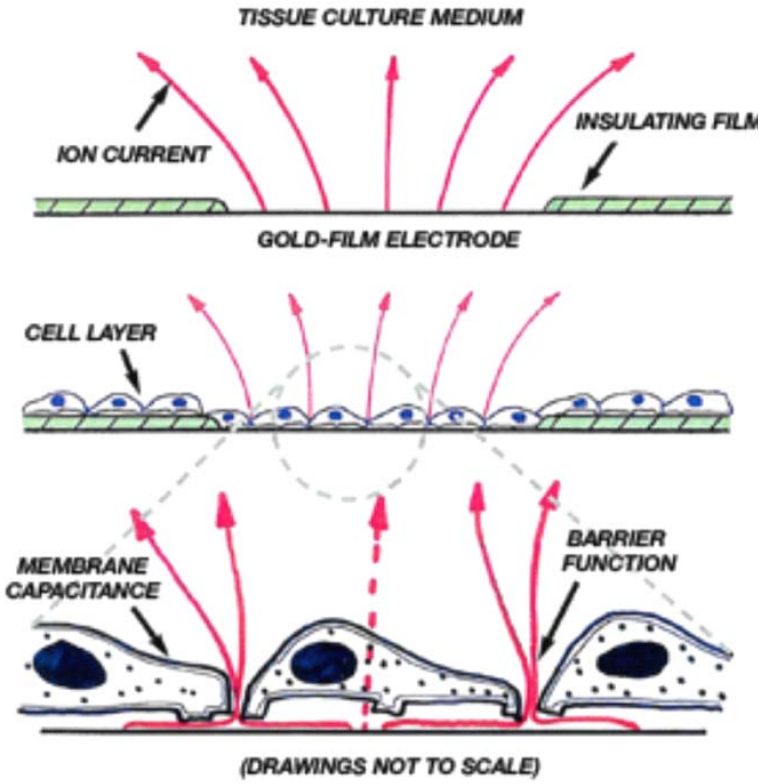

Figure 20. Principle of electric cell-substrate impedance sensing (ECIS) for monitoring cell adhesion [63]

1.4.4 Cell viscoelasticity

Cells have been shown to exhibit a viscoelastic behavior in previous studies [64, 65]. When deformed, the cell stores mechanical energy, which permits subsequent recovery of its shape. It also dissipates mechanical energy through mechanical friction. The responses of the cell to mechanical forces depend on the rate of mechanical loadings. The structural origin of cell elasticity is widely believed to originate in the network of actin fibers within the cytoskeleton. However, the origin of energy dissipation is less clear but is often thought to arise from viscous mechanisms associated with the cytoplasmic fluids and membranes. As discussed earlier, cytoskeleton plays a critical role in regulating the mechanical stresses and resulting deformations,

which has been recognized to regulate various cell function, such as proliferation, differentiation, wound healing, protein and DNA synthesis, apoptosis, and cell motility [66]. The measurements of viscoelastic parameters of cells are expected to give insight into the structure of the cortical and internal cytoskeleton and are important to understanding cell function in many physiological and pathological processes. It has been observed that cell motility is related to viscoelastic change of the lamellipodium, which is explained as the polymerization of actin filaments [67]. Stretch can modify cell viscoelastic properties because it alters the balance of forces at the cell-cell and cell-matrix adhesions and induces a change in cytoskeletal prestress [68]. In addition, the changes in viscoelastic properties of living cells can be induced by the onset and progression of diseases or surrounding biological environments. For hepatocellular carcinoma cells (HCC), its viscoelastic properties probably have significance on tumor cell invasion and metastasis, in which it determines the flow behavior of tumor cells in the circulation and thus whether such cells can be arrested to form metastases [69]. Therefore, measurements of viscoelastic properties of cells help understand the developmental processes underlying disease progression and also facilitate the use of living cells as sensory elements in the biosensor systems for numerous emerging applications such as drug screening and environment monitoring, etc. Current common techniques for measuring cell viscoelasticity include micropipette aspiration, optical tweezer, microplate, atomic force microscopy (AFM), magnetic bead rheometry and micro/nanoparticle **(Figure 21)** [70]. Here I will briefly review these techniques.

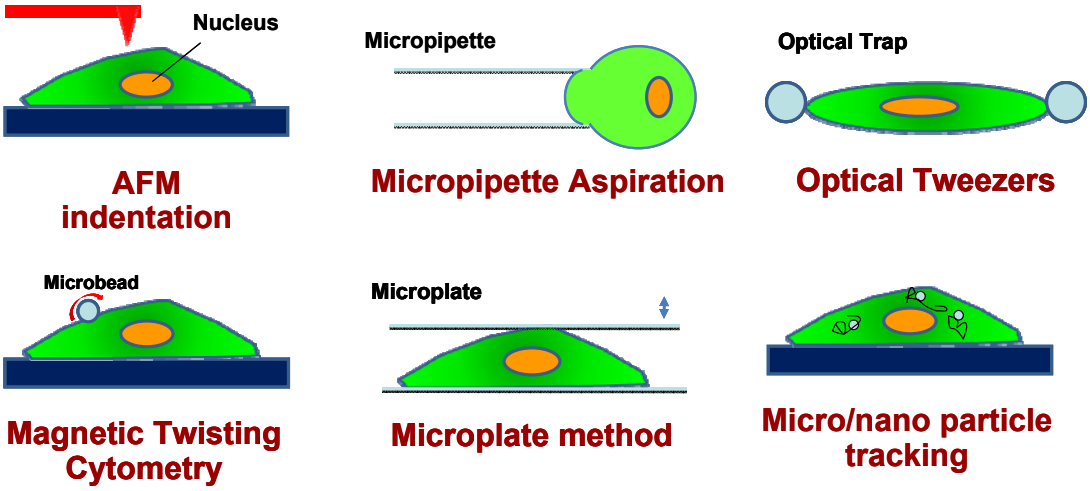

Figure 21. Schematic depiction of common experimental techniques for measuring cell visoelasticity [70]

Micropipette aspiration is one of the most widely used techniques for characterization of cell viscoelasticity. During the measurements, the cell is aspirated into a glass pipette with an inner diameter smaller than the cell. The cell deformation is measured by optical microscopy [71]. Fine force resolutions are controlled by the applied pressure and the inner diameter of the pipette. The force applied on the cell and cell deformations are used to exact cell viscoelasticity. However, this technique requires the cell to undergo large deformations, which makes it incompatible with some cell types.

Optical or laser tweezers techniques are used to manipulate functional beads attached on cells. The laser refracts when it passes through a bead. According to the conservation of momentum, the changes in photon momentum cause the changes in the bead's momentum[72]. As such, the force is applied on the beads through the focal points of the laser. This force is proportional to the perpendicular distance from the optical axis of the trap. The displacement of the beads can be measured by tracking the refracted beam with photodiodes. This method is used to measure the global viscoelastic properties of the single cell.

Microplate method is another widely used method for characterization of cell viscoelasticity. Two microplates, one rigid, the other flexible are used in this method. The cell is adhered on these two microplates. In the measurements, the rigid microplate is moved by micromanipulator to deform the cells [73]. Compression, traction or oscillatory deformations can be obtained by controlling the movement of the rigid microplate. The cell deformation can be monitored by microscopy. The flexible microplate serves as a force sensor. Since the stiffness of the flexible microplate is known by calibration prior to the measurements, the force applied on the cell can be obtained by measuring the deformation of the flexible microplate under microscopy.

As discussed, micropipette aspiration, optical tweezers and microplate method are invasive methods for characterization of global cell viscoelasticity. In these methods, usually, the creep response and stress relaxation are measured. The simple viscoelastic models with finite springs and dashpots are used to explain the experimental results. However, the spring-dashpot model is over-simplified, which cannot precisely describe the complex mechanical properties of cells and makes the results non-reliable. More recently, dynamical viscoelastic properties of cells were characterized. In these studies, the complex shear modulus ($G^*(\omega)$) from oscillatory measurements over a wide frequency range were measured. $G^*(\omega)$ is defined as the complex ratio in the frequency domain between the applied stress and the resulting strain. The real and imaginary parts of $G^*(\omega)$ account for the elastic energy stored and the frictional energy dissipated within the cell at different oscillatory frequencies.

AFM is one of methods to probe the dynamical viscoelastic properties of cells [74]. In the measurements, the AFM probe is indented into and deforms the cell body. The cantilever deflection is detected by the photodiodes. However, operation in aqueous environments, which is

often required to maintain normal cell function, may be complicated due to fluid-probe interaction and reflection or refraction of the laser used for sensing [70]. Magnetic bead micro-rheometry has also been used for measuring the dynamic viscoelastic properties of cells. Magnetic beads attached to cells can be manipulated by the external-generated magnetic field, therefore apply various loadings on cells. The deformation of the cell is imaged by tracking the non-magnetic beads dispersed on the surface of the cell. However, both AFM and magnetic bead micro-rheometry are invasive methods [75]. The experimental setup is complex, and the operation is time-consuming.

All the five methods I discussed above are invasive methods. Mechanical forces are directly applied on cells, such as AFM tip, micropipette, optical tweezers, magnetic beads or microplate and then cell deformation is monitored by using optical microscopy or photodiodes. The dimensions, and the contact between probe and cell surface are significantly affect the values of shear modulus. Direct contact between probe and cell will alter the local organization of cytoskeleton, which affects cell mechanical properties. Micro/nano-particle tracking method is a non-invasive and passive technique for characterization of cell viscoelasticity. In the measurements, micro or nano-particles are dispersed on the surface of cell membrane or in the cytoplasm of a cell. The displacement of these particles is mapped by tracking the path of the particles over time through successive digital images. The Brownian motion of these particles can be used to extract the viscoelastic properties of materials around them. Therefore, through tracking the path of micro or nano-particles, the local viscoelastic properties of cells are obtained. Overall, micro/nano-particle tracking method is a non-invasive, fast and sensitive technique to quantify viscoelastic modulus of cells. However, in many cases, it is hard to find natural particles in cells in terms of the location, particle dimension and so on. Based on the current techniques

for cell viscoelasticity measurements, it is necessary to develop a simple, fast, non-invasive and quantitative method to characterize cell viscoelasticity. In this dissertation, we applied acoustic wave sensing technology, which is a non-invasive method, to characterize cell viscoelasticity.

1.4.5 Cell traction force

When cells attach to and spread on the substrate, they generate internal tensile forces through actomyosin interaction and actin polymerization and exert traction forces on the substrate or extracellular matrix (ECM) through focal adhesions [76]. This traction force is very important in cell shape maintenance and mechanical signal transmission throughout the intracellular space, therefore it is important for cells to probe and respond to various physical signals at the extracellular environment. Understanding the regulation of cell traction forces to cell biological function and the ability to measure cell traction forces are critical in many physiological and pathological events, such as inflammation, wound healing, embryogenesis and metastasis [76].

Many methods have been developed to measure cell traction forces for both populations of cells and the single cell, including cell-populated collagen gel, thin silicone membrane, micro-machined force sensor array and cell traction force microscopy. Cell-populated collagen gel method is used to measure traction forces generated by population of cells. In the measurements, cells are embedded into the collagen gel and the traction forces by cells induce the contraction in gels. Therefore decrease in the diameter of the gel disk can be used to determine cell traction forces. This is the simplest method to measure the traction forces of the population of cells. However, this approach does not measure the traction forces of individual cells. It is a qualitative tool for cell traction force assay. A thin silicone film has been applied to measure cell traction forces [77]. When cells adhere or move across the film, cell traction force generates wrinkles in

the silicone film. These wrinkles are easily detectable with a light microscope and used to determine the traction forces of individual cells. However, this method has a poor spatial resolution. Because the non-linear relationship between the forces and the wrinkle geometry is too complex for facile quantitative analysis, the wrinkling substrate assays remain a qualitative tool [77]. More recently, two quantitative methods have been developed to measure the traction forces of the individual cell with a high spatial resolution: force sensor array and cell traction force microscopy. Force sensor array uses an array of micro-machined cantilever beams or polymer micropost array [78]. The deflection of the cantilever beam determines cell traction force. The limitation of this method is that it only can quantify cell traction force in one direction. The micropost force sensor array fabricated by soft lithography overcomes this limitation [79, 80]. Each micro-post is an individual force sensing unit and measures cell traction force applied on it independently. So micropost force sensor array can detect cell traction forces in all directions. Nowadays, studies on development of micropost force sensor array is still going on, focused on the fabrication of high density micropost array and image analysis to improve the sensitivity and reliability of this method. Another quantitative method for measuring cell traction forces is cell traction force microscopy [81]. It uses elastic polymacrylamide gel (PG) substrate embedded with fluorescent beads. Cells are cultured on this substrate and deform it. The deformation in the substrate is determined by tracking the displacement of fluorescent beads embedding in elastic polymacrylamide gel (PG) substrate with and without cell adhesion to it. The deformation in the substrate is used to compute cell traction forces. The most important issues in cell traction force microscopy are how to determine the displacement field of the substrate and how to compute cell traction force through the substrate deformation. With the progresses in solving these two problems, cell traction force microscopy now provides the most

reliable and comprehensive information on cell traction forces distributed in an entire single cells [81]. Nowadays, cell traction force microscopy has been used to determine the regulation of cell traction force in cell behaviors, such as cell migration and specific gene expression [57, 82, 83]. In this dissertation, we used cell traction force microscopy to study the effects of cell shape on cell traction force.

2.0 RESEARCH OBJECTIVE

Because of potential opportunities of cell-based biosensors in fundamental cell biological research, drug development, environmental pollution, etc, cell-based biosensors have received more and more attentions. The development of innovative cell-based biosensor systems requires detailed research on transduction techniques, interface engineering and the integration of micro/nano-fabrication and biology. As discussed in chapter 1, acoustic wave sensors, especially thickness shear mode resonator and Love mode acoustic wave device, are suitable as cell-based biosensors. However, current research on acoustic wave devices as cell-based biosensors is limited, focused on the thickness shear mode resonator sensors for monitoring cell attachment and spreading. More detailed research activities, including theoretical modeling and experimental studies, are required to extend the applications of acoustic wave devices as cell-based biosensors. Furthermore, for cell-based biosensors, controlling cell function by controlling living/non-living interface in sensor systems is critical to increase the sensor sensitivity and reliability since it can reduce the variability of individual cell response and preserve the physiologic responses of the cell. Therefore, studies on engineering the interface to control cell function and determining cell response to the engineered interface are important. Currently, soft lithography has been widely used to control the adhesive protein distributions on the substrate. Using this technique, people have shown that cell spreading area regulates a lot of cell function. However, no studies have been performed to determine the effects of cell shape on cellular

structure, traction forces and protein synthesis. So, the objective of this dissertation is to develop acoustic wave sensor systems for cell biological studies and to determine the effect of cell shape on cell structure, mechanics and function by soft lithography techniques. Based on this overall objective, this dissertation has the following specific aims:

- To apply the TSM device to monitor the processes of cell attachment, spreading and formation of focal adhesion after cell addition to the medium and detachment procedure under cytoskeleton disruption **(chapter 3)**.
- To characterize the viscoelastic properties of cell monolayer by the TSM sensor **(chapter 4)**.
- To develop a theoretical model of wave-guided shear-horizontal surface acoustic wave devices as cell-based biosensor **(chapter 5)**.
- To determine the role of cell morphology in cell-ECM adhesion, cytoskeleton structure and traction forces, and cell biological function by precisely controlling cell shape using soft lithography techniques **(chapter 6)**.

In the last chapter of this dissertation, the principle conclusions and impact of this work, as well as the most promising avenues for future research will be summarized.

3.0 MONITORING CELL ATTACHMENT, SPREADING AND FORMATION OF FOCAL ADHESION BY USING THICKNESS SHEAR MODE ACOUSTIC WAVE SENSORS

3.1 INTRODUCTION

As discussed in chapter 1, quartz thickness shear mode (TSM) acoustic wave sensor is a promising method for quantitatively monitoring cell attachment and spreading in real time. In the last two decades, studies have been performed to monitor this procedure with different types of cells [20-22, 25]. Their results have successfully demonstrated that resonant frequency shifts and motional resistance changes are related to the fractional surface coverage by cells. By comparing different cell lines under otherwise identical experimental conditions, it has been found that each cell line has a characteristic frequency shift. These studies, however, only provide a qualitative observation of cell behaviors on the sensor surface, and little is known about the detailed cell behaviors and properties that are responsible to frequency shift and resistance change during cell attachment and spreading. It is highly desirable that a theoretical model can be developed to relate the behaviors and properties of attached cells to TSM sensor electric signals.

In this chapter, the theoretical modeling and experimental studies for monitoring the processes of cell attachment, spreading and formation of focal adhesion after cell addition to the medium and detachment procedure under cytoskeleton disruption will be discussed. A one-

dimensional multilayer sensor analytical model for cell monolayer adhesion on sensor surface is proposed to relate resonant frequency and motional resistance to viscoelastic properties of the cell layer and the interfacial layer between cells and the sensor surface. Besides the case of cell monolayer adhesion, we also developed a theoretical model to describe the resonant frequency shift and resistance change due to the non-uniform cell adhesion. Experimentally, the dynamic processes of cell attachment, spreading and formation of focal adhesion after cell contacting a surface have been monitored by measuring the resonant frequency shift and motional resistance change for different cell seeding densities. It has been found that during cell spreading, the resonant frequency shift and resistance change are proportional to cell seeding densities, which agrees with our non-uniform cell adhesion model. In addition, by comparing the theoretical predictions on frequency shift and resistance change with experimental results, it has been shown that during the formation of focal adhesion, the resonant frequency shift and resistance changes are responsible to the changes in the viscoelastic properties of cell layer and cell-substrate distance. Furthermore, knowing that the actin cytoskeleton is important to cell adhesion and the mechanical properties of cells, we have also investigated the motional resistance change caused by the disruption of actin cytoskeleton induced by fungal toxin cytochalasin D in the human skin fibroblasts. Our results have shown the changes in cell-substrate contact and morphology induced by fungal toxin cytochalasin D decrease the motional resistance.

3.2 THEORETICAL CONSIDERATIONS OF CELL-BASED TSM ACOUSTIC WAVE SENSOR

3.2.1 Generic modeling of quartz TSM sensor with loading

A general approach to theoretically describe the transduction mechanism of acoustic wave resonator sensors is based on solving a set of wave equations by applying boundary conditions between different layers to get the input electrical impedance of the resonator [12, 84-86]. Resonant frequency shift or mechanical loss can be correlated to the viscoelastic properties and thickness of the surface layer or the medium that the resonator contacts. However, it is quite complex to solve those wave equations, especially in the case of multilayer loadings. Here we apply transfer matrix method to obtain a generalized electrical impedance of quartz TSM resonator sensor with multilayer loading on the top electrode. If the electrode exposed to air is treated as a backing layer with acoustic impedance of $Z_1 = F_{LL}/v_{LL}$, the transfer matrix of the one-dimensional TSM resonator that relates the input electric voltage and current to the multilayer loading **(Figure 22)** on the other side of the device is given by

$$\begin{bmatrix} V \\ I \end{bmatrix} = [A] \times \begin{bmatrix} F_{LR} \\ v_{LR} \end{bmatrix} \tag{3.1}$$

where matrix A have the following format:

$$[A] = \frac{S}{\varphi H} \begin{bmatrix} 1 & j\varphi^2/\omega C_o \\ j\omega C_o & 0 \end{bmatrix} \times \begin{bmatrix} \cos\gamma_q + j\frac{Z_1}{Z_q}\sin\gamma_q & Z_q\left(\frac{Z_1}{Z_q}\cos\gamma_q + j\sin\gamma_q\right) \\ j\sin\gamma_q/Z_q & 2(\cos\gamma_q - 1) + j\frac{Z_1}{Z_q}\sin\gamma_q \end{bmatrix} \tag{3.2}$$

In this equation, $H=\cos\gamma_q - 1 + jZ_1\sin\gamma_q/Z_q$, $\varphi = hC_o$, $h = e_q/\varepsilon_q$, $C_o = \varepsilon_q S/h_q$, $\gamma_q = \omega h_q/(c_q/\rho_q)^{1/2}$, $Z_q = (\rho_q c_q)^{1/2}$, $e_q = e_{26}$, $\varepsilon_q = \varepsilon_{22}$, and $c_q = c_{66} + e_{26}^2/\varepsilon_{22} + j\omega\eta_q$. C_o is the static capacitance of piezoelectric quartz, and S is the area of quartz. c_{66}, e_{26}, ρ_q, ε_{22} and η_q are the components of the material property tensors

for mechanical stiffness, piezoelectric constant, density, permittivity and viscosity of quartz [87]. If the electrode effect is neglected, since one side of the resonator sensor is exposed to air, we have $Z_1 = 0$. According to Eq. (3.2), the input electrical impedance of the quartz resonator sensor with acoustic wave loading impedance $Z_L = F_{LR}/v_{LR}$ on the top electrode is given by:

$$Z = \frac{V}{I} = \frac{1}{j\omega C_o}\left(1 - \frac{k^2}{\gamma_q}\frac{2\tan\frac{\gamma_q}{2} - j\frac{Z_L}{Z_q}}{1 - j\frac{Z_L}{Z_q}\cot\gamma_q}\right) \tag{3.3a}$$

where $k^2=e_q^2/(\varepsilon_q c_q)$ is the electromechanical coupling coefficient of the quartz.

The abbreviations in equation (3.1) are calculated with the following equations:

$$K^2 = \frac{e_q^2}{\varepsilon_q c_q} \tag{3.2b}$$

$$\alpha = \omega h_q \sqrt{\rho_q / c_q} \tag{3.2c}$$

$$Z_q = \sqrt{\rho_q c_q} \tag{3.2d}$$

$$C_0 = \varepsilon_q \frac{A}{h_q} \tag{3.2e}$$

$$e_q \equiv e_{26} \tag{3.2f}$$

$$\varepsilon_q \equiv \varepsilon_{22} \tag{3.2g}$$

$$c_q \equiv c_{66} + \frac{e_{26}^2}{\varepsilon_{22}} + j\omega\eta_q \tag{3.2h}$$

where K^2 is the electromechanical coupling coefficient of quartz, α is the acoustic phase shift inside the quartz crystal and Z_q is the characteristic acoustic impedance of the quartz crystal. C_0 is the static capacitance of piezoelectric quartz, and A is the area of quartz. c_{66}, e_{26}, ρ_q, ε_{22}, h_q and η_q are the components of the material property tensors for mechanical stiffness, piezoelectric

constant, density, permittivity, thickness and viscosity of quartz. Z_L is acoustic loading impedance, defined as the ratio between the stress and displacement at the sensor surface.

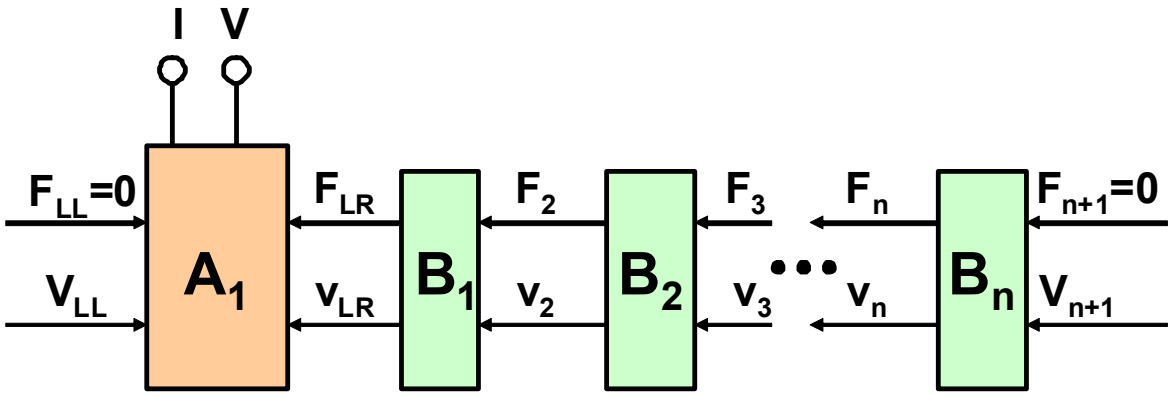

Figure 22. Transfer matrix model of a thickness shear mode (TSM) quartz resonator with multiple uniform layers loaded on one side

The electrical impedance can be separated into a parallel circuit consisting of the static capacitance C_o and motional impedance Z_m. From Eq.(3.3), the motional impedance Z_m can be written as follows:

$$Z_m = \frac{1}{j\omega C_o}\left(\frac{\frac{\gamma_q}{k^2}}{2\tan(\frac{\gamma_q}{2})} - 1\right) + \frac{1}{\omega C_o}\frac{\gamma_q}{4k^2}\frac{Z_L}{Z_q}\frac{1}{1 - j\frac{Z_L}{2Z_q\tan(\frac{\gamma_q}{2})}} \tag{3.4}$$

The motional impedance is split into two parts, Z_m^o and Z_m^L, i.e., the motional electrical impedance of unloaded quartz resonator and impedance change caused by uniform acoustic loading:

$$Z_m^o = \frac{1}{j\omega C_o}\left(\frac{\frac{\gamma_q}{k^2}}{2\tan(\frac{\gamma_q}{2})} - 1\right) \tag{3.5a}$$

$$Z_m^L = \frac{1}{\omega C_o}\frac{\gamma_q}{4k^2}\frac{Z_L}{Z_q}\frac{1}{1 - j\frac{Z_L}{2Z_q\tan(\frac{\gamma_q}{2})}} \tag{3.5b}$$

By taking the approximation of $\tan(\gamma_q/2)=4\gamma_q/[(N\pi)^2-\gamma_q^2]$ near the resonant frequency, (N is the harmonic number), the motional impedance of unloaded quartz near the series resonant frequency is expressed as

$$Z_m^o = \frac{1}{j\omega C_q} + \frac{1}{-j\omega C_o} + j\omega L_q + R_q = \frac{1}{j\omega C_q'} + j\omega L_q + R_q \tag{3.6}$$

The circuit parameters in the motional impedance have been given by Lucklum *et al* [85, 88-90] and are listed here for convenience, $C_q = \frac{8Se_q^2}{\pi^2 h_q c_{qo}}$, $C_q' = \frac{C_q}{1-8k^2/\pi^2}$, $L_q = \frac{\pi^2}{8C_o k^2 \omega_o^2} = \frac{\rho_q h_q^3}{8Se_q^2}$, $R_q = \frac{\eta_q / c_{qo}}{C_q} = \frac{\eta_q \pi^2}{8C_o k^2 c_{qo}}$, and $c_{qo} = c_{66} + \frac{e_{26}^2}{\varepsilon_{22}}$.

For small uniform loading, $Z_L/Z_q << 2\tan(\gamma_q/2)$, Eq. (3.5b) can be further simplified and Z_m^L can be expressed as,

$$Z_m^L = \frac{1}{\omega C_o}\frac{\gamma_q}{4k^2}\frac{Z_L}{Z_q} \tag{3.7}$$

According to Eqs. (3.6) and (3.7), a direct relation between impedance of the acoustic loading, Z_L, and the frequency shift at the maximum of the in-phase electrical admittance as well as the changes in the motional resistance are obtained, shown in Eqs.(3.8a) and (3.8b) (Lucklum and Hauptmann, 2003).

$$\frac{\Delta f_s}{f_o} = -\frac{\mathrm{Im}(Z_L)}{\pi Z_q} \tag{3.8a}$$

$$\frac{\Delta R_s}{2\omega_o L_q} = \frac{\mathrm{Re}(Z_L)}{\pi Z_q} \tag{3.8b}$$

3.2.2 Acoustic impedance of uniform multilayer loading and non-uniform loading

For multilayer loading with continuous boundary conditions between each layer, a transfer matrix model of quartz TSM sensor with multilayer loading can be created **(Figure 22)**. Here B_1, B_2, ... , B_n are transfer matrixes of each non-piezoelectric uniform loading layer. The transfer matrix for a non-piezoelectric layer B is given by,

$$\begin{bmatrix} F_o \\ v_o \end{bmatrix} = [B] \times \begin{bmatrix} F_i \\ v_i \end{bmatrix} = \begin{bmatrix} \cos\gamma & jZ\sin\gamma \\ j\sin\gamma/Z & \cos\gamma \end{bmatrix} \times \begin{bmatrix} F_i \\ v_i \end{bmatrix} \tag{3.9}$$

where F and v represent stress and particle velocity, respectively; subscript i and o represent input and output ports of the layer; Z and γ are the characteristic acoustic impedance and the phase delay of the layer [87]. With these transfer matrixes, the overall acoustic impedance of uniform multilayer loading Z_L can be calculated using Eq.(3.10):

$$\begin{bmatrix} F_{LR} \\ v_{LR} \end{bmatrix} = [B_1] \times [B_2] \times \cdots \times [B_n] \times \begin{bmatrix} F_{n+1} \\ v_{n+1} \end{bmatrix} \tag{3.10}$$

where $F_{n+1}=0$, since the top layer is exposed to air.

It should be noted that the above discussion is for the case of uniform multilayer loading on the entire sensor surface. In the application of the sensor system, however, the loading is often non-uniform in thickness. Lucklum and Hauptmann recently developed a model for sensors with non-uniform loading. In this model, the sensor is divided into several subunits and a uniform loading is applied on each subunit [90]. This model can be represented as an equivalent circuit in

which each subunit has its own motional impedance in parallel to the static capacitance C_o and all other motional impedances (**Figure 23**). According to Eqs. (3.5a) and (3.5b), the motional admittance of each subunit is proportional to C_{oi} therefore proportional to the area of each subunit S_i. The total motional electrical impedance of the resonator with non-uniform loading can be expressed as

$$Z_m^{total} = \frac{1}{\sum_{i=1}^{n} \frac{S_i / S_o}{Z_m^o + Z_m^{L_i}}} \tag{3.11}$$

where Z_m^o is the motional impedance of the unloaded resonator, $Z_m^{L_i}$ is motional impedance change if the loading on subunit i is uniformly applied onto the entire surface of the resonator and S_o is the area of the resonator electrode. Therefore, the motional electrical impedance change induced only by the non-uniform loading is given by

$$Z_m^{L_{total}} = \frac{1}{\sum_{i=1}^{n} \frac{S_i / S_o}{Z_m^o + Z_m^{L_i}}} - Z_m^o \tag{3.12}$$

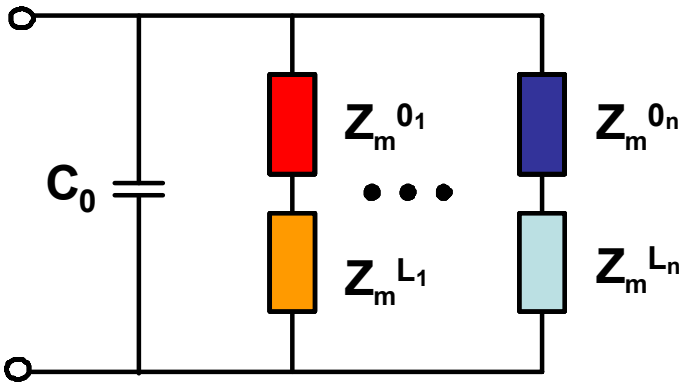

Figure 23. Equivalent circuit of TSM resonator with non-uniform loading

3.2.3 Physical model of cell adhesion onto the sensor surface and its acoustic loading impedance

Cells attach to the underlying substrate through complex transmembrane receptors, which connect the cytoskeleton to the extracellular matrix [91]. When cells are steadily adhered to the substrate, there exists an interfacial gap between cell basal membrane and substrate. The values of the interfacial gap vary with different contact types. According to surface plasmon resonance microscopy (SPRM) studies [92], the gap in focal contact area is only a few nanometers, while cell membrane is separated from the substrate about 30nm in close contact area and about 100-150 nm in the rest part of cells, respectively. Furthermore, it has been shown that the properties of cell medium on top of cell layer have minimal effect on the frequency shift and resistance change since the cell layer is relatively thick and the acoustic wave decays before reaching the cell medium [23]. Based on these considerations, it is reasonable to include 2 layers on the TSM resonator sensor surface: a finite interfacial gap and a semi-infinite cell layer. In addition, for simplicity, all the three layers are assumed uniform in the cell-covered area (Figure 24).

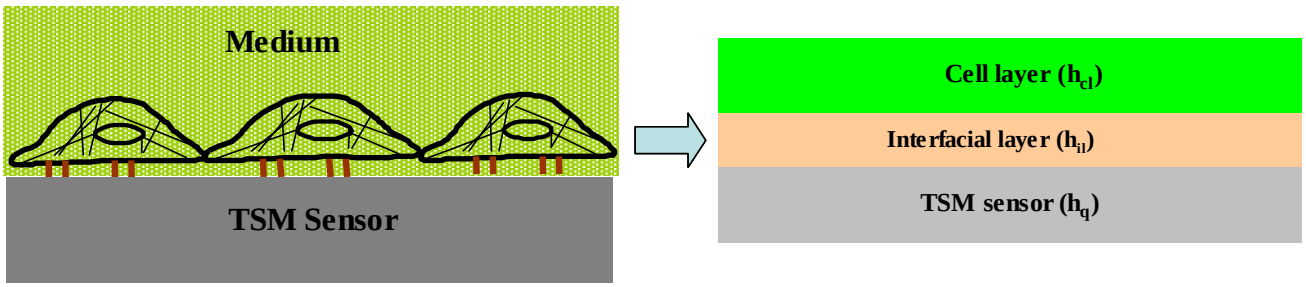

(a) (b)

Figure 24. (a) cell monolayer adhering to TSM sensor surface; (b) multilayer model of cell monolayer on sensor surface

For the case that cells attach on the entire surface of the resonator, the total acoustic loading impedance caused by the uniform interfacial layer and cell layer is given by,

$$Z_L = \sqrt{\rho_{il} G_{il}} \frac{\sqrt{\rho_{cl} G_{cl}} + j\sqrt{\rho_{il} G_{il}} \tan(\omega \sqrt{\frac{\rho_{il}}{G_{il}}} h_{il})}{\sqrt{\rho_{il} G_{il}} + j\sqrt{\rho_{cl} G_{cl}} \tan(\omega \sqrt{\frac{\rho_{il}}{G_{il}}} h_{il})} \tag{3.13}$$

where ρ, G and h are the density, complex shear modulus and thickness, respectively. Subscript *il* and *cl* represent the interfacial layer and cell layer respectively.

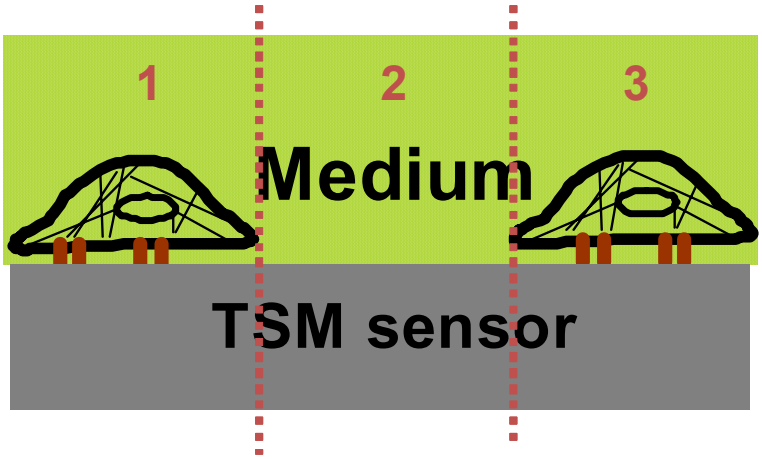

Figure 25. Non-uniform cell adhesion to TSM sensor surface

For the case that cells only attach on the partial surface of the resonator, we treated the loading as non-uniform loading **(Figure 25)**. In this case, we subdivided the sensor system into several subunits. On each subunit, the loading is uniform. For example, in figure 25, there are three subunits. The loading on subunits 1 and 3 are cell monolayer adhesion (a finite interfacial layer plus a semi-infinite cell layer), while that on subunit 2 is the semi-infinite medium. We can use an equivalent circuit shown in figure 23 to describe this model, in which each subunit has its own motional impedance in parallel with the motional impedance of all other subunits and external capacitance of the sensor. If the cell coverage ratio on the electrode area is A, according

to Eqs. (3.6), (3.7), (3.12) and (3.13), the total motional electrical impedance change induced by cell adhesion on partial resonator surface is

$$Z_m^{L_{total}} = \left(\frac{A}{Z_m^o + Z_m^{L_1}} + \frac{1-A}{Z_m^o + Z_m^{L_2}} \right)^{-1} - Z_m^o \tag{3.14}$$

where Z_m^o, $Z_m^{L_1}$ and $Z_m^{L_2}$ are the motional electrical impedance of the unloaded resonator, motional electrical impedance change induced by cell adhesion, and motional electrical impedance change by semi-infinite medium loading on the entire resonator surface, respectively. Further simplification of Eq.(3.14) leads to

$$Z_m^{L_{total}} = A \frac{Z_m^{L_1} - Z_m^{L_2}}{1 + (1-A)\dfrac{Z_m^{L_1} - Z_m^{L_2}}{Z_m^o + Z_m^{L_2}}} + Z_m^{L_2} \tag{3.15}$$

Since $Z_m^o >> Z_m^{L_1}$ and $Z_m^{L_2}$, Eq. (14) can be simplified as

$$Z_m^{L_{total}} = A(Z_m^{L_1} - Z_m^{L_2}) + Z_m^{L_2} \tag{3.16}$$

Eq. (16) indicates that the difference between $Z_m^{L_{total}}$ and $Z_m^{L_2}$ is proportional to the cell coverage *A*.

3.3 MATERIALS AND METHODS

3.3.1 Experimental setup

The experimental setup of TSM resonators for functional biosensors is schematically shown in **Figure 26**. Commercially available AT-cut quartz resonators (International Crystal

Manufacturing, Oklahoma City, OK) with the fundamental resonant frequency of 10MHz were used in this study. TSM resonators were inserted into a standard cell culture plate, which was placed in an incubator during the measurements. The measuring chamber was formed by putting a poly(dimethylsiloxane) (PDMS) tube, which can be self-sealed on the quartz surface, onto each resonator. The two electrodes were connected to an impedance analyzer (Agilent 4294A Precision Impedance Analyzer, Agilent Technologies, Palo Alto, CA) to measure the impedance spectra of the resonators. Prior to each experiment, the quartz crystal sensor device was sterilized with ethanol for half an hour and then washed with de-ionized water for three times. After that, they were dried with a stream of pressurized air and exposed to UV light for about 1 hour to sterilize the chamber.

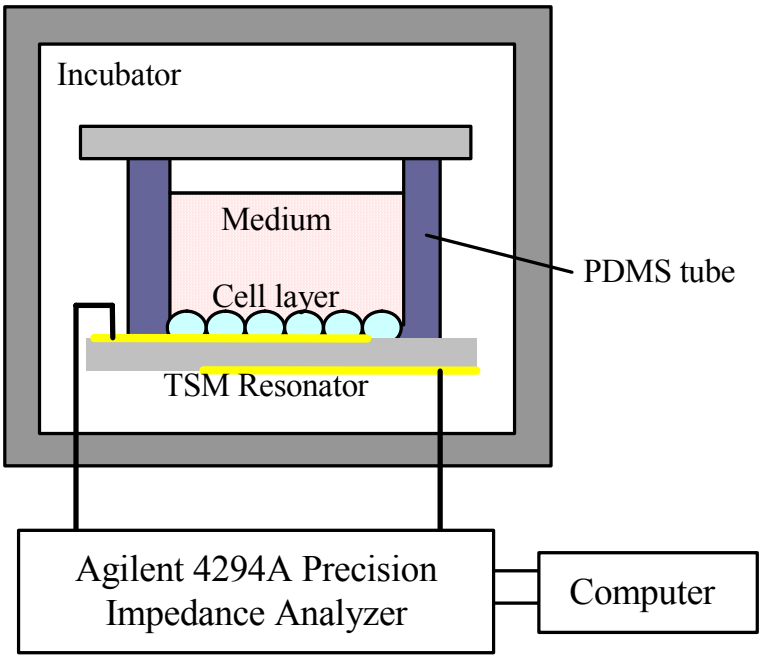

Figure 26. Experimental setup of thickness shear mode resonators for cell-based functional biosensor

3.3.2 Cell culture

Human skin fibroblasts were obtained from the American Type Culture Collection (ATCC, Manassas, VA 20110, USA) and grown in DMEM supplemented with 10% fetal bovine serum and 1% penicillin/streptomycin (Invitrogen, CA) in 5% CO_2 at 37^{o}C and 100% humidity in culture flask. The medium was changed twice a week. Once fibroblasts reached confluence, cells were sub-cultured by the standard trypsinization and centrifugation techniques. The passage of cells was from 7 to 10.

3.3.3 Monitoring cell attachment, spreading and formation of focal adhesion

The attachment and spreading of human skin fibroblasts were monitored after suspended cells were added onto the resonator surface. Prior to the deposition of cells, the electrical impedance spectra of uncoated resonators were measured. Cells were then trypsinized, centrifuged and counted with a hemacytometer. Cell-free medium was loaded into one sensor well as a control, at the same time medium containing cells with numbers of 7.5×10^4, 5×10^4, 3×10^4, and 1×10^4 was each added into the other sensor wells. Cell solutions were also added onto gold-coated glass slides under identical conditions as a simulation experiment. The electrical impedance spectra for each resonator sensor were recorded continuously. Images of cells on the gold-coated glass were recorded on a microscope with a CCD camera.

3.3.4 Cells with cytochalasin D (CD) treatment

20 hours after cells cultured on the resonator surface, cells were exposed to CD with concentration of 0 μM, 2.5 μM, 5 μM and 10 μM. The motional resistance for each resonator sensor was recorded continuously to monitor correspondingly the response of resonator sensors to CD treatment.

3.3.5 Immunostaining of actin filaments and nucleus

Cells treated with 5 uM CD for 3, 5, 10, 20 and 40 min were fixed with 4% paraformaldehyde (FD NeuroTechnologies, Ellicott City, MD) for 20 min, pretreated with 0.1% Triton-X100 for 2 min, and blocked with 5% bovine serum albumin for 1 h. The TRITC conjugated phalloidin was then applied at a dilution ratio of 1:100 for 45 min. The sample was washed extensively with PBS to remove excessive phalloidin. The DAPI was applied at a dilution ratio of 1:5000 for 1 min and then sample was washed extensively with PBS again. After that, the samples were examined with fluorescence microscopy (Eclipse TE2000-U, Nikon, Japan).

3.4 RESULTS

3.4.1 Modeling results for cell adhesion

The relative resistance change (ΔR_r) and frequency shift ($-\Delta f_r$) of TSM sensors due to cell attachment and adhesion with different cell-substrate contact as compared to cell free medium

can be simulated using the theoretical model. Since ΔR_r and $-\Delta f_r$ are proportional to cell coverage, it is sufficient to simulate the resistance and frequency responses for full cell coverage on the resonator surface. For simplicity, it is assumed that the viscoelastic property of the interfacial layer between cell and sensor substrate is the same as the cell medium (water). The resistance change ΔR_r as a function of the thickness (h_{il}) of interfacial layer at different viscosity and shear storage modulus of cell layer is calculated and plotted in **Figure 27(A)** and **(B)**, respectively. It can be found that ΔR_r increases with decreasing h_{il} from 300nm to 0. If a cell storage shear modulus value of 1Kpa is used, ΔR_r increases with increasing the viscosity of cell layer (**Figure 27 (A)**). If a cell viscosity value of 2cp is used, ΔR_r decreases with increasing the storage shear modulus of cells when h_{il} is greater than 90nm but increases when h_{il} is less than 90nm. Changes in storage shear modulus of cells do not induce significant resistance change (**Figure 27 (B)**). The frequency shift ($-\Delta f_r$) as a function of interfacial layer thickness is plotted in **Figure 27 (C)** and **(D)** at different viscosity and shear storage modulus of the cell layer, respectively. ($-\Delta f_r$) decreases first and then increases with the decrease of the thickness of interfacial layer h_{il} from 300nm to 0. For storage shear modulus value of 1KPa, ($-\Delta f_r$) decreases with increasing the viscosity of cells when h_{il} is greater than 60nm but increases when h_{il} is less than 60 nm (**Figure 27 (C)**). For a cell viscosity value of 2cp, ($-\Delta f_r$) always decreases with increasing the shear storage modulus of cells (**Figure 27 (D)**). It should be noted during the course of cell attachment and spreading, the thickness and property of interfacial layer and viscoelastic property of the cell layer are dynamic parameters. Clearly, the resistance change and frequency shift can be used as quantitative indications of the cell attachment and spreading on the sensor surface.

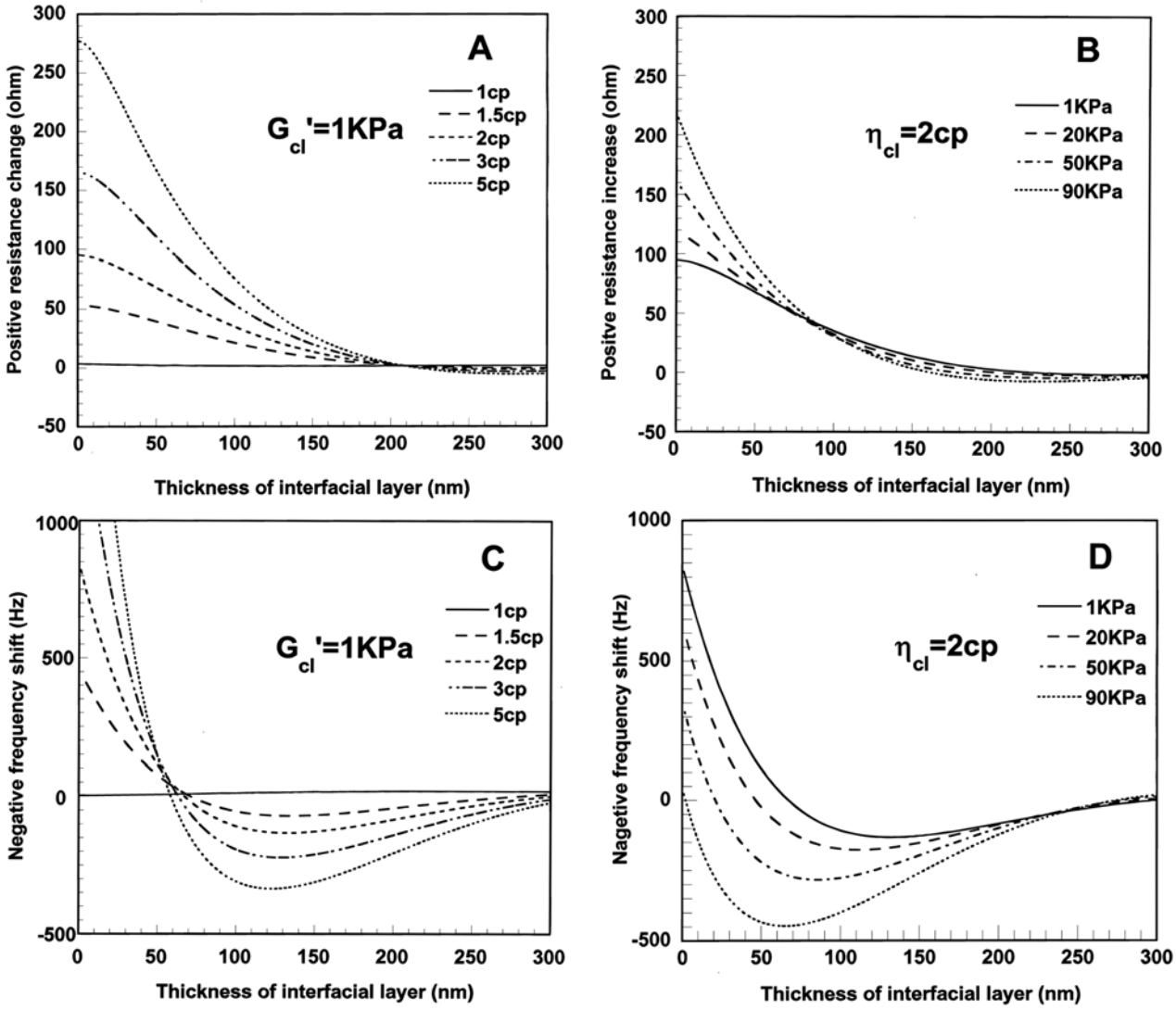

Figure 27. Modeling results of relative motional resistance increase and resonant frequency decrease to cell-free medium due to cell monolayer adhesion. (A) Relative resistance increase with changing thickness of interfacial layer and viscosity of cell layer when the storage shear modulus of cell layer is fixed to 1KPa; (B) relative resistance increase with changing thickness of interfacial layer and storage shear modulus of cell layer when the viscosity of cell layer is fixed to 2cp; (C) relative frequency decrease with changing thickness of interfacial layer and viscosity of cell layer when the storage shear modulus of cell layer is fixed to 1KPa; and (D) relative frequency decrease with changing thickness of interfacial layer and storage shear modulus of cell layer when the viscosity of cell layer is fixed to 2cp.

3.4.2 Process of cell adhesion after cells contact with a surface

The morphology of cells cultured on the gold-coated glass surface with different cell seeding densities was recorded at different culture time points using microscopy with CCD camera

(**Figure 28(A)**). For all seeding densities, cells are with spherical shapes and suspend in the medium a few minutes after the cell additions. Then, most of cells are found to attach onto the resonator surface during the first 10 min and then start spreading. For high seeding densities (cell number: 7.5×10^4 and 5×10^4), cells cover the entire resonator surface about 50 min after the cell addition. However, some cells do not have enough places to attach and spread at that time point. After that, the rearrangements occur and cell monolayer is formed finally at 500min. For the intermediate (cell number: 3×10^4) and low seeding density (cell number: 1×10^4), after cells attach to the surface, they spread continually until they establish cytoskeleton network and reach a steady adhesion state. During their spreading, there is no obvious rearrangement observed.

During the course of cell attachment, spreading and formation of a steady state of cell adhesions, both (ΔR_r) and ($-\Delta f_r$) experience four phases: fast increase stage, slow increase stage, decrease stage and steady state stage (**Figure 28(B) and (C)**). At the decrease stage, ΔR_r decreases much faster for high densities than the intermediate seeding density. There is only a very small decrease in (ΔR_r) at the low seeding density. However, ($-\Delta f_r$) decreases rapidly for all seeding densities at the decrease stage. In addition, (ΔR_r) and ($-\Delta f_r$) are dependent on cell seeding densities at fast increase stage except the highest one, while they are not significantly affected by seeding densities at the steady state stage.

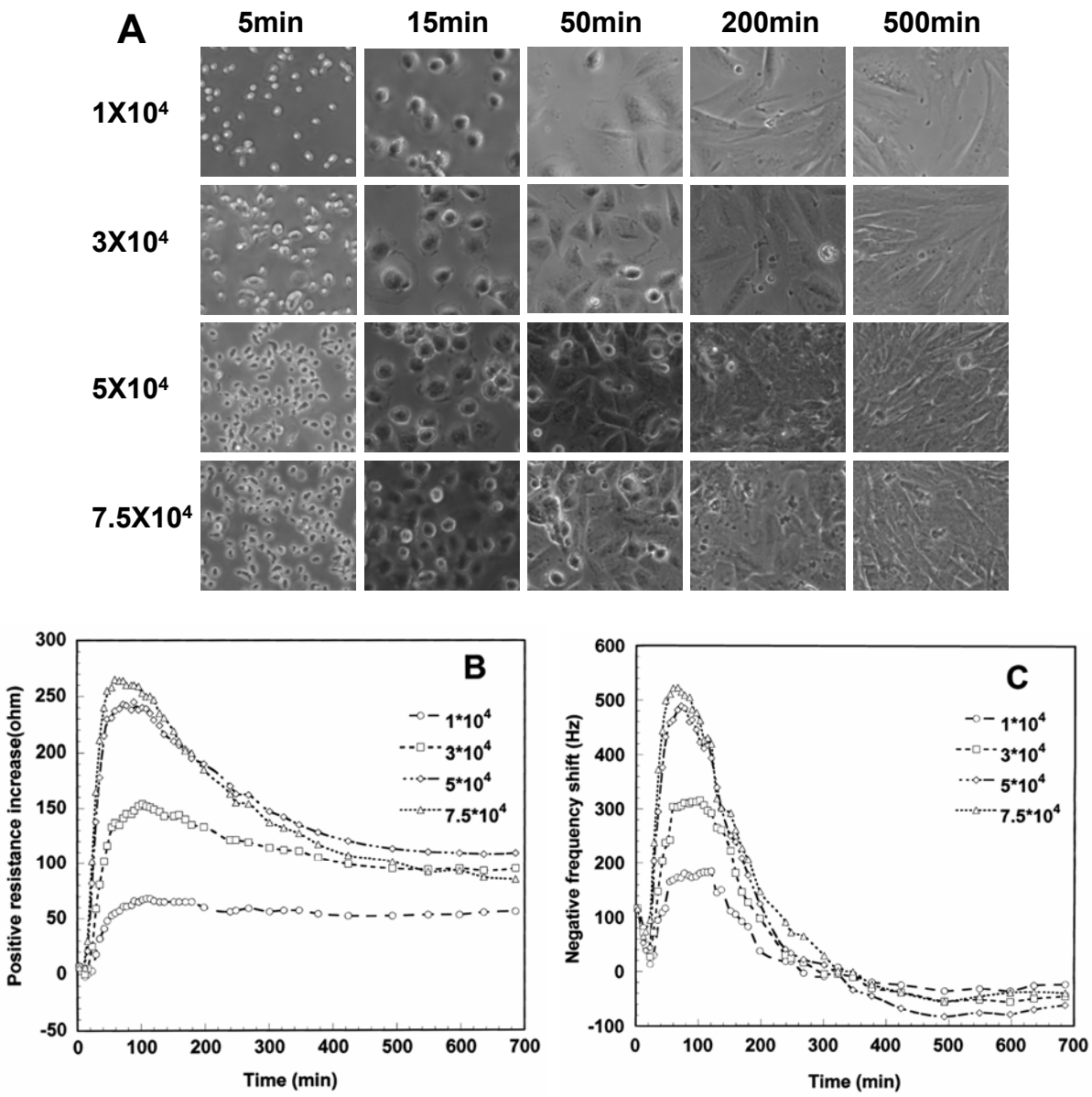

Figure 28. (A) Images of cells in culture at different time points; (B) time course of the relative motional resistance increase; and (C) relative resonant frequency decrease to the cell-free medium after different numbers of human skin fibroblasts seeded onto the resonator surface at time point zero

3.4.3 Cell layers with CD treatment

Cytochalasin D is a fungal toxin that severely disrupts network organization, increases the number of actin filament ends, and leads to the formation of filamentous aggregates (Schliwa,

1982). The actin stress fibers are distributed evenly and the actin filaments form end-to-side associations with other actin filaments for untreated cells (**Figure 29(A)**). However, after cells are treated with 5μM cytochalasin D, the filamentous network is rather non-uniformly distributed throughout the cell. The dense network aggregates form first in the cell periphery (**Figure 29(B), (C) and (D)**), and later throughout the cell body **(Figure 29(E) and (F)**). With a treatment longer than about 20 min, cells show the dissolution of stress fibers.

For 5μM Cytochalasin D treatment, motional resistance has a significant change after about 7-8 minute treatment as compared with the control experiment, and continuously shifts during the first hour. In addition, the values of resistance decrease after about 7-8 minutes are dosage dependent (**Figure 29(G)**).

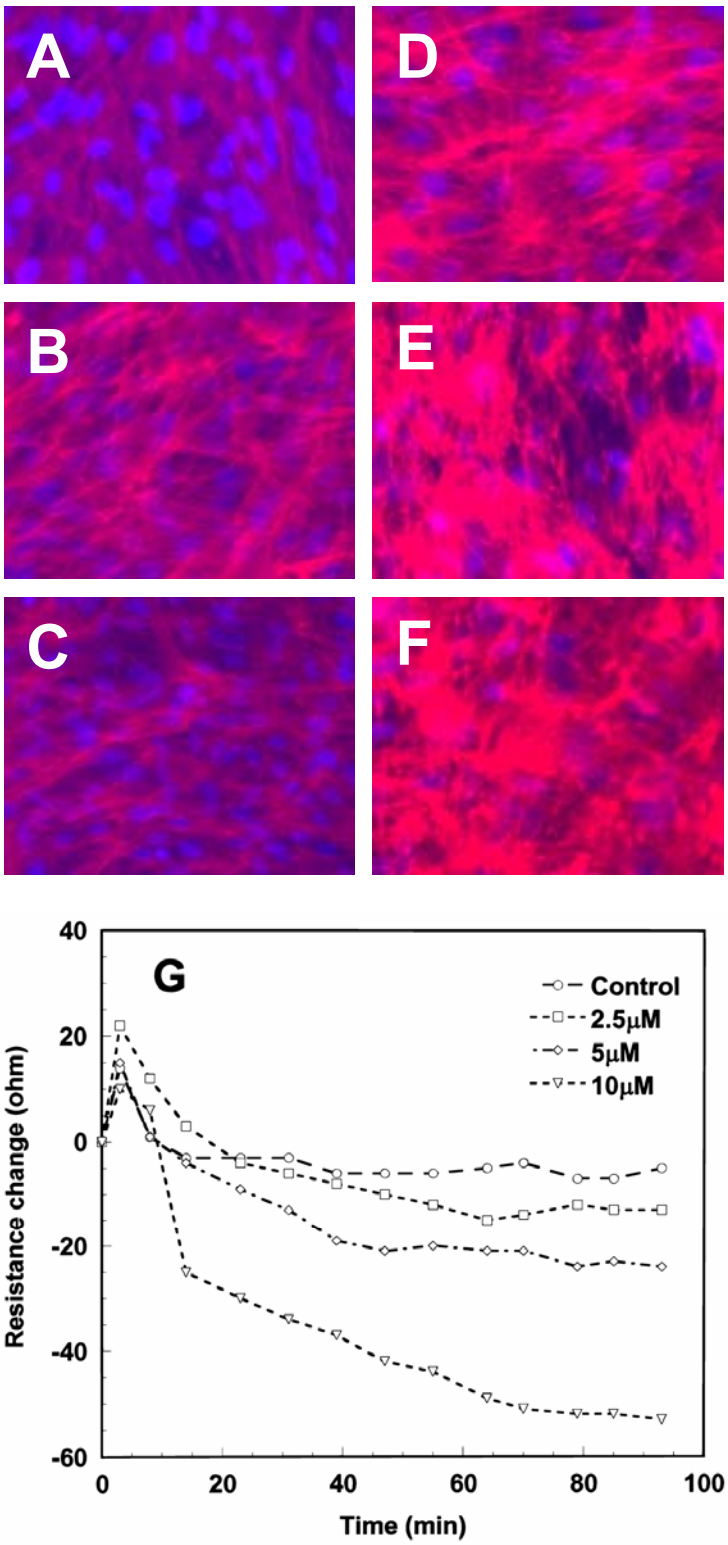

Figure 29. Florescence images of human skin fibroblasts exposed to 5uM cytochalasin D for different time: (A) 0min; (B) 3min; (C) 5 min; (D) 10 min; (E) 20 min; (F) 40min; and (G) changes in motional resistance after confluent human skin fibroblast layers treated with Cytochalasin D with different concentrations

3.5 DISCUSSIONS

Based on the modeling results, three factors are regarded to significantly affect the frequency and resistance responses during the cell attachment, spreading and formation of focal adhesions: cell-covered area, interfacial layer between the basal membrane and substrate, and cell mechanical properties. When a cell contacts with a surface, cell attachment occurs first, involving the interaction between integrins and substrate. Then cells increase their surface contact area with the substrate through formation of actin microfilaments and cell spreading [60]. It is observed under microscopy that cells attach onto the resonator surface and spread during the first hour of cell culture. Therefore, there are an increase in cell coverage on the sensor surface and a decrease in the thickness of interfacial layer. The measurement results indicate that both $-\Delta f_r$ and ΔR_r increase quickly. These experimental observations are consistent with our simulation results that $-\Delta f_r$ and ΔR_r increase with increasing cell coverage and decreasing h_{il}. In addition, at the fast increase phase, both ΔR_r and $-\Delta f_r$ are seeding-density dependent except the highest one (cell number: 7.5×10^4). The reason is that the cell-substrate contact and cell mechanical properties are similar for different seeding densities during this period, therefore ΔR_r and $-\Delta f_r$ are proportional to cell coverage, which is linearly dependent on the seeding densities before the coverage reaches 100%.

Cell images by microscopy show that 1 hour after cell addition, significant rearrangements occur because some cells cannot find a space to attach during the first hour for high cell seeding densities but no rearrangements at the low cell seeding density. It is believed that cell migration, and decrease in cell spreading area in order to allow more cells attaching on the surface during cell rearrangements increase the cell-substrate separation, which decreases $-\Delta f_r$ and ΔR_r according to the simulation results. Consistently, it is observed that there is a

significant decrease in $-\Delta f_r$ and ΔR_r measurements at high cell densities. However, for the low seeding densities (cell number: 1×10^4) it has been found that $-\Delta f_r$ decreases after cells cultured onto the resonator surface for 2 hours but no such a decrease appears in ΔR_r. This observation may be explained by examining the cell adhesion mechanism. Following spreading, cells proceed to organize their cytoskeleton as characterized by the formation of focal adhesions and actin-containing stress fibers. It is believed that the formation of actin stress fibers affects cell viscoelasticity, especially significantly increasing the storage shear modulus [67, 93]. The simulation results show that increasing storage shear modulus G'_{cl} slightly increases ΔR when h_{il} is less than 90nm, but slightly decreases ΔR when h_{il} is greater than 80nm. The effect of G'_{cl} on ΔR_r is not significant. However, increasing G'_{cl} significantly decreases $-\Delta f$. So the different responses of ΔR and $-\Delta f$ after cells cultured onto the resonator surface for 2 hours at the low seeding densities might be due to the increase in the storage shear modulus of cells. Therefore, the TSM resonator sensors can be used to detect the changes in cell viscoelastic properties, which plays an important role in cell migration, cytokinesis and cell mechanics [55, 67, 94].

The steady values of ΔR_r and $-\Delta f_r$ are not dependent on cell number. One possible reason is that the cell coverage is not proportional to cell number at the steady adhesion stage. Microscopic images at culture time point of 500 min have indicated that the spreading area of cells is different for different seeding densities. The lower the cell seeding density, the larger the individual cell spreading area is. In addition, the cell-substrate separation and cell mechanical properties could be different for different seeding densities, therefore the differences in the steady values of ΔR_r and $-\Delta f_r$ for different cell seeding densities are not only affected by cell coverage, but also by cell mechanical properties and the thickness of the interfacial layer. An interesting experimental observation at the steady adhesion stage is that for high cell seeding

densities (cell number: 7.5×10^4 and 5×10^4), the steady value of ΔR for cell number 5×10^4 is larger than cell number 7.5×10^4. Since the cell coverage is similar (100% coverage) for both cases, the larger steady value of ΔR for cell seeding density of 5×10^4 could be caused by a smaller cell-substrate separation and a larger value of storage shear modulus of cells.

Cells adhere to the substrate via adhesion proteins whose intracellular domain binds to cytoskeleton. Without attachment to the cytoskeleton, a cell adhesion protein could be hydrolyzed by extracellular hydrolytic enzymes and ripped out from the cell membrane. Therefore, cytoskeleton plays an important role in maintaining strong adhesion between cells and substrate. Since cytoskeleton is a three-dimensional network extending throughout the cytoplasm, it is considered as the determining factor for cell mechanical properties, especially the elastic part [66]. Fungal toxin cytochalasin D disrupts the actin cytoskeleton, as was shown by the fluorescent images. According to the simulation results, the resistance change is significantly affected by the thickness of interfacial layer, cell-covered area and viscosity of cells, but is less sensitive to the storage shear modulus. Therefore, the decrease in resistance after cytochalasin D treatment can be attributed to the loss of strong adhesion of cells with the substrate and the subsequent cell shape changes due to the cytoskeleton disruption.

3.6 CONCLUSIONS

In summary, a multilayer resonator sensor model was proposed to establish a relationship between the resonant frequency and resistance change of the TSM resonator induced by cell adhesion and spreading and the physical properties of the interfacial layer and the cell layer. By dividing the resonator into several subunits, we have first time theoretically shown that the

relative frequency and resistance changes to cell-free medium due to cell adhesion is linearly dependent on the cell coverage, which has also been observed by previous experimental studies. Experimentally, the dynamic processes of cell adhesions as functions of cells seeding densities have been investigated. By comparing the theoretical prediction on ΔR_r and $-\Delta f_r$ using the model with experimental results, the mechanism that is responsible for the changes in frequency and resistance during cell attachment, spreading and formation of strong adhesions has been discussed. Cell rearrangements involving cell migration at high seeding densities cause a large decrease in resistance and increase in frequency. The different responses of frequency shift and resistance change during the formation of actin stress fiber in cells indicate the changes in cell mechanical properties. Changes in cell-substrate contact and morphology induced by fungal toxin cytochalasin D decrease the motional resistance. This study has demonstrated that the thickness shear mode (TSM) acoustic wave resonator attached with living cells can be used, in real time, as an effective functional biosensing device to monitor the process of cell adhesion and spreading onto a surface, which are important in physiological and pathological processes [95]. It may also be used to measure cell mechanical properties and interfacial layer characteristics between cells and the substrate.

4.0 THICKNESS SHEAR MODE RESONATORS FOR CHARACTERIZING VISCOELASTIC PROPERTIES OF MC3T3 FIBROBLASTS MONOLAYER

4.1 INTRODUCTION

In chapter 3, we developed theoretical models of the thickness shear mode resonator sensors with cell monolayer adhesion and non-uniform cell adhesion on their surface. Experimentally, using thickness shear mode sensors, we investigated the dynamic procedure of cell attachment, spreading and formation of focal adhesion with different cell seeding densities. In addition, we monitored the changes in cell adhesion under cytoskeleton disruption. Our theoretical model and experimental studies have demonstrated that electrical signals of TSM resonator (e.g. resonant frequency, motional resistance, and electric impedance or admittance) are related to the viscoelastic properties of cell layer when they attach to the sensor surface. So in this chapter, we investigated the feasibility of characterizing cell viscoelasticity using TSM acoustic wave sensors.

Cell viscoelasticity, determined by lipid membranes and cytoskeleton, plays an important role in regulating many cell behaviors. A high-precision measurement of the cell viscoelasticity provides critical information to quantify the effect of drugs, mutations or diseases on cell structures [65]. As discussed in chapter 1, up to now, many techniques have been developed to measure the viscoelastic properties of cells, including atomic force microscopy (AFM) [96],

magnetic bead Microrheometry (MBM) [65, 97], micropipette [98], microneedles [99] and cell poker [100]. However, all of the above techniques directly apply mechanical forces on cells, therefore they are invasive methods. In addition, the system is complex and measurement is also time-consuming. Laser tracking microrheology, a non-invasive, fast and sensitive technique, was developed to quantify viscoelastic modulus of cells recently. Endogenous cellular particles were used as probes. However, it is hard to obtain the natural particles in cells that meet high requirements in terms of the location or dimensions [64]. Therefore, it is highly desirable to develop a non-invasive, simple and fast tool to characterize cell viscoelasticity. So in this chapter, we characterized the viscoelastic properties of MC3T3 fibroblast momolayer with TSM quartz resonators. In order to obtain comprehensive and detailed information on the resonator oscillation, the impedance over a range of frequencies near resonance were measured by the impedance analyzer instead of only measuring the resonance frequency and motional resistance with an oscillation circuit. After cells were fully spread to form a monolayer on the surface, the viscoelastic properties of the cell monolayer were evaluated by fitting experimental admittance curves with those obtained from the theoretical model. Compared with other techniques, our results demonstrated that TSM acoustic wave sensor provides a reliable tool to characterize cell viscoelasticity in a non-invasive, fast and simple way.

4.2 MATERIALS AND METHODS

4.2.1 Experimental setup

In the experimental setup of TSM resonators for functional biosensors **(Figure 26)**, the AT-cut quartz resonators with the fundamental frequency of 5MHz are commercially available (Stanford Research Systems Inc., Sunnyvale, CA). TSM resonators were inserted into a standard cell culture plate, which was placed in an incubator during the measurements. The measuring chamber was formed by putting a poly(dimethylsiloxane) (PDMS) tube, which can be self-sealed on the quartz surface, onto each resonator. The two electrodes were connected to an impedance analyzer (Agilent 4294A Precision Impedance Analyzer, Agilent Technologies, Palo Alto, CA) to measure the admittance spectra of the resonators. Prior to each experiment, the quartz crystal sensor device was sterilized with ethanol for half an hour and then washed with de-ionized water for three times. After that, they were dried with a stream of pressurized air and exposed to UV light for about 1 hour to sterilize the chamber.

4.2.2 Cell Culture

MC3T3-E1 cells (ATCC, Manassas, VA) were grown in the α-MEM growth medium (Invitrogen, Carlsbad, CA) supplemented with 10% fetal bovine serum (Invitrogen, Carlsbad, CA), 100units/ml penicillin, and 100 μ g/ml streptomycin (Sigma, St. Louis, MO). The cells were maintained at 37^{o}C in a humidified atmosphere of 95% air and 5% carbon dioxide. For all experiments, cells were plated on the sensor surface at an initial density of 2×10^{4} cells/cm^{2}.

4.2.3 Measurements

Prior to the deposition of cells, the electrical admittance spectra and total parallel capacitance of the uncoated resonators and water-loaded resonators were measured first. Then the electrical responses of resonators with α-MEM growth medium solution were measured to characterize the properties of the solution. 24 hours after cell-free medium and cell medium were added onto each resonator surface, the admittance spectra and the total parallel capacitance of each resonator sensor were recorded.

4.3 DETERMINATION OF THE VISCOELASTIC PROPERTIES OF CELL LAYERS

According to Eq. (3.3), without taking any approximation, the input electrical impedance of TSM resonators with loading on one side can be expressed as an equivalent circuit consisting of a static capacitance C_0 parallel to motional impedance Z_m. Because the fixture and cable induce an external capacitance that has to be considered here, the generalized input electric admittance of resonator sensors is rewritten as

$$Y = G + jB = j\omega C_0^{*} + \frac{1}{Z_m} \tag{4.1}$$

where C_0^{*} is the total parallel capacitance of resonators, which is the sum of the static capacitance C_0 and the external parallel capacitance C_{ex}, and Z_m is the impedance of the motional branch [25]. The motional impedance can be rewritten based on Eq. (3.3):

$$Z_m = \frac{1}{j\omega C_0}\left(\frac{1 - j\frac{Z_L}{Z_q}\cot\alpha}{\frac{K^2}{\alpha}\left[2\tan\frac{\alpha}{2} - j\frac{Z_L}{Z_q}\right]} - 1\right) \tag{4.2}$$

As discussed in chapter 3, the total acoustic loading impedance caused by the uniform interfacial layer and cell layer is given by

$$Z_L = \sqrt{\rho_{il}G_{il}}\frac{\sqrt{\rho_{cl}G_{cl}} + j\sqrt{\rho_{il}G_{il}}\tan(\omega\sqrt{\frac{\rho_{il}}{G_{il}}}h_{il})}{\sqrt{\rho_{il}G_{il}} + j\sqrt{\rho_{cl}G_{cl}}\tan(\omega\sqrt{\frac{\rho_{il}}{G_{il}}}h_{il})} \tag{4.3}$$

where ρ, G and h are the density, complex shear modulus and thickness respectively. Subscript il and cl represent interfacial layer and cell layer respectively.

4.3.1 Generic consideration for determining the viscoelastic properties of cell monolayer

According to Eq. (4.2), the input admittance of the resonator with loadings is determined by the quartz parameters (e_{26}, ε_{22}, c_{66}, ρ_q, h_q, A and η_q) and the surface acoustic loading impedance Z_L. Of all quartz parameters, e_{26}, ε_{22}, c_{66} and ρ_q can be obtained from the literatures, while h_q, A and η_q must be calculated by sensor calibration because these parameters are affected by the electrodes, fixtures et al. Z_L is the only 'foreign parameter' in Eq. (4.1), which are dependent on the material properties of loading layers shown in Eq. (4.3). Therefore, the input admittance of the resonator can be calculated when the properties of the loading layers and quartz parameters are known. However, for the resonators as sensors, we have to extract the properties of the loading layers from the measurement of the electric admittance spectra. For the cell monolayer on the sensor surface, the sensor structure includes the quartz resonator, finite interfacial layer and semi-infinite cell layer. In this three-layer model, there are seven unknown parameters in

acoustic loading impedance. Four of them correspond to the interfacial layer (ρ_{il}, h_{il}, G_{il}' and G_{il}'') and three to the cell layer (ρ_{cl}, G_{cl}' and G_{cl}''). In these seven parameters related to loading layers, the density and shear modulus of interfacial medium layer can be characterized by loading the cell culture medium alone onto the resonator surface and furthermore we assume the density of cell monolayer is the same as water. Therefore, the unknown parameters can be reduced to three: h_{il}, G_{cl}', and G_{cl}''.

4.3.2 Algorithmic strategy of exacting the viscoelastic parameters of cell layer

The algorithmic strategy of extracting parameters of loading layers on TSM resonators from the measurement of the electric admittance spectra has been developed recently by Yolanda Jimenez et al.[101], which is used for extraction of the viscoelasticity of cell monolayer in this dissertation. Basically, there are three steps: sensor calibration, interfacial layer characterization, and calculating the shear modulus of cell layers **(Figure 30)**. In the following, I will briefly describe these three steps.

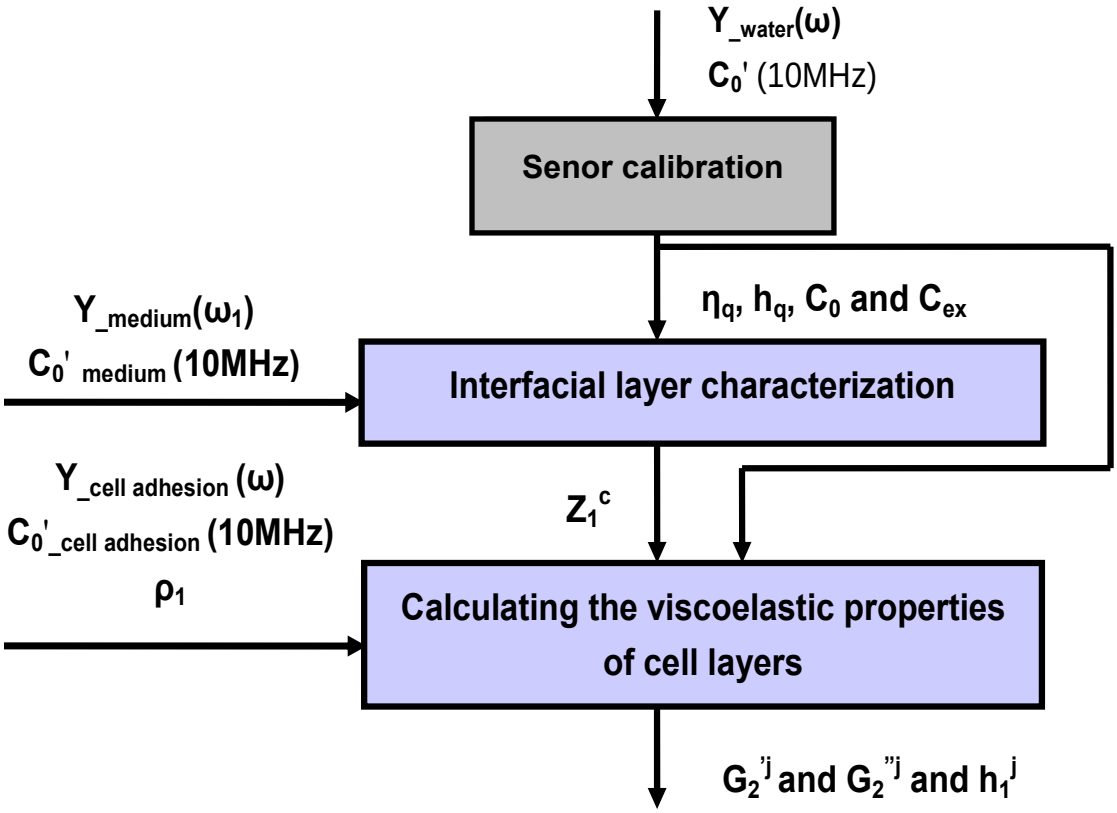

Figure 30. Flow chat for exacting the properties of loading layers from the measurements of the electric admittance spectra of TSM resonators.

Sensor calibration

As mentioned, before extracting the viscoelastic parameters of cell layers, a calibration process is carried out to calculate the effective TSM resonator's parameters. The inputs include electric admittance spectrum of the resonator sensor only in contact with water, the total parallel capacitance C_0^* and the characteristic impedance of water. The outputs are the effective quartz parameters, including the quartz's thickness (h_q), viscosity (η_q), static capacitance (C_0) and external capacitance (C_{ex}). The calibration process is as follows: (a) The admittance spectrum $Y(\omega_i)$ of the water-loaded resonator is measured by using the impedance analyzer (where i=1 to

M with M the number of frequency points). C_0^* is measured at two times of fundamental resonant frequency. $Z_m(\omega_0)$ is then obtained from Eq. (4.1). (b) In a reasonable range, η_q is discretized into η_q^j (where j=1 to n with n is the number of η_q). At first, a high range is tried. Then it can be reduced to a lower range for precision requirement after several tries. (c) According to Eq. (4.2), C_0 can be expressed as

$$C_0 = \frac{1}{j\omega Z_m}\left(\frac{1 - j\frac{Z_L}{Z_q}\cot\alpha}{\frac{K^2}{\alpha}\left[2\tan(\alpha/2) - j\frac{Z_L}{Z_q}\right]} - 1 \right) \tag{4.4}$$

For each $Z_m(\omega_0)$ and η_q^j, the thickness h_q^j is obtained through canceling the imaginary part of Eq.(4.4). A Regula-Falsi based algorithm is applied for getting the values of h_q. For each (η_q^j, h_q^j), the corresponding values of C_0^j are obtained from Eq. (4.4). (d) The solution of parameters (η_q, h_q, C_0) is obtained as the one that make the smallest admittance spectrum error between theoretical and experimental values. The error function is defined as follow:

$$Error\big|_j = \frac{\sum_{i=1}^{M}(G(\omega_i)\big|_{EXP} - G(\omega_i)\big|_j^{MODEL})^2 + \sum_{i=1}^{M}(B(\omega_i)\big|_{EXP} - B(\omega_i)\big|_j^{MODEL})^2}{\sum_{i=1}^{M}(G(\omega_i)\big|_{EXP})^2 + \sum_{i=1}^{M}(B(\omega_i)\big|_{EXP})^2} \tag{4.5}$$

Interfacial layer characterization

According to our model, there is an interfacial layer between cells and the substrate. We assume that the properties of this interfacial layer are the same as those of the cell culture medium. Therefore, for interfacial layer characterization, the inputs include the calibration parameters obtained from the sensor calibration, and the electrical admittance spectrum and total parallel capacitance of the resonator loaded with the cell culture medium only. According to Eqs. (4.1) and (4.2), the acoustic impedance of medium loading Z_L can be easily calculated. Since

$Z_L=(j\rho_{il}G_{il}'')^{1/2}$ and the density of cell culture medium ρ_{il} is known from the literature, the values of G_{il}'' are obtained. G_{il}' is equal to zero if the interfacial layer is assumed as a Newtonian liquid layer. Therefore, finally, we obtain ρ_{il}, G_{il}' and G_{il}''.

Calculating the viscoelastic properties of cell monolayers

The calculation of the shear storage and loss modulus of cell layer is similar with the sensor calibration procedure [101]. From Eq.(4.3), we can get

$$m_s(\omega)=\rho_{il}h_{il}=-\frac{\sqrt{\rho_{il}G_{il}}}{2j\omega}\left[\ln(r)+j(\theta+2k\pi)\right] \tag{4.6}$$

where

$$r(\omega)=\left|\frac{(\sqrt{\rho_{il}G_{il}}+\sqrt{\rho_{cl}G_{cl}})}{\sqrt{\rho_{il}G_{il}}+\sqrt{\rho_{cl}G_{cl}}}\times\frac{\sqrt{\rho_{il}G_{il}}-Z_L(\omega)\big|_{EXP}}{\sqrt{\rho_{il}G_{il}}+Z_L(\omega)\big|_{EXP}}\right| \tag{4.7a}$$

$$\theta(\omega)=phase(\frac{(\sqrt{\rho_{il}G_{il}}+\sqrt{\rho_{cl}G_{cl}})}{\sqrt{\rho_{il}G_{il}}+\sqrt{\rho_{cl}G_{cl}}}\times\frac{\sqrt{\rho_{il}G_{il}}-Z_L(\omega)\big|_{EXP}}{\sqrt{\rho_{il}G_{il}}+Z_L(\omega)\big|_{EXP}}) \tag{4.7b}$$

with $-\pi\le\theta\le\pi$, and k=0, ±1, ±2, ….

The extraction process includes the following steps:

(a) The admittance spectrum $Y(\omega_i)$ of the resonator with cell monolayer adhesion, is measured by using the impedance analyzer (where i=1 to M with M the number of frequency points). C_0^* is measured at two times of fundamental resonant frequency. $Z_L(\omega_i)\ |_{EXP}$ is obtained from Eqs. (4.1) and (4.2).

(b) In a reasonable range G_{cl}' is discretized into $G_{cl}^{j'}$ (where j=1 to n with n is the number of G_{cl}').

(c) At $\omega=\omega_0$ (angular resonant frequency), for each G_{cl}^{j}', G_{cl}^{j}" is obtained through canceling the imaginary part of $m_s(\omega_0)$. For each (G_{cl}^{j}', G_{cl}^{j}"), the corresponding values of h_{il}^{j} are obtained from Eq. (4.6).

(d) The solutions of G_{cl}^{j}', G_{cl}^{j}" and h_{il}^{j} with the value of Eq.(4.4) over 0.5% are ignored.

4.4 RESULTS AND DISCUSSIONS

The quartz parameters are extracted first by sensor calibration. For three different quartz resonators, the effective thickness and the static capacitance are similar. However, the effective viscosities are different, which may be caused by different fixtures and surface toughness **(Table 4).**

Table 4 Quartz parameters by sensor calibration

Experiment number	Effective viscosity	Thickness (μm)	Static capacitance (pF)
#1	0.0398	332	4.1352
#2	0.0239	332	4.57
#3	0.0378	332	4.41

24 hours after MC3T3-E1 cells cultured on the 5MHz TSM resonator surface, the viscoelastic properties of the cell monolayer are extracted based on the methods discussed in section 4.3. It is found that the values for G_{cl}', G_{cl}" and h_{il} obtained have wide ranges although the theoretical values fit the measurements very well after each group of solution (G_{cl}^{j}', G_{cl}^{j}" and h_{il}^{j}) is plugged in the model (the error is less than 0.5%) (**Figure 31**). The wide ranges of G_{cl}',

G_{cl}" and h_{il} indicate that it is hard to extract three unknown parameters of loading layers at the same time using the admittance spectra near resonant frequency. However, if the thickness of the interfacial layer is known, the storage and loss shear modulus of the cell monolayer can be obtained based on the relationships shown in **Figure 32**. Giebel *et al.* has reported that the values of cell-substrate distance obtained with surface plasmon resonance microscopy are, respectively, 25nm for close contact and 160nm for the other part of cells [92]. It has also been reported by Izzard and Lochner that the cell-substrate distance is about 30nm for the close contact, and is 100-140 nm for other regions of fibroblasts with interference reflection microscopy (IRM) [102]. And impedance measurements by cell-substrate electrical impedance sensing system showed that the average cell-substrate distances were from 30-80 nm for fibroblasts [61]. In this study, we assume the thickness of the interfacial layer between cell and substrate is in the range of 30-80nm. The storage and loss shear modulus are therefore obtained. Three individual experiments under the same conditions show similar results **(Table 2).**

Table 5 The extracted viscoelastic properties of cells for three individual experiments

Experiment number	G' (KPa)	G" (KPa)	$\eta = G'' / \omega$(cp)
#1	21-30	49	1.56
#2	24-32	48	1.52
#3	24-37	29-35	0.92-1.11

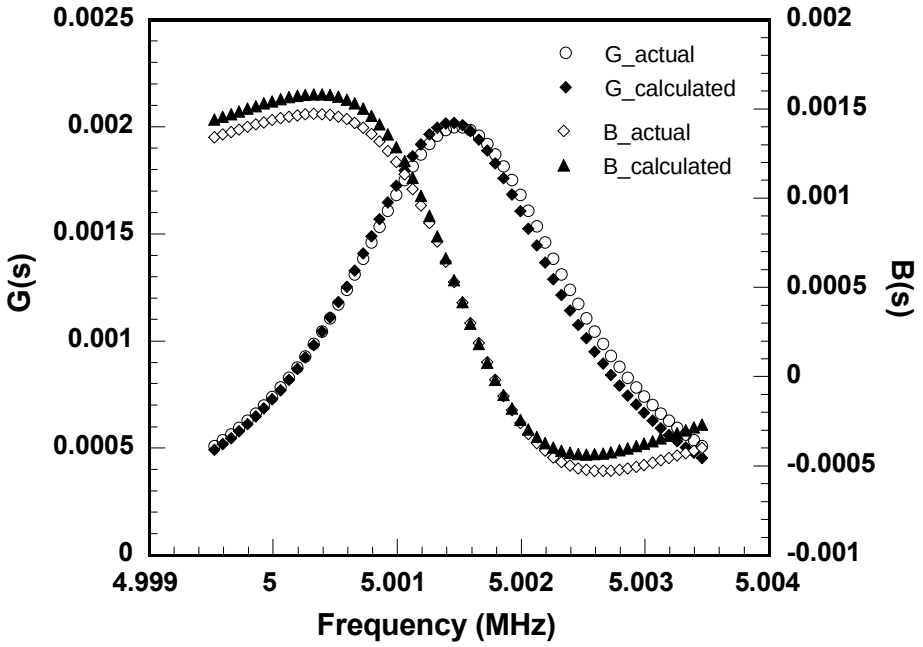

Figure 31. Comparison of G (real part of the electrical admittance) and B (imaginary part of the electrical admittance) spectra for the resonators with cell adhesion between the actual experimental measurements and calculated values by plugging the solutions into our theoretical model.

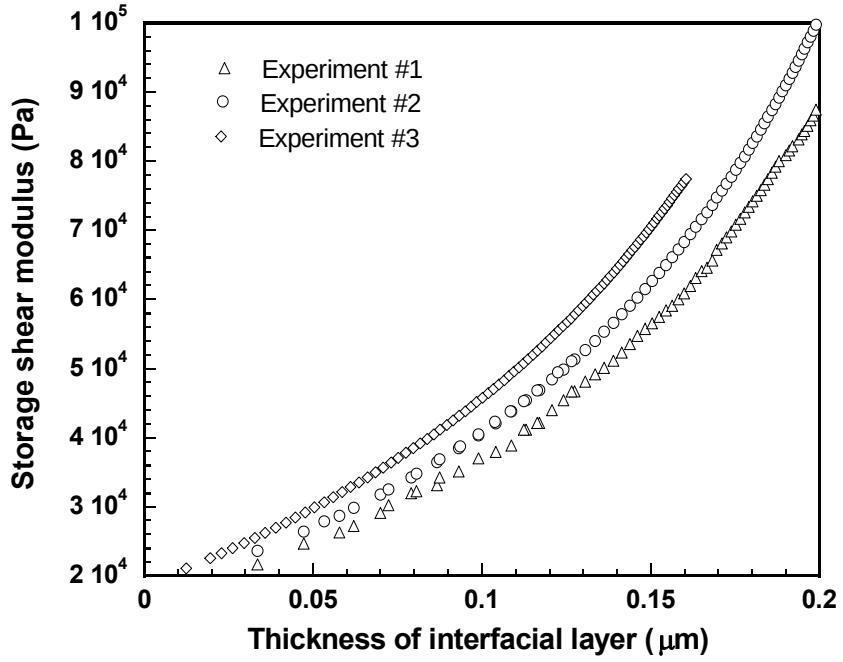

(A)

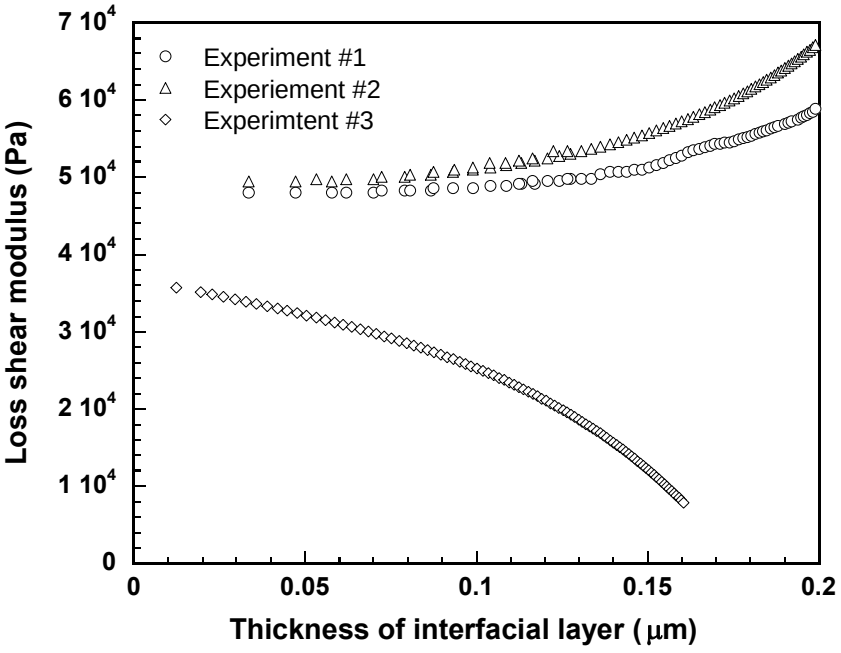

(B)

Figure 32. The relationship between extracted values of the thickness of interfacial layer and storage shear modulus (A) and between extracted values of the thickness of interfacial layer and loss shear modulus (B).

Table 6 Comparison of cell storage and viscosity with different techniques

Method	Cell type	G' (KPa)	Viscosity (cp)	Measured frequency (Hz)	Model for exacting cell viscoelasticity	Ex-ternal Force	Re-ference
TSM	MC-3T3	21-38	0.92-1.56	5M		No	Our study
Magnetic Bead Micro-rheometry	NIH 3T3	20-40	4×10^{6}		Finite springs and dashpots model	Yes	[65]
Magnetic Bead Micror-heometry	Airway smooth muscle cells	4	1.4×10^{3}	10	Power-law structural damping model	Yes	[75]
Microplate	Fibroblast s	0.96	1.1×10^{7}		Finite springs and dashpots model	Yes	[73]
AFM	Airway smooth muscle cells	1.2	5.1×10^{3}	10	Power-law structural damping model	Yes	[96]

Table 6 (continued)

AFM	Human lung epithelial cells	1	1.68×10^3	10	power-law structural damping model	Yes	[104]
	Chinese hamster ovary (CHO) cells		1.0-1.4			No	[105]
Micro-fluori-metry	Swiss 3T3 fibroblast		1.0-1.4			No	[106]
	Mono-nuclear cell		1.0-1.5			No	
	Swiss 3T3		0.9-1.3			No	
	MDCK		0.8-1.2			No	

Our results are compared with those by other techniques, such as microplate method, AFM, MBM and micro-fluorimetry (**Table 6**). Earlier techniques for characterizing cell viscoelasticity include micropipette aspiration, magnetic cytometry and microplate manipulation,

in which the creep response and stress relaxation are measured and the simple viscoelastic models with finite springs and dashpots are used to explain the experimental results [65, 73, 107]. More recently, dynamical viscoelastic properties of cells are characterized using magnetic twisting cytometry and atomic force microscopy [75, 96, 104]. In these studies, the complex shear modulus (G*(ω)) from oscillatory measurements over a frequency range is measured. G*(ω) is defined as the complex ratio in the frequency domain between the applied stress and the resulting strain. The functional dependence of modulus of cells is described by the power-law structural damping model:

$$G^*(\omega) = \overline{G_0}(1 + i\eta)\left(\frac{\omega}{\omega_0}\right)^{\alpha} + i\omega\mu \tag{4.8}$$

where η is the hysteresivity or structural damping coefficient of the model, α is the power-law exponent, and $\overline{G_0}$ and ω_0 are scale factors for the moduli and frequency respectively [75, 96, 104]. This model shows that the storage modulus follows a power law with exponent α and the loss modulus has the same power-law dependence on the frequency with an additional Newtonian viscous term. At low frequencies, the loss modulus increases proportionally to G' (ω) while at high frequencies G'' (ω) is dominated by the viscous term and approaches the linear dependence of a Newtonian fluid.

Our measurements show the elastic shear modulus of cells at 5MHz is about 21-38KPa. Dynamic measurements by AFM and MBM reveal the values for cell elastic modulus in the range of 1-4 KPa at 10 Hz. According to Eq. (4.8), the elastic shear modulus has a power law with exponent α, whose value is in the range of 0.15-0.35 according to previous experimental results [75, 96, 104]. If we choose α=0.25 and G_{cell}'~30K at 5MHz in our case, we can calculate G_{cell}'=1.1K at 10Hz, which is similar with the results by the dynamic measurement using AFM

and MBM at the same frequency range. However, the value by MBM and a simple viscoelastic model with finite springs and dashpots in Bausch's study is about 20-40KPa at quasi-static state, about one order of magnitude larger than the dynamic measurements and our study [65]. Studies by Desprat et al. have shown that viscoelastic properties extracted by different mathematic models are quite different even though the experimental creep or stress relaxation curves are obtained by the same microplate methods [108]. They conclude that the cells cannot be thought as a viscoelastic medium with a few characteristic relaxation time constants as the finite springs and dashpots models describing, but a viscoelastic medium with a wide and continuous spectrum of relaxation time constants. The viscoelastic properties of cells obtained by finite springs and dashpots model may not be reliable.

For the viscosity of cells, our results agree with those by micro-fluorimetry, which is a non-invasive method to characterize viscosity of cell cytoplasm at very high frequencies. This agreement is reasonable since cell viscosity in our study is measured at high frequency, which has been shown relating to cytoplasm fluid. However, the value of Newtonian viscous term μ in Eq. (4.8), indicating cell viscosity at high frequencies, by dynamic measurements with AFM and magnetic bead microrhemethy is about three orders of magnitude larger than our results. Since the dynamic measurements with AFM and MBM are implemented at relative low frequencies and μ value shows cell viscosity at high frequencies, the method for calculating μ value by fitting Eq. (4.8) to the experimental values of $G^*(\omega)$ at relative low frequencies might cause errors. In addition, the large probes in AFM and MBM may overestimate cell viscosity. Cell viscosity by the static measurements and finite springs and dashpots models is even larger, about seven orders larger than our results. Since the viscosity of cell is related to cytoskeleton at low frequencies but related to cytoplasm fluid at high frequencies [109], the values of cell viscosity in our studies and

static measurements are related to the properties for different cellular structures. Another reason is as we discussed, the finite springs and dashpots model might not be good enough to describe cell viscoelasticity, making the results not reliable.

4.5 CONCLUSIONS

The present study has demonstrated that the TSM resonator can be effectively used as a functional biosensor to determine viscoelastic properties of living cells. At the steady state of the confluent cell layer adhering to the substrate, a theoretical model consisting of two uniform layers (a finite uniform medium layer and a semi-infinite uniform viscoelastic cell layer) loaded on the resonator surface is proposed to relate the electric response of resonators to mechanical properties of cell layers. Using this model, the theoretical values of the resonator admittance near resonance are fitted with the measured spectrum, and the viscoelastic properties of cell layers are obtained. The results are reasonable compared with other techniques. In addition, the acoustic wave resonator sensor has advantages of experimentally simple and non-invasive over other techniques used to measure mechanical properties of cells.

However, in this study, the cell viscoelasticity cannot be obtained if the thickness of the interfacial layer is unknown. The properties of interfacial layer are assumed to be the same as those of cell culture medium, which may cause errors. In the future, the quartz TSM resonator can be combined with electrical impedance sensing system, which can measure cell-substrate separation, to characterize the cell viscoelasticity. The properties of interfacial layer could be characterized by measuring the electrical response of TSM resonators at higher order resonant frequencies so that the acoustic wave only penetrates into the interfacial layer.

5.0 LOVE MODE SURFACE ACOUSTIC WAVE DEVICE AS CELL-BASED BIOSENSOR

5.1 INTRODUCTION

In chapters 3 and 4, we have discussed the application of thickness shear mode bulk acoustic wave sensors for monitoring cell adhesion and characterizing cell viscoelasticity. Is it possible to use the surface acoustic wave devices as cell-based sensors for cell biological studies? What are the advantages and disadvantages of surface acoustic wave devices as cell-based biosensors compared with thickness shear mode bulk acoustic wave devices? Of various types of surface acoustic wave devices, wave-guided shear-horizontal surface acoustic wave device have attracted more and more attention due to their advantages over other acoustic wave devices for sensing applications in liquid, such as high sensitivity, mechanical robustness, and the protection of the IDTs due to the use of the waveguide layer. As talked in chapter 1, wave-guided shear-horizontal surface acoustic wave (also called Love mode) devices use piezoelectric substrate with inter-digital transducers (IDTs) deposited on one side of the surfaces to produce the shear-horizontal acoustic waves. In order to prevent the energy lost into the bulk material, a material layer with a slower acoustic velocity as a waveguide are deposited on it to trap the acoustic energy near the surface **(figure 12)** [3, 31]. However, the current investigation on Love mode biosensors is still far from mature, for both the theoretical and experimental studies. Most of

studies are limited to the use of Love mode devices as mass sensors. No studies have been performed to probe cell behaviors and properties using Love mode devices so far. In this chapter, we developed a theoretical model to optimize the sensor performance and predict the electrical signals changes (e.g. resonant frequency and attenuation) due to cell adhesion to the sensor surface. Experimentally, we fabricated Love mode acoustic wave device and experimentally demonstrated the validity of our theoretical model.

5.2 THEORETICAL MODELING OF CELL-BASED LOVE MODE ACOUSTIC WAVE SENSORS

As discussed in chapter 1, up to now, there are several methods developed to theoretically describe Love mode acoustic wave sensors, including analytical method [26, 27], perturbation method, [3, 28, 29], and transmission line method [30]. These methods have their limitations. For example, the analytical method is computationally complex and difficult to relate the changes in the loading to corresponding changes in electrical signals of the device, especially in the case of considering the loss of materials. Perturbation method assumes the changes in the system parameters are very small. Therefore, the perturbation method is limited to the modeling of the small changes of physical parameters in the system. The transmission line model has been applied for the modeling of Love mode acoustic wave devices as sensors [31]. It has been demonstrated that this model can describe the behavior of the sensor loaded by viscoelastic masses in a viscous liquid. However, the calculation is still complex. Therefore, it is necessary to develop an accurate and efficient method to describe the Love mode acoustic wave sensors with various loading, especially multi-viscoelastic layer loading. The transfer-matrix method is used

when the total system can be broken into a sequence of subsystems that interact only with adjacent subsystems. In our previous studies, it has been successfully used in the modeling of quartz thickness shear mode resonators as cell-based sensors [110]. It is a simple method for modeling the acoustic wave devices, especially for the multilayer structures. So the transfer matrix method is suitable for the analysis of Love mode devices as cell-based biosensors.

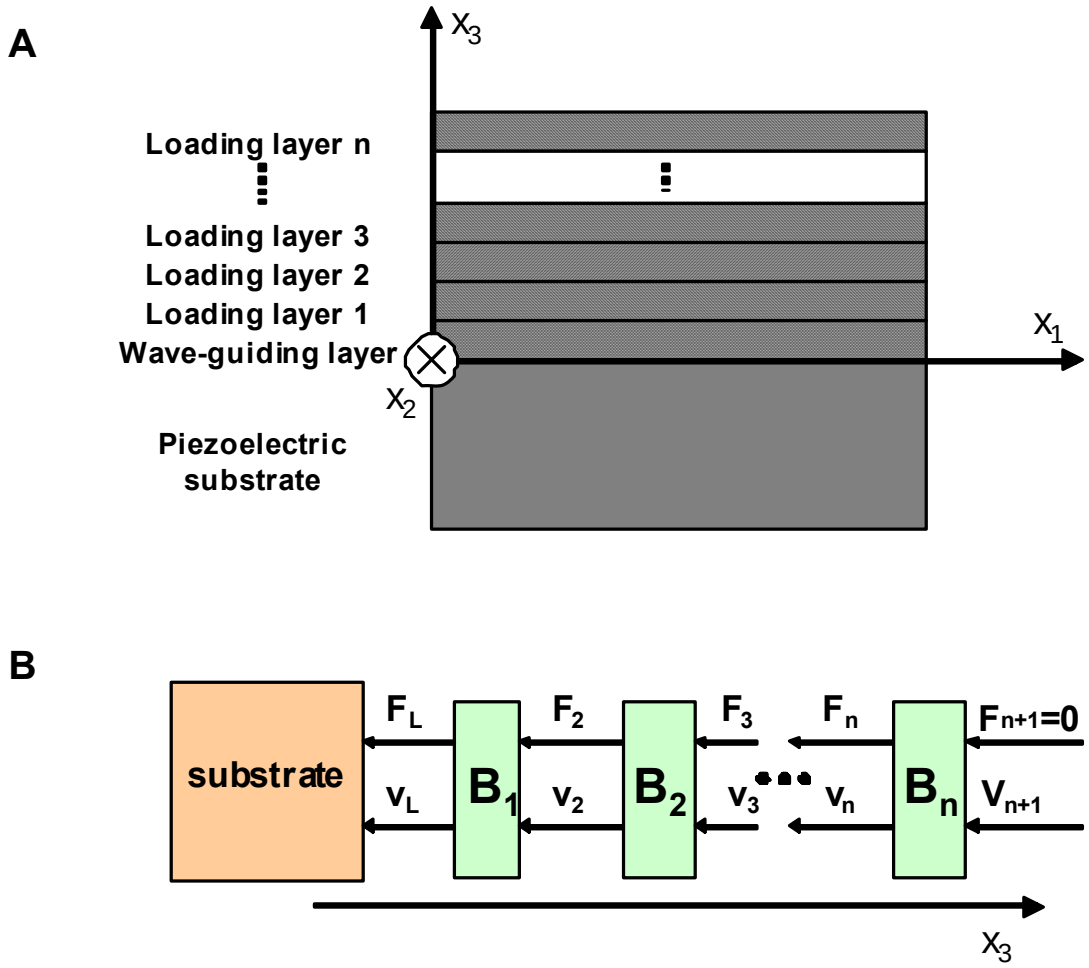

Figure 33. (A) Models for Love mode acoustic wave sensors with multilayer loadings; (B) Transfer matrix model of a Love mode acoustic wave device with multiple uniform layers loaded on one side

For Love mode acoustic wave sensors with multilayer loadings, the sensor structure includes a semi-infinite piezoelectric substrate, a finite wave-guiding layer and multiple loading layers **(Figure 33A)**. According to the transfer matrix model **(Figure 33B)**, the transfer matrix B for non-piezoelectric uniform layer is given by

$$\begin{bmatrix} F_0 \\ v_0 \end{bmatrix} = [B] \times \begin{bmatrix} F_i \\ v_i \end{bmatrix} = \begin{bmatrix} \cos\gamma & jZ\sin\gamma \\ j\sin\gamma/Z & \cos\gamma \end{bmatrix} \times \begin{bmatrix} F_i \\ v_i \end{bmatrix} \tag{5.1}$$

where F and v represent stress and particle velocity, respectively; subscript i and o represent input and output ports of the layer; Z and γ are the characteristic acoustic impedance and the phase delay of the layer [87]. Since the direction of transfer matrix model is x_3 direction, the characteristic acoustic impedance Z and phase delay are calculated in x_3 direction. In the Love mode devices, we assume that the acoustic waves are pure shear-horizontal. Therefore, the wave equation in the layers can be written as

$$U_2(x_1, x_3, t) = U_2(x_3)\exp(j(\omega t - (k_1 - j\alpha_1)x_1 - (k_3 - j\alpha_3)x_3) = U_2(x_3)\exp(j(\omega t - K\vec{r}) \tag{5.2}$$

where U is the particle displacement, ω is the angular frequency, k is wave number, α is attenuation (rate of amplitude change with the propagation distance), t is time, and subscriptions 1, 2, and 3 represent x_1, x_2 and x_3 directions respectively. The complex wave number of the acoustic wave $K = ((k_1 - j\alpha_1)^2 + (k_3 - j\alpha_3)^2)^{1/2} = \omega(\rho/G)^{1/2}$ (ρ and G are the density and complex shear modulus of the layer), and the propagation velocity of the acoustic wave in the device $v_p = \omega/k_1$. The characteristic impedance Z and phase delay in the layer γ in x_3 direction are given by

$$Z = \frac{G}{\omega} K_3 = \frac{G}{\omega}(\omega^2(\rho/G) - (k_1 - j\alpha_1)^2)^{1/2} = \sqrt{(\rho - \frac{G}{(\frac{\omega}{k_1 - j\alpha_1})^2})G} \tag{5.3}$$

$$\gamma = 2\pi h/\lambda = hK_3 = h(\omega^2(\rho/G) - (k_1 - j\alpha_1)^2)^{1/2} = \frac{\omega h}{G}\sqrt{(\rho - \frac{G}{(\frac{\omega}{k_1 - j\alpha_1})^2})G} \tag{5.4}$$

where $K_3 = k_3 - j\alpha_3$, which is complex wave number of the acoustic wave in x_3 direction, and h is the thickness of the layer. Comparing the characteristic acoustic impedance and the phase delay for the thickness shear mode resonator, which are given by $Z = \sqrt{\rho G}$ and $\gamma = \omega h\sqrt{\rho/G}$, with those for Love mode devices, we found that the expressions of Z and γ in these two modes were similar. The differences bwteen them are caused by the different propagation directions of acoustic waves: in the Love mode acoustic wave devices, the acoustic wave propagates in both x_3 and x_1 directions, while in the thickness shear mode resonators, the wave propagates only in x_3 direction. According to Eqs. (5.1), (5.3) and (5.4), the transfer matrix of the finite non-piezoelectric layer is given by

$$[B] = \begin{bmatrix} \cos\left(\frac{\omega h}{G}\sqrt{(\rho - \frac{G}{(\frac{\omega}{k_1 - j\alpha_1})^2})G}\right) & j\sqrt{(\rho - \frac{G}{(\frac{\omega}{k_1 - j\alpha_1})^2})G}\sin\left(\frac{\omega h}{G}\sqrt{(\rho - \frac{G}{(\frac{\omega}{k_1 - j\alpha_1})^2})G}\right) \\ j\sin\left(\frac{\omega h}{G}\sqrt{(\rho - \frac{G}{(\frac{\omega}{k_1 - j\alpha_1})^2})G}\right)\Big/\sqrt{(\rho - \frac{G}{(\frac{\omega}{k_1 - j\alpha_1})^2})G} & \cos\left(\frac{\omega h}{G}\sqrt{(\rho - \frac{G}{(\frac{\omega}{k_1 - j\alpha_1})^2})G}\right) \end{bmatrix} \tag{5.5}$$

With these transfer matrixes, the overall acoustic impedance of uniform multilayer loading Z_L can be easily calculated using the following equation:

$$\begin{bmatrix} F_L \\ v_L \end{bmatrix} = [B_1] \times [B_2] \times \cdots \times [B_n] \times \begin{bmatrix} F_{n+1} \\ v_{n+1} \end{bmatrix} \tag{5.6}$$

where $F_{n+1}=0$, since the top layer is exposed to air.

In chapter 3, we have developed a multiple layer model for cells adhering onto the thickness shear mode resonators. Similarly, the cell-based Love mode acoustic wave biosensors can be considered to include four uniform layers, which are the semi-infinite piezoelectric substrate, finite wave guiding layer, finite interfacial layer and semi-infinite cell layer. Therefore, according to Eq. (5.6), the overall acoustic loading impedance applied onto the piezoelectric substrate when cells adhere to the substrate is given by

$$Z_L = \sqrt{(\rho_{waveguid} - \frac{G_{waveguid}}{(\frac{\omega}{k_1 - j\alpha_1})^2})G_{waveguid}} \frac{Z_{L1} + j\sqrt{(\rho_{waveguid} - \frac{G_{waveguid}}{(\frac{\omega}{k_1 - j\alpha_1})^2})G_{waveguid}} \tan(\omega\sqrt{\frac{(\rho_{waveguid} - \frac{G_{waveguid}}{(\frac{\omega}{k_1 - j\alpha_1})^2})}{G_{waveguid}}} h_{waveguid})}{\sqrt{(\rho_{waveguid} - \frac{G_{waveguid}}{(\frac{\omega}{k_1 - j\alpha_1})^2})G_{waveguid}} + jZ_{L1}\tan(\omega\sqrt{\frac{(\rho_{waveguid} - \frac{G_{waveguid}}{(\frac{\omega}{k_1 - j\alpha_1})^2})}{G_{waveguid}}} h_{waveguid})} \tag{5.7}$$

where subscription *waveguide* represents wave guiding layer and Z_{L1} is the acoustic loading impedance on the wave guiding layer, which is calculated by

$$Z_{L1} = \sqrt{(\rho_{il} - \frac{G_{il}}{(\frac{\omega}{k_1 - j\alpha_1})^2})G_{il}} \frac{\sqrt{(\rho_{cl} - \frac{G_{cl}}{(\frac{\omega}{k_1 - j\alpha_1})^2})G_{cl}} + j\sqrt{(\rho_{il} - \frac{G_{il}}{(\frac{\omega}{k_1 - j\alpha_1})^2})G_{il}} \tan(\omega\sqrt{\frac{(\rho_{il} - \frac{G_{il}}{(\frac{\omega}{k_1 - j\alpha_1})^2})}{G_{il}}} h_{il})}{\sqrt{(\rho_{il} - \frac{G_{il}}{(\frac{\omega}{k_1 - j\alpha_1})^2})G_{il}} + j\sqrt{(\rho_{cl} - \frac{G_{cl}}{(\frac{\omega}{k_1 - j\alpha_1})^2})G_{cl}} \tan(\omega\sqrt{\frac{(\rho_{il} - \frac{G_{il}}{(\frac{\omega}{k_1 - j\alpha_1})^2})}{G_{il}}} h_{il})}$$

where subscription *il* and *cl* represent the interfacial layer and cell layer respectively. In the Love mode acoustic wave sensors, the wave equations in the semi-infinite piezoelectric substrate is given by

$$u_{2s} = u_{os}\exp((jA + B)x_3)\cdot\exp(j(\omega t - (k_1 - j\alpha_1)x_1)) \tag{5.8}$$

Although the piezoelectric substrate used here is anisotropic material, for the simplicity, in the calculation, first, we treated the substrate as an isotropic material. Therefore, the equation of motion in piezoelectric substrate can be written as

$$G_s(-A^2 + 2jAB + B^2) + (\rho_s\omega^2 - (k_1 - j\alpha_1)^2 G_s) = 0 \tag{5.9a}$$

$$\Rightarrow \begin{cases} jG_s(AB + k_1\alpha_1) = 0 \Rightarrow AB = -\alpha_1 k_1 \\ G_s(B^2 - A^2) + \rho_s\omega^2 - {k_1}^2 G_s + {\alpha_1}^2 G_s = 0 \Rightarrow B^2 - A^2 = (1 - \frac{(\omega/k_1)^2}{{v_s}^2}){k_1}^2 - {\alpha_1}^2 \end{cases} \tag{5.9b}$$

where ${v_s}^2 = \frac{C_s}{\rho_s}$. Subscription *s* represents the piezoelectric substrate and ρ is the density. From the substrate direction, the acoustic loading impedance is given by

$$Z_s\big|_{x_3=0} = \frac{T_{32}}{v_2}\bigg|_{x_3=0} = G_s \frac{\frac{\partial u_2}{\partial x_3}}{v_2}\bigg|_{x_3=0} = G_s \frac{(jA + B)}{j\omega}\bigg|_{x_3=0} \tag{5. 10}$$

which is equal to $-Z_L$. So the solution of the wavenumber k_1 and α_1 are obtained. Finally, the phase velocity and attenuation of the shear-horizontal acoustic waves in Love mode sensors can be calculated according to the values of k_1 and α_1. The transfer matrix method provides a simple way to evaluate the impact of the modification at the surface of the sensor. Indeed, we can calculate the basic properties of the structure on the devices, such as a rigid or viscoelastic layer and with or without a liquid environment.

5.3 OPTIMIZATION OF LOVE MODE ACOUSTIC WAVE SENSOR DESIGN

It has been noted that several parameters of Love mode devices, such as operating frequency, thickness and mechanical properties of wave-guiding layers, affect the sensing performance of the device [26, 31, 111]. In this section, we optimize the design of the acoustic structure and selection of materials that enhance the sensitivity according to our theoretical model developed in last section. To optimize the sensor design, first we have to investigate the effects of design parameters (material properties and thickness of wave-guiding layer, material properties of the piezoelectric substrate) on the sensor performance (sensitivity). The effect of the properties of the guiding layer and piezoelectric substrate on the acoustic wave propagation velocity was simulated using our theoretical model in the last section first. In this simulation, we assume that all the materials for wave guiding layers are acoustic lossless. From the modeling results, we found that the changes in propagation velocity with the increase in the thickness of wave guiding layer were periodic. The period decreases with the decrease in the phase velocity of the guiding layer, while increases with the decrease in the phase velocity of the piezoelectric substrate **(Figure 34A)**. However, the density of piezoelectric substrate and guiding layer don't affect the period **(Figure 34B)**. In addition, we found that a significant negative shift in the propagation velocity occurred when the phase shift φ_3 in the wave guiding layer in the thickness direction is around odd times of $\pi/2$ **(Figure 34C)**. So the period of propagation velocity change is associated with phase shift in the guiding layer. Rewriting Eq. (5.4) as $\gamma = \omega h\sqrt{\frac{1}{v_{gl}^2}-\frac{1}{v^2}}$, we get the period is given by $\pi/(\omega\sqrt{\frac{1}{v_{gl}^2}-\frac{1}{v^2}})$, which confirms that smaller v_{gl} results in a smaller period while the density of the substrate and guiding layer does nothing with it. In our simulation, the

operating frequency is calculated by $(2\pi/\lambda)*v_{substrate}$, in which λ is a constant. So the larger phase velocity causes the larger operating frequency, which confirms our simulation results too.

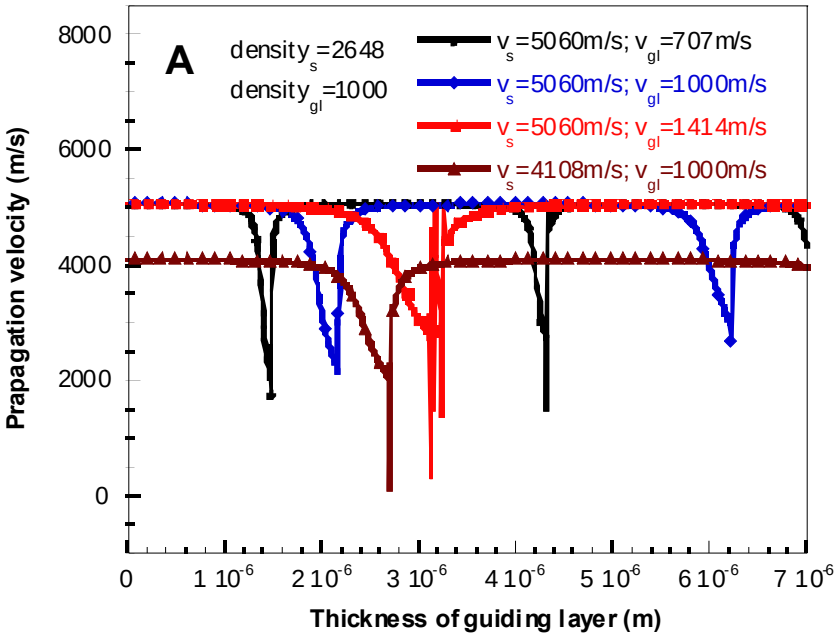

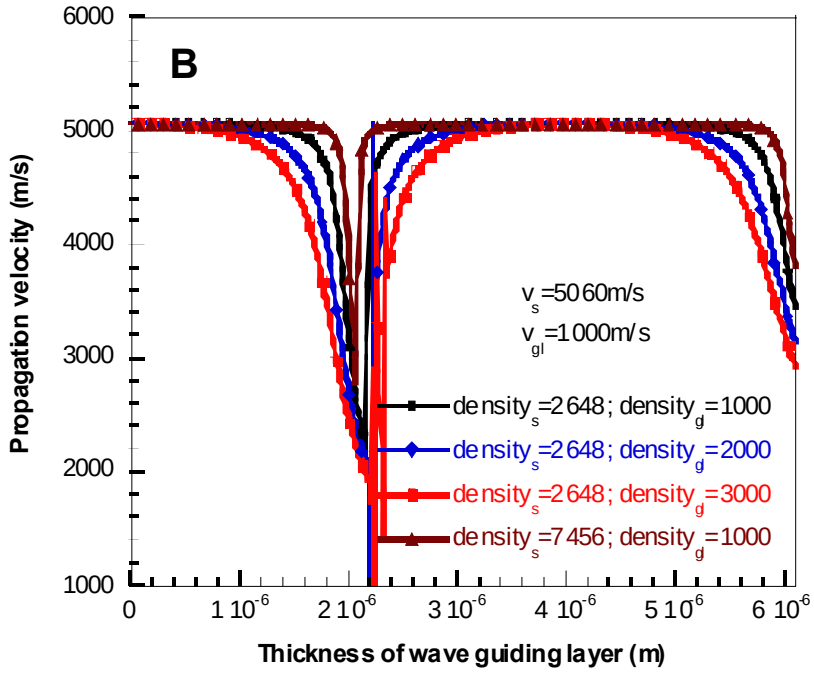

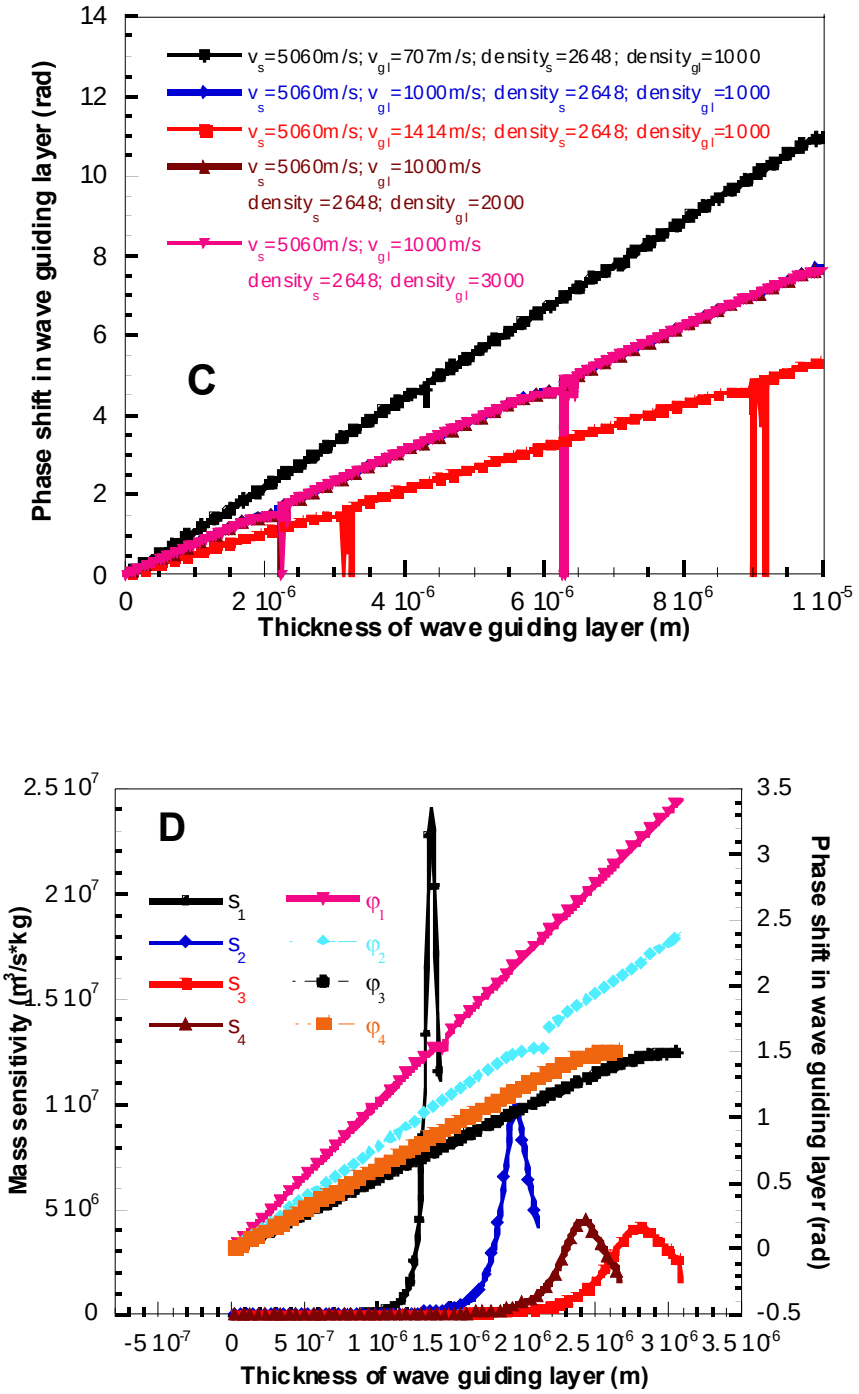

Figure 34. (A) Propagation velocity v.s. the thickness of the guiding layer; (B) Propagation velocity v.s. the thickness of the guiding layer; (C) Phase shift in wave guiding layer v.s. the thickness of wave guiding layer; (D) mass sensitivity and phase shift in guiding layer v.s. the thickness of guiding layer. The materials parameters of substrate and guiding layer for each curve are (v_s=5060m/s, v_{gl}=707m/s, $density_s$=2648kg/m^3, $density_{gl}$=1000kg/m^3 for s_1 and φ_1; v_s=5060m/s, v_{gl}=1000m/s, $density_s$=2648kg/m^3, $density_{gl}$=1000kg/m^3 for s_2 and φ_2; v_s=5060m/s, v_{gl}=1414m/s, $density_s$=2648kg/m^3, $density_{gl}$=1000kg/m^3 for s_3 and φ_3; v_s=4108m/s, v_{gl}=1000m/s, $density_s$=2648kg/m^3, $density_{gl}$=1000kg/m^3 for s_4 and φ_4)

For the mass sensitivity, we have found that it reaches a maximum value when the phase shift in the guiding layer is around $\pi/2$ for each device. The maximum mass sensitivity is larger for the devices with larger $v_{substrate}$ and smaller v_{gl} **(Figure 34D)**. The value of $\pi/2$ for the phase shift in the guiding layer indicates that the film resonance happens at that time and the shear stresses applied to the lower film surface interfere constructively with those reflected from the upper film surface. At that condition, the maximum coupling of acoustic energy from the piezoelectric substrate to the wave guiding layer is obtained, which causes the highest sensitivity. In addition, the larger $v_{substrate}$ and smaller v_{gl} results in the deposition of a thinner guiding layer to obtain the film resonance, which means in the devices with the larger $v_{substrate}$ and smaller v_{gl}, the acoustic energy is trapped in a thinner layer. This results in the increase in the device sensitivity.

Considering the guiding layer is acoustic loss, we checked the effect of the guiding layer viscosity on the propagation velocity, attenuation and their sensitivity to mass loading. The guiding layer with acoustic loss not only induces changes in phase velocity, but also attenuation in acoustic waves. With increasing the viscosity of guiding layer, the changes in the propagation velocity and attenuation are significantly damped, especially when the guiding layers are at the resonance in the thickness mode. In addition, compared with the fundamental resonant response, the harmonic resonant responses for both propagation velocity and attenuation become less pronounced **(Figure 35A and 35B)**. It has been explained that particle motion at the upper surface of the film goes from an in-phase to an out-of-phase condition when the phase shift is beyond $\pi/2$, which results in a smaller particle excursion in the upper regions of the film, diminishing the kinetic contribution to velocity and attenuation response [20]. **Figure 35C** shows the response of propagation velocity and attenuation sensitivity to mass loading with changing

the viscosity and the thickness of guiding layer. We found that with increasing the viscosity of guiding layer, the maximum values of the propagation velocity and attenuation sensitivity to mass loading (for different thickness of guiding layer) increased first and then decreased when the viscosity of guiding layer is around 80cp and 160cp respectively. In addition, we found the sensitivity was affected by the original acoustic loading on the device. In this simulation, we calculated the sensitivity by computing the velocity and attenuation changes induced by the gold layer with 1nm in thickness when 0.1nm, 1nm, and 10nm gold layer already deposited onto the devices. We found the original acoustic loading also affects the sensitivity, especially for the thickness of guiding layer on which the sensitivity has the maximum value.

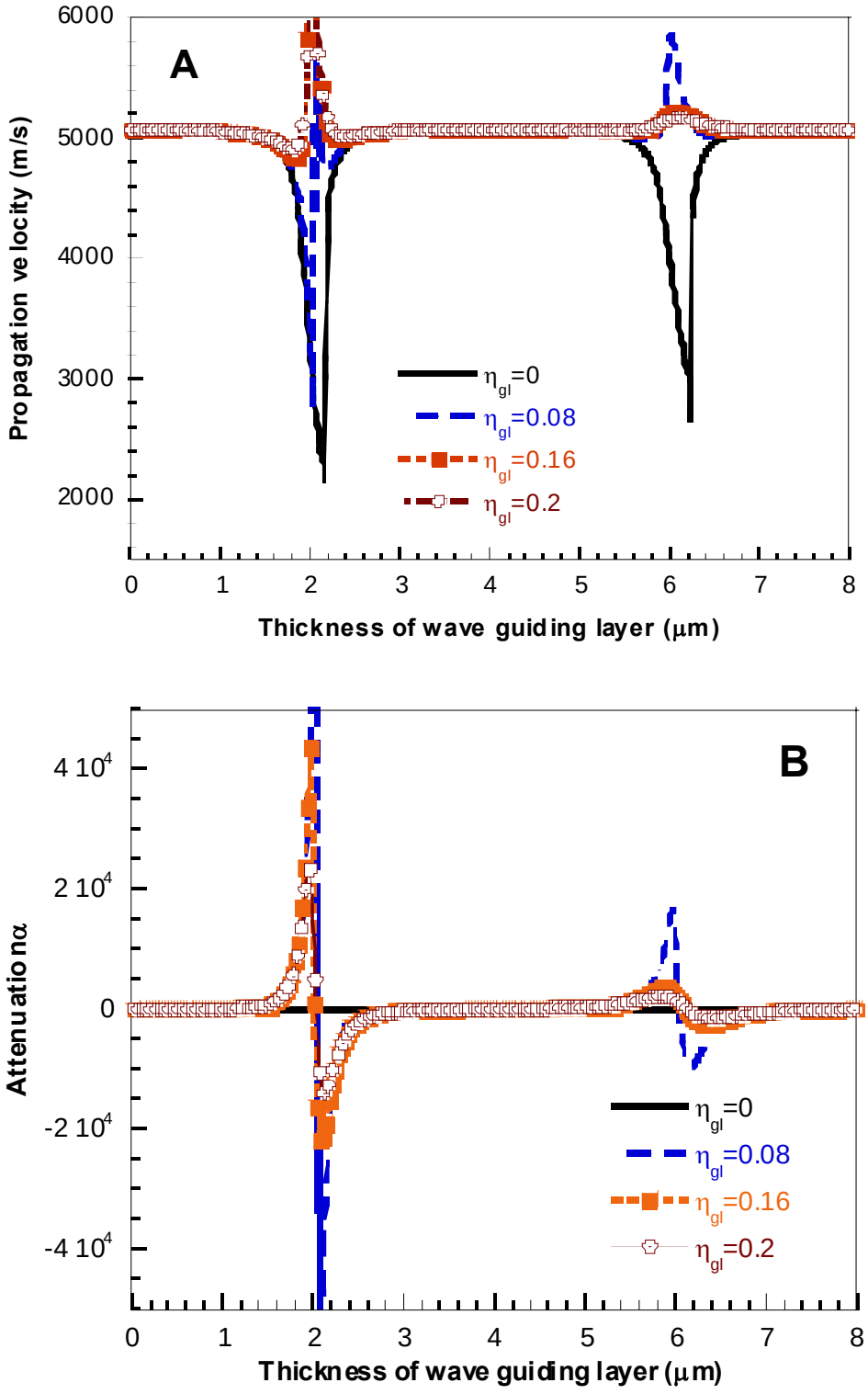
A
Propagation velocity (m/s)
6000
5000
4000
3000
2000
0
1
2
3
4
5
6
7
8
Thickness of wave guiding layer (μm)
ηgl=0
ηgl=0.08
ηgl=0.16
ηgl=0.2
B
Attenuation α
4 10^4
2 10^4
0
-2 10^4
-4 10^4
0
1
2
3
4
5
6
7
8
Thickness of wave guiding layer (μm)
ηgl=0
ηgl=0.08
ηgl=0.16
ηgl=0.2

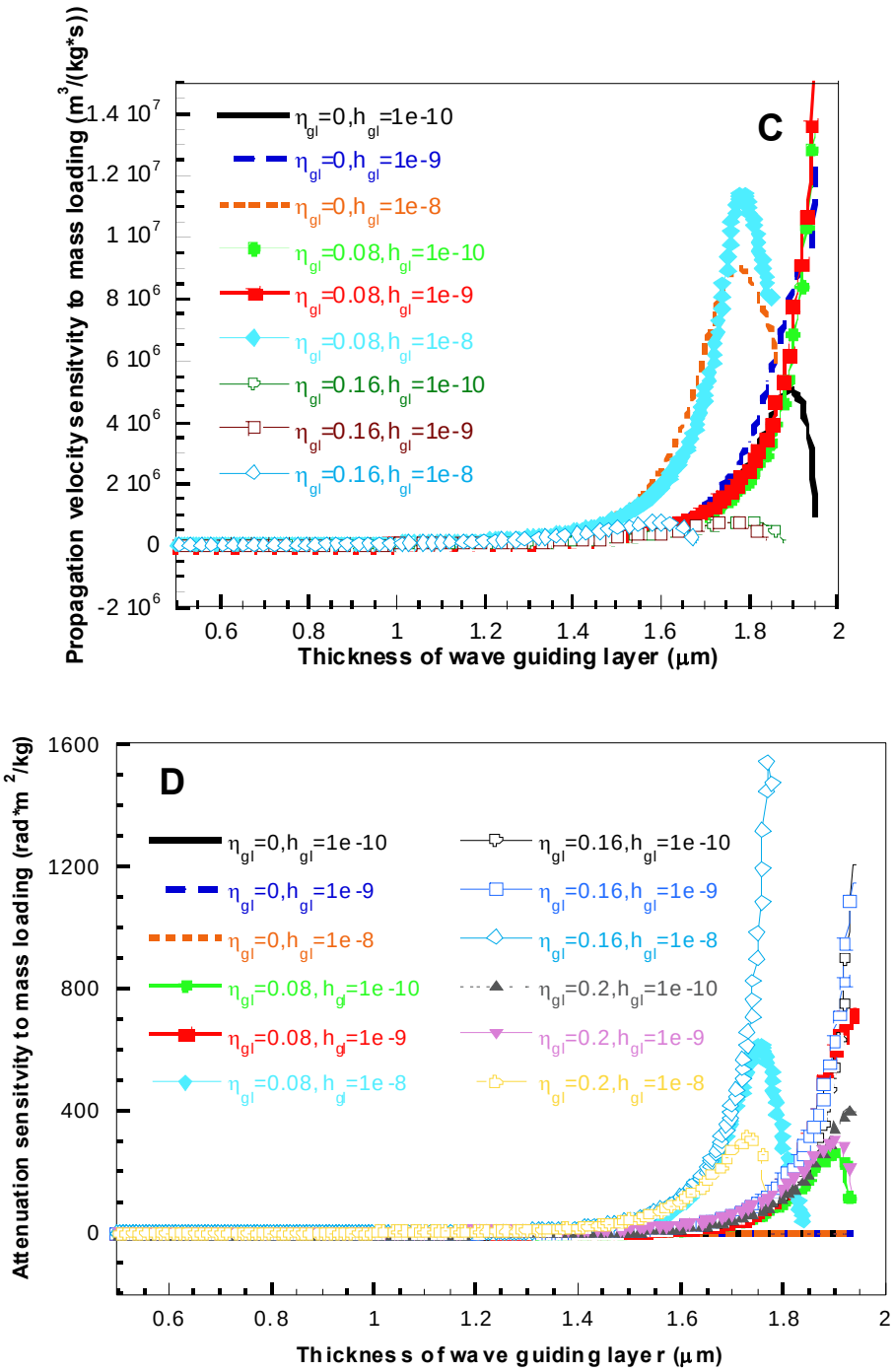

Figure 35. (A) Propagation velocity v.s. thickness of wave guiding layer; (B) Wave attenuation v.s. thickness of wave guiding layer; (C) Propagation velocity sensitivity to mass loading v.s. thickness of wave guiding layer; (D) Attenuation sensitivity to mass loading v.s. thickness of wave guiding layer

Table 7 Parameters of the materials for the simulation of Love mode devices

Material	Density (kg/m^3)	Phase velocity (m/s)	Shear stiffness (GPa)	Viscosity (cp)
Quartz	2648	5060	66.3	0
36^o rotated YX $LiTaO_3$	7456.4	4108	130.3	0
PMMA	1100	1100	1.3	14.14
SiO_2	2610	2850	8.3	0
SU-8	1200	814	0.796	$1.414*10^{-2}$

Based on our simulation results, we conclude that in order to obtain a high sensitivity for the Love mode device, the wave guiding layer and piezoelectric substrates should meet several requirements: high phase velocity for the piezoelectric substrate and low phase velocity and relative low viscosity (less than 80-100cp) for the wave-guiding layer. In addition, we should control the thickness of guiding layer to make the phase shift in the layer around $\pi/2$. Table 7 lists the parameters of the materials usually considered as the substrate and wave guiding layer for Love mode devices. ST-cut quartz and 36^o rotated YX $LiTaO_3$ are usually used as the substrate, and PMMA, SiO_2 and SU-8 as the guiding layers. The phase velocity of 36^o rotated YX $LiTaO_3$ is a little lower than that ST-cut quartz. However, since 36^o rotated YX $LiTaO_3$ has a relatively higher electromechanical coupling coefficient than quartz, which makes the better performance of the device. So both quartz and YX $LiTaO_3$ can be considered as the piezoelectric substrate. For the wave guiding layer, PMMA and SU-8 have the similar properties, lower phase velocity but higher viscosity compared with SiO_2. Since the viscosity for PMMA and SU-8 is

much less than 80cp, which does not induce a significant decrease in the sensitivity according to our simulation results, we will choose PMMA as the wave-guiding layer in our experimental studies.

5.4 EXPERIMENTAL CHARACTERIZATION OF LOVE MODE ACOUSTIC WAVE SENSORS

5.4.1 Fabrication of Love mode acoustic wave devices

The piezoelectric substrate used for the Love mode acoustic wave device is a 36^{o}-rotated Y-cut X-propagation Lithium Tantalate (36^{o}YX-$LiYaO_3$). The interdigital transducers (IDTs) were fabricated using the photolithography and lift-off procedures. Basically, photoresists were patterned on the Lithium Tantalate using standard photolithography techniques. The 10/80nm thick Cr/Au layer was deposited onto the photoresist-patterned substrate, covering the whole surface. During the lifting-off, the photoresist under the metal film is removed with solvent, taking the film with it, and leaving only the film which was deposited directly on the substrate. After finishing patterning IDTs on the substrate, the wafer is diced into several devices. Each device has a dual delay line configuration, of which one is the reference line and the other is sensing line. This dual line is used to reduce all the secondary environmental effects such as temperature variation, pressure interaction, etc **(Figure 36)**. To reduce the reflection of acoustic waves from the crystal ends and bulk wave component that can affect the sensitivity and reproducibility of the device, the two short ends of the substrate, which are perpendicular to the direction of wave propagation, were coated with PDMS as a absorber. The PDMS can absorb the

waves to avoid the reflection of the acoustic wave from the two short ends of the substrate. The bottom side of the device is roughed to dissipate bulk acoustic wave that are generated by the transducers. For each IDTs, there are thirty split finger pairs IDTs having periodicity of 32μm. Therefore, the operating frequency is around 131MHz. The IDT center-to-center separation is about 8.8 mm and the thickness of the substrate is about 0.5mm.

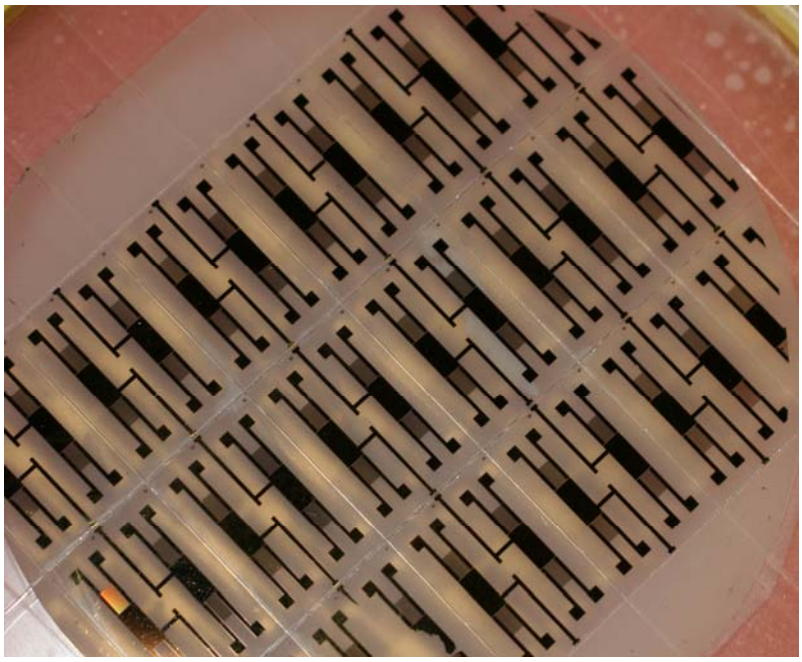

Figure 36. Fabricated shear-horizontal acoustic wave devices

PMMA was used as the wave-guide layer to trap the acoustic energy near the sensing surface in our experiments. According to the thickness range of the PMMA film desired, PMMA solution with appropriate molecular weight and concentration was chosen. Basically, PMMA was coated onto the devices by spin coating. To characterize our device, we coated the PMMA film with the thickness of 1.4-3.3 μm by spin coating with appropriate spin speed and time. The device with PMMA coating was then cured at 180^{o}C for 2 hours in ovens. After curing, the

coated devices were allowed to cool down to room temperature. The thickness of PMMA films was measured using the surface profilometer then. After the PMMA film coated on the device surface, platinum wires were bounded to the electrode pads using conductive silver paste (SPI Supplies and Structure Probe, Inc., West Chester, PA). Then the devices were baked at 120^{o}C on the hot plate for several minutes. The uncured PDMS were poured at the two short ends of the devices. At high temperature, PDMS was quickly cured and severs as absorbers. Finally, the Love mode acoustic wave devices were obtained **(Figure 37)**.

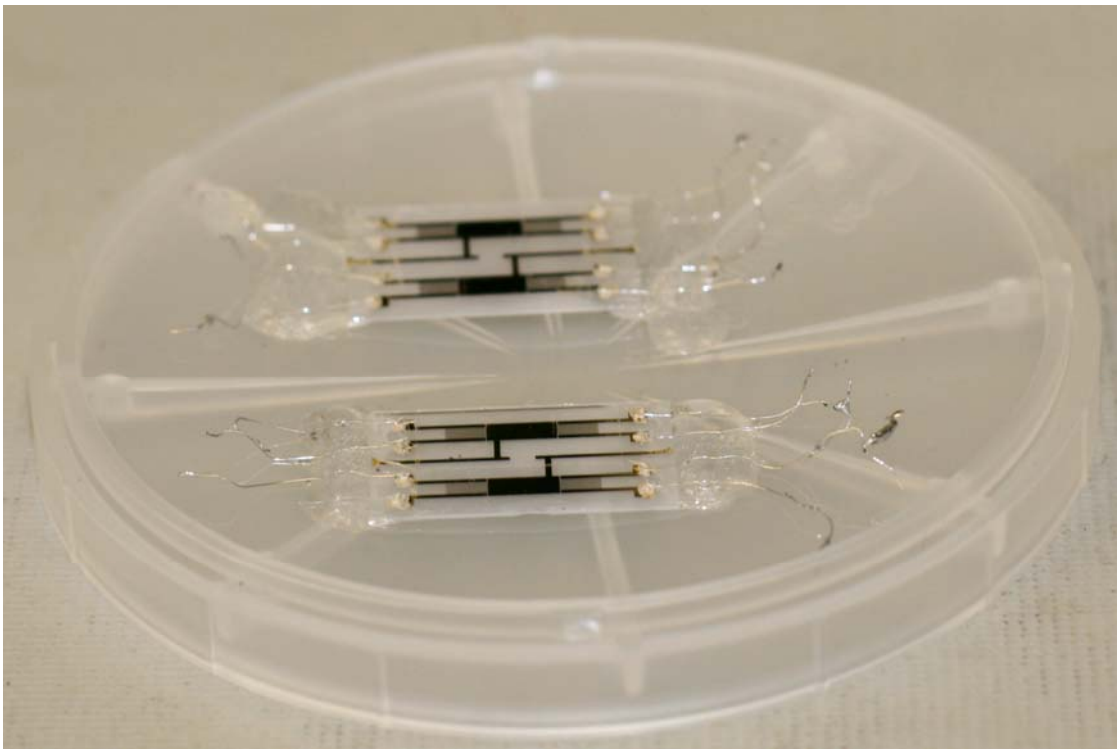

Figure 37. Love mode acoustic wave devices

5.4.2 Experimental setup

During the measurement, the acoustic wave sensors were mounted onto the fixtures by tapes **(Figure 38)**.

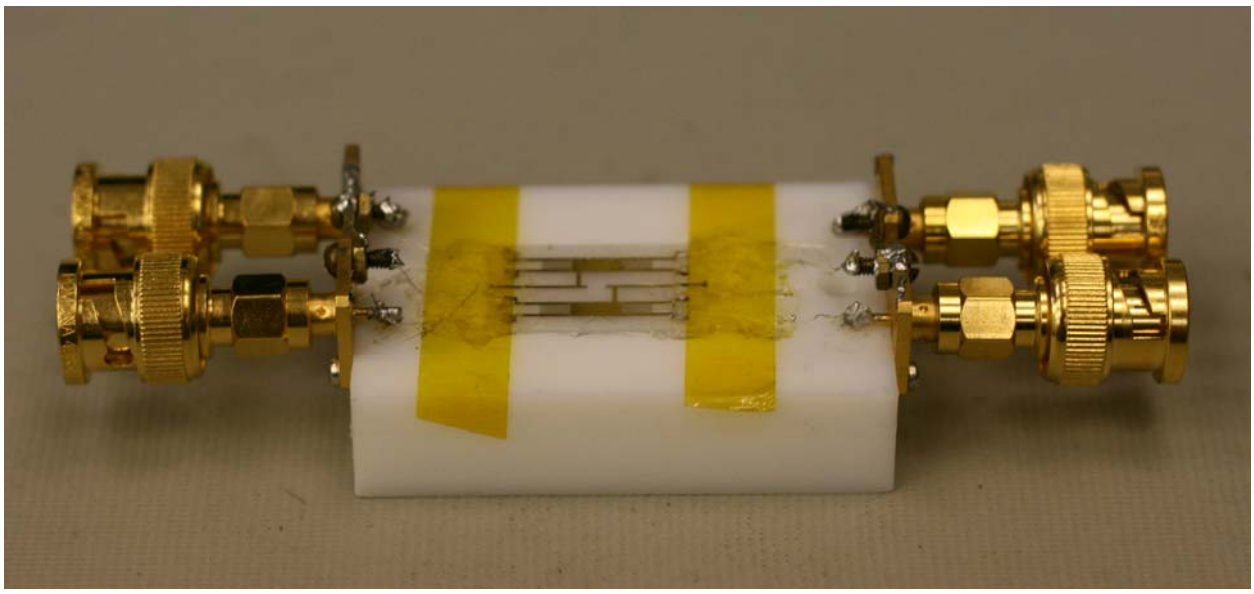

Figure 38. Love mode acoustic wave devices mounted on the test fixture

The wires glued to IDT electrodes were linked to BNC connectors in the test fixture, which were connected to the measurement system. The measurement system is comprised of a vector network analyzer (HP8722C), a switch/control unit (Agilent 34970A), hi-speed GPIB controller and the labview software **(Figure 39)**.

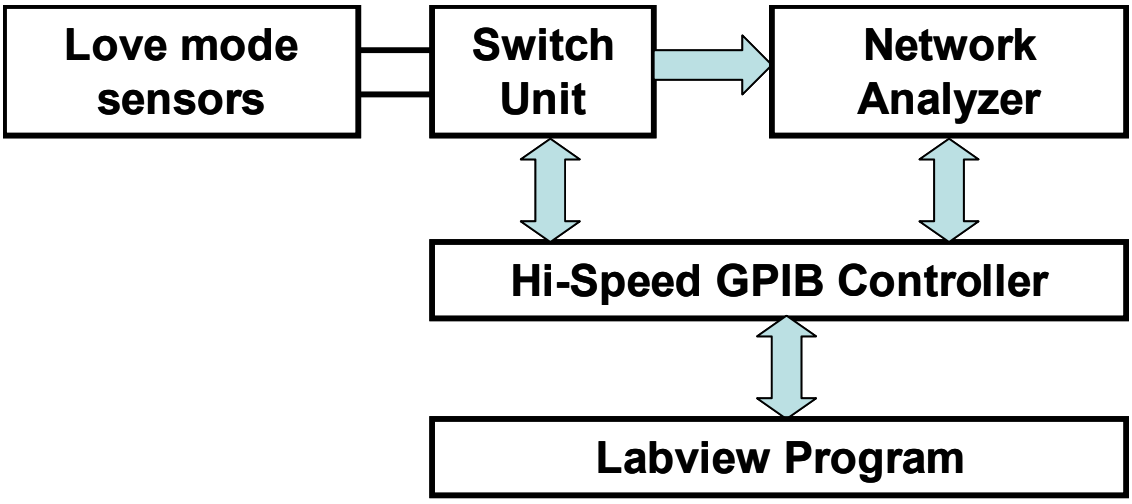

Figure 39. Measurement system of Love mode acoustic wave sensors.

5.4.3 Experimental results

First, the devices without PMMA coatings were mounted onto the test fixture. The amplitude and phase of parameter S_{21} between two IDTs were measured using the network analyzer. It was found that the resonant frequency of all the devices was around 130MHz and the insertion loss at the resonant frequency was about 29dB. The relative high insertion loss is because IDTs on the 36^{o} rotated $LiTaO_3$ substrate produces the surface skimming bulk wave, in which the acoustic waves are propagating deeper into the bulk material therefore the insertion loss increases. After the measurement of the devices without PMMA coating, PMMA were spun on the device surface with different spinning speed and time in order to obtain the different film thickness in the range of 1,2-3.5μm. **Table 8** shows the experimental conditions and thickness of the PMMA film under each condition.

Table 8 Experimental conditions of PMMA spin coating and the thickness of PMMA film

Material	spinning speed (rpm)	spinning time (s)	Film thickness (μm)
PMMA 950 C7	4000	30	1.0
PMMA 950 C7	2500	30	1.4
PMMA 950 C9	4000	30	2.0
PMMA 950 C7	1500	30	2.2
PMMA 950 C9	3500	30	2.4
PMMA 950 C9	3000	30	2.7
PMMA 950 C9	2500	30	2.9
PMMA 950 C9	2000	30	3.3
PMMA 950 C9	1500	30	3.5

The S_{21} between two IDTs on the devices with PMMA coatings with different thickness was measured then. The amplitude and phase images of the device with 2.0μm thick PMMA coating showed that the resonant frequency decreases a lot, which is about 6MHz, compared with uncoated device while the insertion loss decreased since the PMMA layer traps the acoustic energy in the guiding layer **(Figure 40)**.

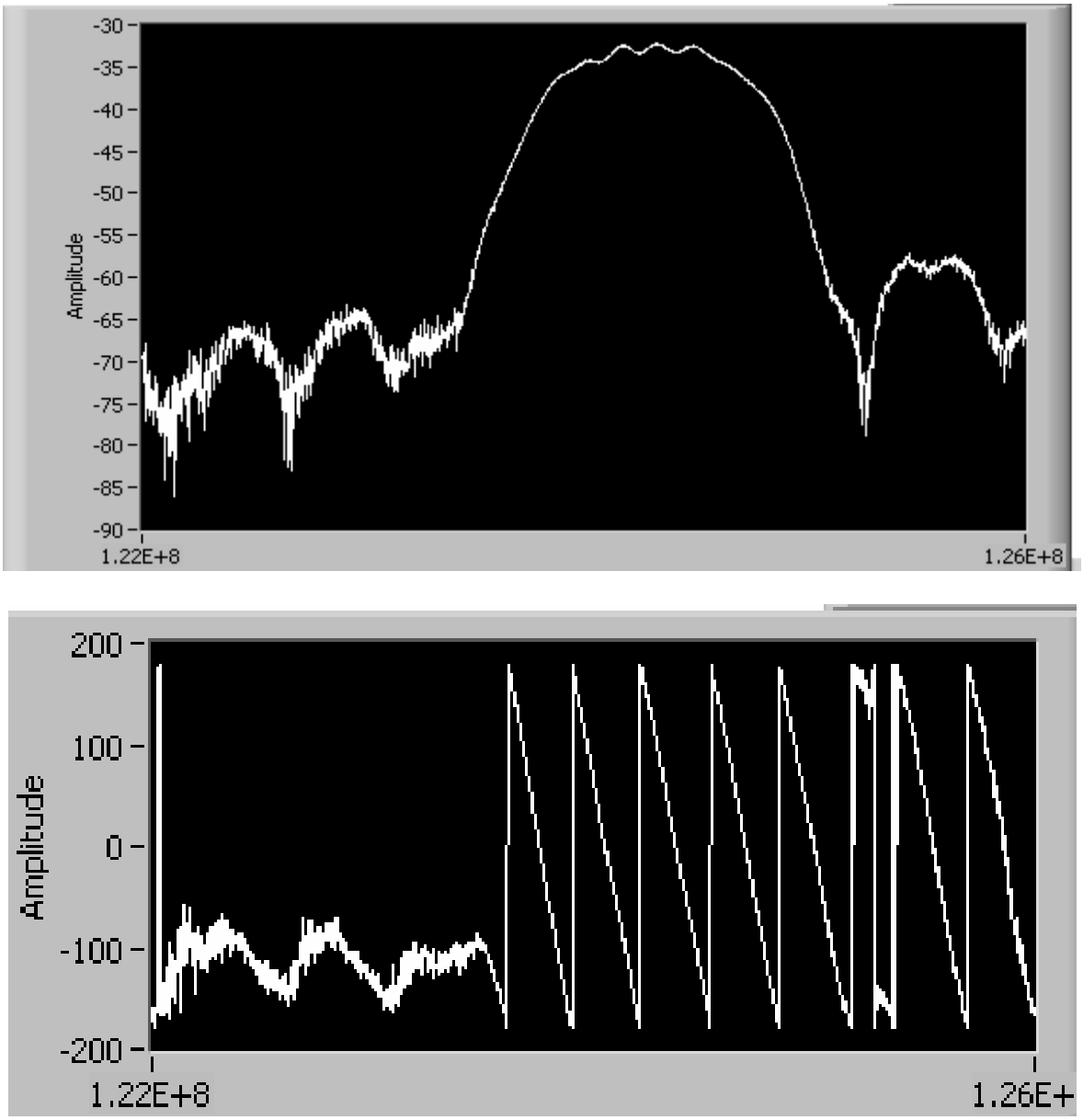

Figure 40. The amplitude and phase images of S_{21} for Love mode acoustic sensors with 2.0mm PMMA coating.

With the increase in the thickness of the PMMA film, the resonant frequency decreases a little bit first and decreases dramatically when the thickness of PMMA film is around 2.0μm. When the thickness of PMMA layer is larger than 2.5μm, the resonant frequency returns to 130 MHz again. Comparing our experimental results with our theoretical modeling ones, we found that the trend of resonant frequency change with increasing the thickness of PMMA coating layer

was consistent. However, the maximum frequency shift obtained by our experimental results is much smaller than that predicted by the theoretical models **(Figure 41)**. The reason is that according to our theoretical models, the significant decrease in the resonant frequency occurs when the thickness of PMMA coating layer is in the range of 2.1-2.3μm, which is a very narrow range. In our experiment, we used spinning coating method to deposit PMMA layer on the sensor surface, which is very hard to control the thickness of the coating layer precisely. Therefore, it is hard to obtain the PMMA film with a certain thickness that causes a large decrease in the resonant frequency of the Love mode acoustic wave sensors.

The initial insertion loss for the device without PMMA coating is about -29dB. Compared with bared device, the insertion loss change induced by the PMMA coating layer initially increases with increasing the PMMA guiding layer thickness, reaching a minimum value at about 1.4μm. Then the increase in the thickness of the PMMA layer gives a gradual decrease in insertion loss **(Figure 42)**. Comparing the experimental results with our theoretical modeling results, we found that the increase in the insertion loss could not be predicted by our theoretical models. In addition, our theoretical model showed that the insertion loss for the device without coating was zero while our experimental results showed 29dB attenuation from the input IDT to output IDT. Although our theoretical model cannot predict the initial signal attenuation for the bared device and the increase in the insertion loss when the thickness of PMMA guiding layer is thin, the gradual decrease after the insertion loss reaches a maximum value observed in our experimental results, which is consistent with our theoretical modeling results. The decrease in the insertion loss with increasing the thickness of PMMA guiding layer is believed to be determined by the viscosity of PMMA wave guiding layer.

The reason that causes the inconsistence between our theoretical and experimental results is that in our theoretical modeling, we assume all the acoustic energy is located near the surface of shear-horizontal acoustic wave device and the output IDT can transduce all the acoustic energy in the device into electrical signals. Therefore, the insertion loss in our theoretical model is assumed to be the attenuation in the acoustic waves when they propagate in x_1 direction. So in our calculation, we use parameter α_i to compute the attenuation between two IDTs. However, for the real device, as we discussed in chapter 1, there is no pure shear-horizontal surface acoustic wave device. The IDTs on the 36^o rotated $LiTaO_3$ substrate produces the surface skimming bulk wave, in which the acoustic waves are propagating deeper into the bulk material. Therefore, the output IDT cannot transform all the acoustic energy into the electrical signals and the additional signal attenuation between two IDTs is produced. Therefore, in real experimental measurements, the insertion loss is the sum of the loss induced by material viscosity when the acoustic wave propagates in it in x_1 direction, the energy loss due to the acoustic wave propagates into the bulk material, and the loss induced by measurement system. In our theoretical modeling, we only considered the loss induced by the loss of wave-guiding materials, which causes the inconsistent between our theoretical modeling results and experimental results.

Overall, our experimental results demonstrated that our theoretical model could efficiently predict the resonant frequency shift in the Love mode acoustic wave device with loadings. For the insertion loss, although our models cannot describe the signal attenuation induced by the changes in acoustic energy distribution because of the wave guiding layer deposition, they are able to predict the insertion loss induced by the material loss in loading layers. For the biological applications of Love mode acoustic wave devices, appropriate wave guiding layers have been chosen and deposited on the device surface. Therefore, most of energy

has been trapped near the device surface. With cells attaching to the surfaceof this device, most of the acoustic energy is still confined in or near the guiding layers. Therefore, the insertion loss due to cells is mainly induced by the material loss of the cell, protein or medium layers. So our theoretical models are valid for describing the resonant frequency and insertion loss change for Love mode acoustic wave devices as cell-based biosensors.

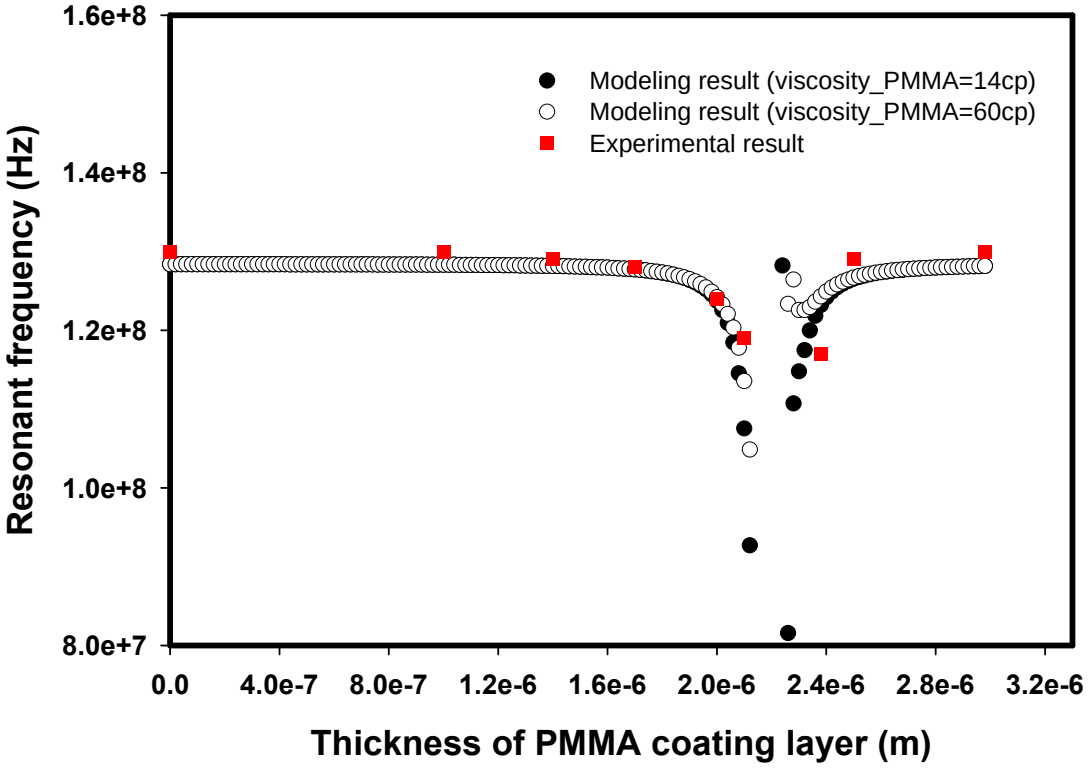

Figure 41. Comparison of theoretical and experimental results of resonant frequency shift with the thickness of PMMA coating layer.

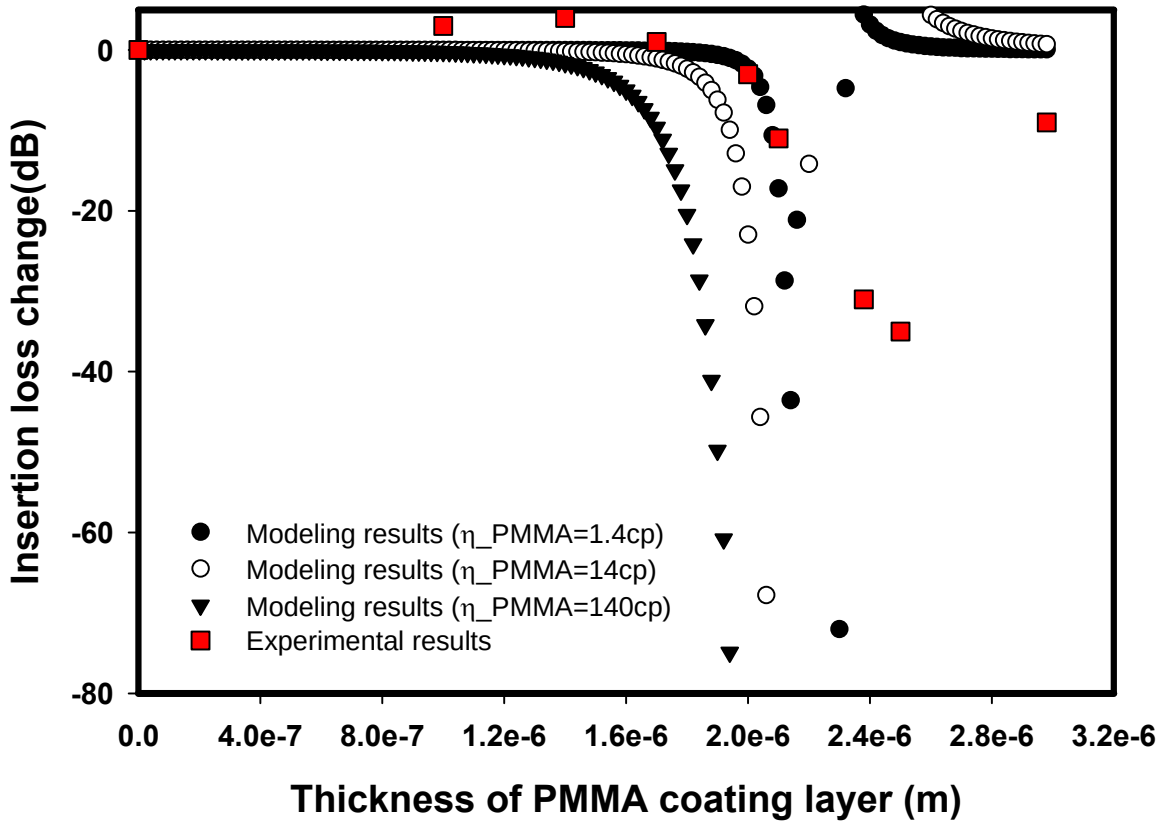

Figure 42. Comparison of theoretical and experimental results of insertion loss changes induced by PMMA layer with the different thickness.

5.5 POTENTIAL APPLICATIONS OF LOVE MODE ACOUSTIC WAVE SENSOR FOR CELL BIOLOGICAL STUDIES

In the above sections, we have discussed the theoretical modeling, the optimization, and the experimental characterization of the Love mode acoustic wave sensors. Our experimental results showed the ability of our theoretical model to help optimize the sensor design and its validity. In this section, through investigating the relationship between the electrical signals of the device

(resonant frequency and attenuation) and cell-substrate interaction and cell viscoelastic properties, we discuss the potential applications of Love mode acoustic wave sensors for cell biological studies.

The effect of the thickness of the interfacial layer and wave guiding layer on the relative changes in the propagation velocity and attenuation to the semi-infinite cell medium loading was investigated **(Figure 43)**. In this simulation, we choose 36^{o} rotated $LiTaO_3$ as substrate and PMMA as wave guiding layer. According to our previous study, the storage shear modulus and viscosity of cell layer are chosen to be 50KPa and 1cp respectively. The viscosity of interfacial layer is assumed to be 2cp [73, 75, 104, 105]. The relative change in phase velocity and attenuation to the semi-infinite cell medium loading is caused by the cell layer. From the results, we can see that when the thickness of the interfacial layer is beyond about 150nm, the relative change in phase velocity and attenuation to the semi-infinite cell medium loading almost reaches to zero. These results indicate that the penetration depth of the acoustic wave with the frequency of 131MHz (the operating frequency in our simulation) in the medium with the viscosity of 2cp is about 150nm. In another word, if the cell layer is too far from the substrate, for the Love mode acoustic wave devices with the operating frequency above 100MHz, the acoustic waves are totally damped before they reach the cell layers. Therefore, for Love mode acoustic wave devices with operating frequency above 100MHz, cells can be detected only when cells tightly attach to the substrate. If the cells are far from the substrate, the acoustic waves only penetrate into the interfacial layer, therefore, the devices has the potential to detect the properties of interfacial layer, which may be altered by the proteins in this layer and focal adhesion area between the substrate and cell layer. Therefore, the Love mode acoustic devices have the potential to detect the protein production by cells and monitor cell adhesion to the substrate.

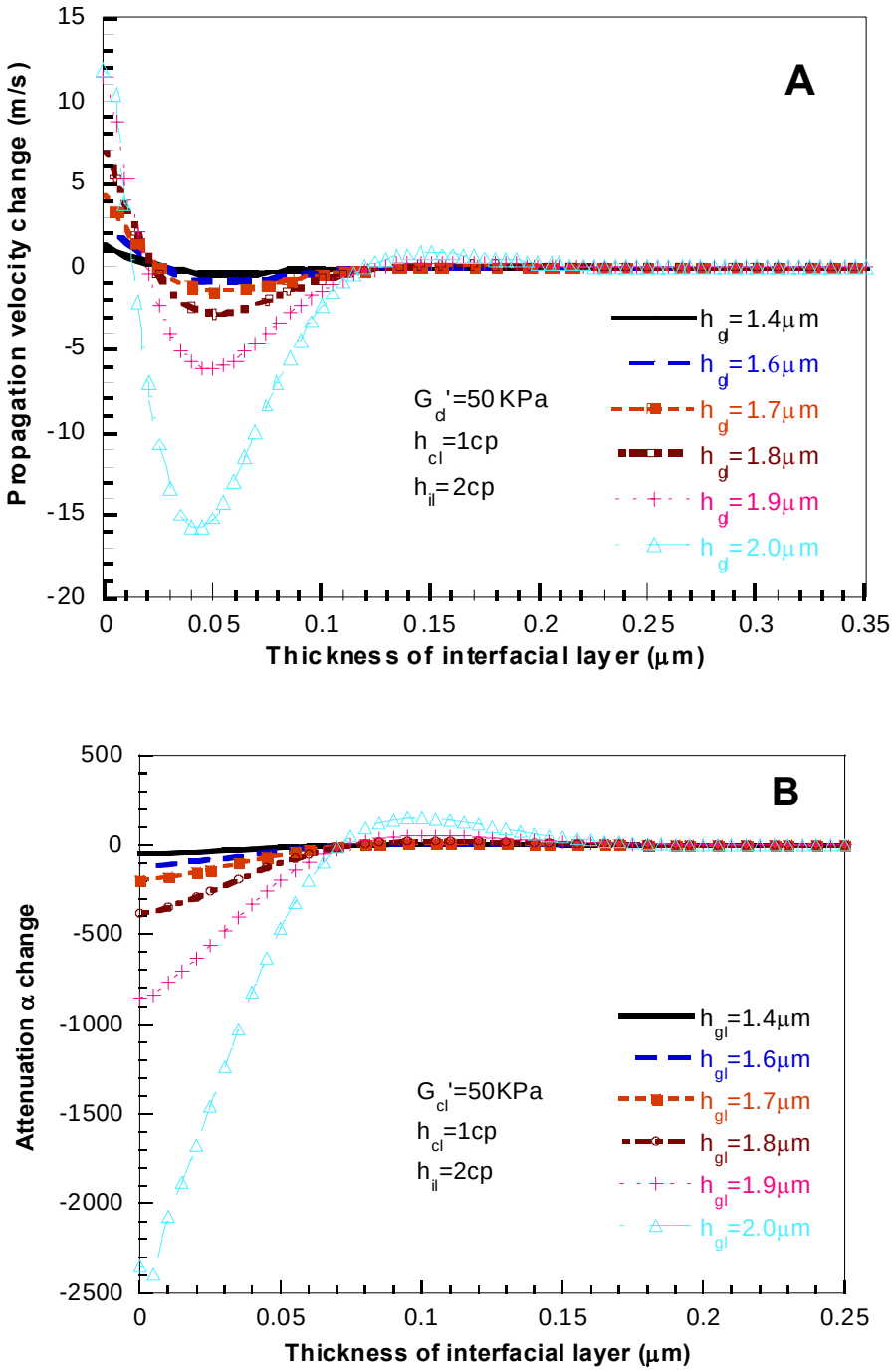

Figure 43. Effect of the thickness of interfacial layer and wave guiding layer on the relative changes in (A) the propagation velocity and (B) attenuation to the semi-infinite cell medium loading.

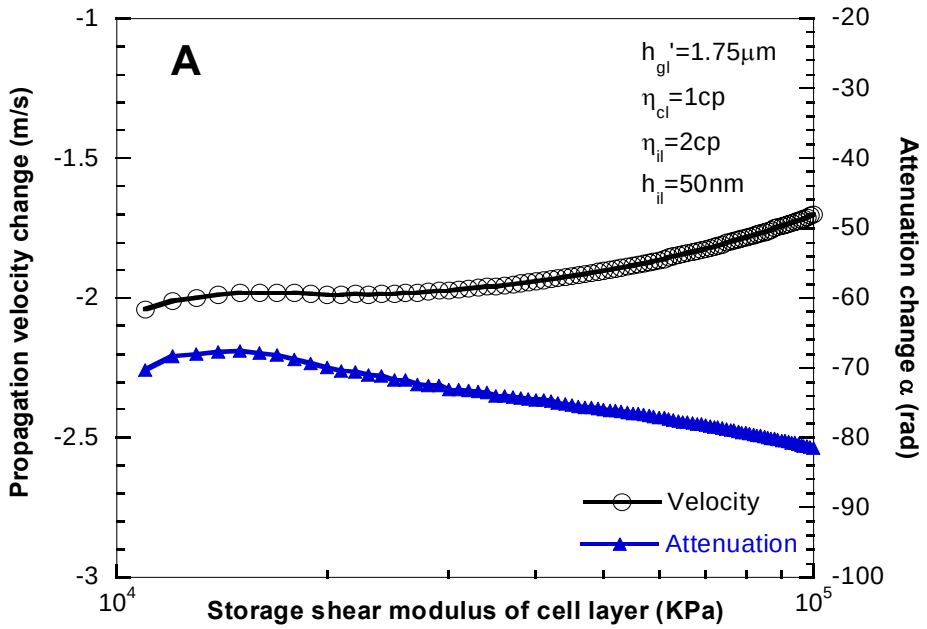
A
h_{gl}'=1.75μm
η_{cl}=1cp
η_{il}=2cp
h_{il}=50nm
Velocity
Attenuation
Propagation velocity change (m/s)
Attenuation change α (rad)
Storage shear modulus of cell layer (KPa)
-1
-1.5
-2
-2.5
-3
-20
-30
-40
-50
-60
-70
-80
-90
-100
10^4
10^5

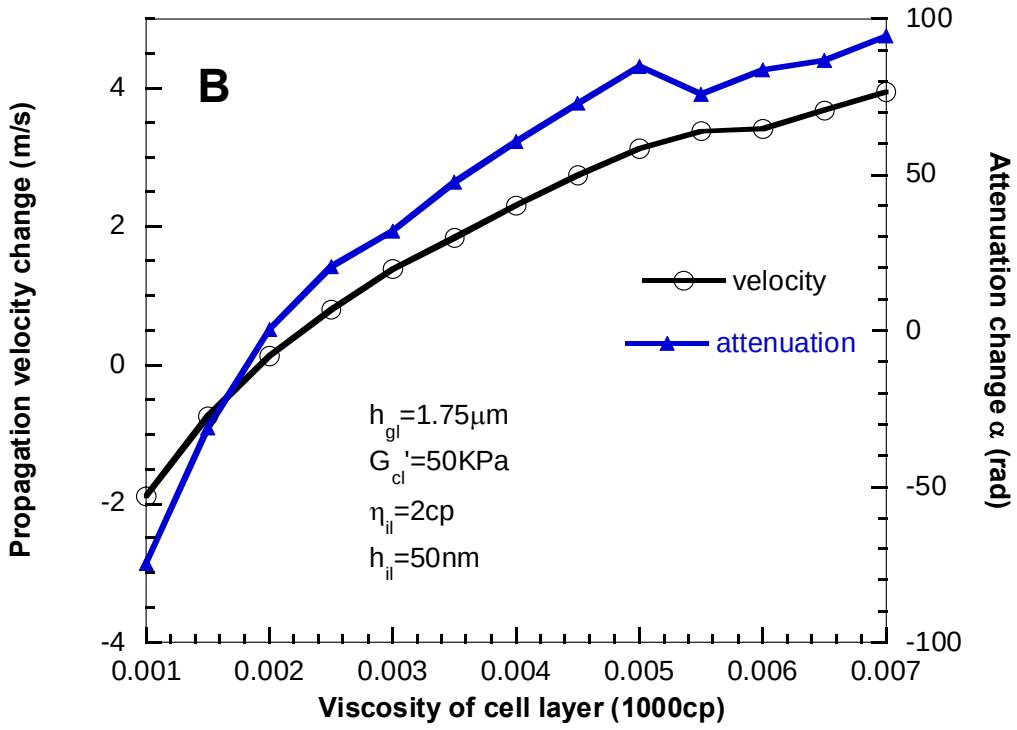
B
velocity
attenuation
h_{gl}=1.75μm
G_{cl}'=50KPa
η_{il}=2cp
h_{il}=50nm
Propagation velocity change (m/s)
Attenuation change α (rad)
Viscosity of cell layer (1000cp)
4
2
0
-2
-4
100
50
0
-50
-100
0.001
0.002
0.003
0.004
0.005
0.006
0.007

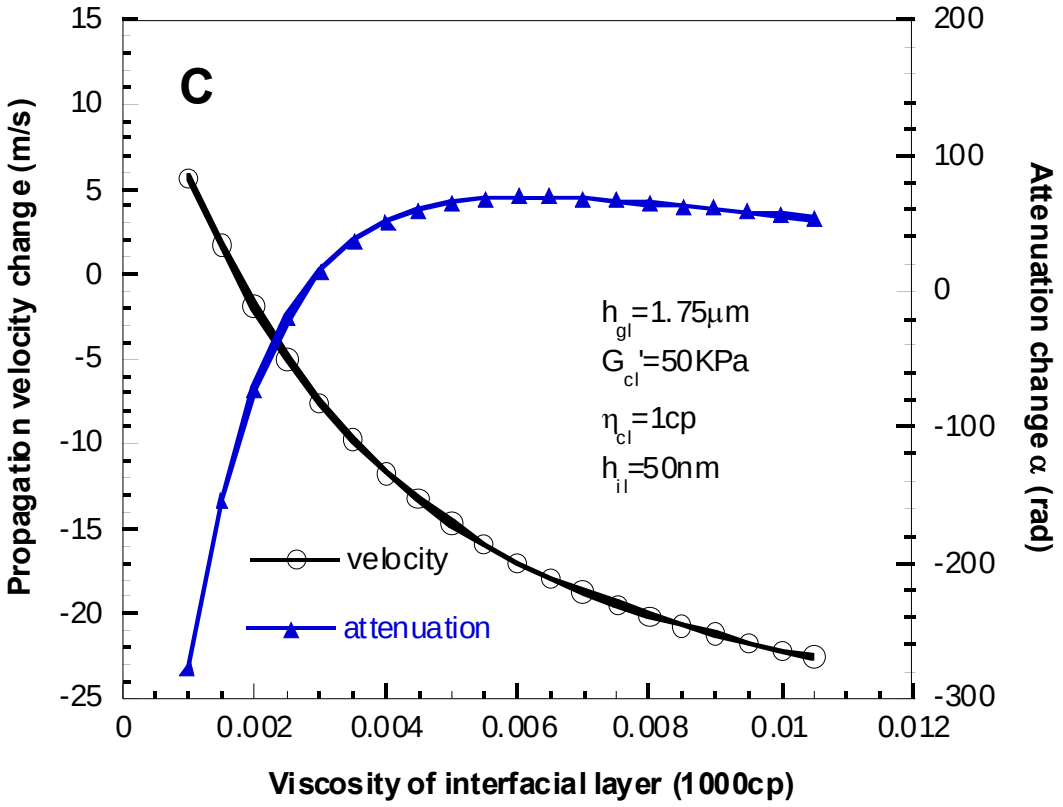

Figure 44 Effects of (A) storage shear modulus of cell layer, (B) viscosity of cell layer and (C) viscosity of interfacial layer on the relative changes in the propagation velocity and attenuation to the semi-infinite cell medium loading.

The effect of the storage shear modulus of cell layer on the propagation velocity and attenuation of Love waves was investigated using our theoretical model **(Figure 44A)**. From the results, we can see that the propagation velocity and attenuation of Love waves are not sensitive to storage shear modulus of cell layer with the range of 30-100KPa. With the increase of cell viscosity, changes in propagation velocity and attenuation increase **(Figure 44B)**. The sensitivity of propagation velocity and attenuation to cell viscosity is higher than to the storage shear modulus of cell layer. **Figure 44C** shows the propagation velocity and attenuation response to the changes in the viscosity of the interfacial layer. We found that the device signals were much

sensitive to the properties of interfacial layer compared with the properties of cell layer. This is reasonable since the interfacial layer is more close to the substrate; therefore, the acoustic wave is stronger in the interfacial layer than in the cell layer.

5.6 SUMMARY

In summary, in this study, based on the steady state of cell adhesion to the solid surface, we developed a multiple layer model to describe the structures of the cell-based Love mode acoustic wave devices. According to this multiple layer model, the transfer matrix method was used to determine the response of the device, including phase velocity and attenuation, to the changes in physical parameters in the wave-guiding layer, interfacial layer and cell layer. According to simulation results, it has been found that the sensitivity of the Love mode acoustic wave sensors are affected by the phase velocity of piezoelectric substrate, and the phase velocity, viscosity and thickness of wave-guiding layer. Therefore, our model can be used to optimize the device structure and direct the selection of materials for the device to obtain best performance. Experimentally, our results on the resonant frequency and insertion loss change with the thickness of PMMA wave guiding layer showed that our theoretical models were valid to describe the resonant frequency shift with loadings and insertion loss change induced by the loss of loading materials in the Love mode acoustic wave device. Furthermore, we showed that propagation velocity and attenuation shifts are sensitive to the properties and thickness of the interfacial layer and cell layer, especially interfacial layer, which means the Love mode acoustic wave devices provide potential tools to detect protein production, monitor cell adhesion. Since our theoretical model cannot describe the signal attenuation induced by energy loss in bulk

material, in the future, we will improve our theoretical models by considering this part of loss in them. In addition, we will perform the experimental studies on the use of Love mode acoustic wave devices to detect cell behaviors based on the modeling results discussed in this paper.

6.0 THE APPLICATION OF SOFT LITHOGRAPHY TECHNIQUES TO DETERMINE THE EFFECTS OF CELL SHAPE ON CELL STRUCTURES AND FUNCTIONS

6.1 INTRODUCTION

In chapter 3, 4 and 5, I discussed the application of thickness shear mode (TSM) acoustic wave sensors and Love mode acoustic wave sensors for cell biological studies. The other research areas that are critical to the development of cell-based biosensors are the controlling of cell function and fundamental studies of cell response to various hybrid interfaces.

In culture, cells attach to and spread on a substrate. Previous studies have shown that cell attachment and spreading is related to gene expression and protein production, implying a cell shape-based regulation of cellular function [39, 43, 112]. Understanding how cell shape influences cellular function is important to regulating cell phenotype and developing engineered tissues for medical applications [57, 113]. Therefore, in this chapter, I will discuss our research on the controlling of cell shape by soft lithography and determining the effects of cell shape on cell structure and function.

Soft lithography, a technique derived from microfabrication technology in the semiconductor industry, provides a powerful approach for studying cell shape or spreading in regulation of cell function [33, 39, 41, 114]. This technique allows fabrication of adhesive

patterns on the substrate at micro- to sub-micrometer scales. Confining cells to these adhesive patterns with various shapes and sizes can precisely control cell shape and spreading area. Micropatterning substrates by soft lithography overcomes the limitations of homogeneous unconfined adhesive substrates on which cells display various shapes even though they belong to the same cell type, which may partially alter their normal functions [115]. Using soft lithography, previous studies show that the degree of cell spreading influences DNA synthesis [39], proliferation and apoptosis [40, 41], and focal adhesion assembly [42] in human and bovine capillary endothelial cells; differentiation in mesenchymal stem cells [43]; and gene expression and protein synthesis in primary rat bone cells [44]. However, for a fixed spreading area, studies on cell shape regulation are mainly limited to cell motility, i.e., lamellipodia extension and direction of cell migration. For example, cells preferentially extended lamellipodia from their corners regardless of their geometric shapes [45, 46]. During migration, narrow teardrop-shaped or triangular cells moved predominantly toward the blunt end, while wide cells did not; rectangular cells migrated outward towards their two ends without bias for either one, but circular or square cells moved in random directions [33].

In this part of study, we aimed to determine the effect of cell shape on collagen expression in human tendon fibroblasts (HTFs). *In vivo*, tendon fibroblasts are highly elongated and are aligned along the longitudinal direction of the intact tendon, a well-organized fibrous connective tissue that is mainly composed of parallel collagen fibers [116]. By producing extracellular matrix (ECM) proteins, especially collagen type I, tendon fibroblasts serve to maintain, repair, and remodel the tendon matrix [55]. As such, synthesis of collagen type I is one major function of tendon fibroblasts. Therefore, the first aim of this study was to determine how this particular elongated cell shape is related to collagen type I expression in HTFs.

It is known that cells generate mechanical tension in their actin cytoskeleton and exert forces on cell-cell or cell-ECM contacts [77]. Tension in the actin cytoskeleton transmits to ECM via focal adhesions, and this force is termed as cell traction. The alterations in cell traction forces (CTFs) can result in change of cell shape [50, 76, 117]. Moreover, the physical connections between focal adhesions, actin cytoskeleton, and nuclear scaffold is thought to provide a pathway for mechanical signal transfer from cell surface to nucleus [50]. Therefore, the second aim of this study was to test the hypothesis that change of collagen type I expression in HTFs with various shapes is associated with alterations in the actin cytoskeletal structure and tension distribution. Specifically, we examined the distribution of actin cytoskeleton, focal adhesions, and CTFs in HTFs of various shapes and correlated them to the expression of collagen type I in these tendon cells.

6.2 MATERIALS AND METHODS

6.2.1 Fabrication of micropatterned substrates

Micropatterned substrates were fabricated by microcontact printing method according to the following procedures **(Figure 45)**. First, silicon masters were fabricated by using standard photolithography technologies. Negative photoresist SU-8 was spun on cleaned silicon wafer **(Figure 45a)**. The photoresist-coated silicon wafer was then exposed under UV light through the patterned photomask on Suss MA 6 mask aligner for 20 sec (SUSS MicroTec Inc., Santa Clara, CA) **(Figure 45b)**. The features were then developed, and the silicon master with the desired pattern was generated **(Figure 45c)**. In order to facilitate subsequent release of

Poly(dimethylsiloxane) (PDMS) from the silicon master, the template was oxidized in air plasma for 1 min and silanized with (tridecafluoro-1,1,2,2-tetrahydrooctyl)-1-trichlorosilane vapor overnight under vacuum. PDMS was then prepared by thoroughly mixing two silicone components, 601A and 601B (Wacker Chemical, Adrian, MI), in a weight ratio of 10:1, then slowly poured onto the silicon master (**Figure 45d**). After curing at room temperature for 24 hr, the PDMS was removed and cut to the desired size (**Figure 45e**). The substrate was prepared by the following procedures. The glass slides were cleaned and coated with 10 nm thick chromium and 20 nm thick gold (**Figure 45f**). The PDMS stamps were cleaned with ethanol and dried with a stream of pressurized air. A 2 mM ethanol solution of tris(ethylene glycol)-terminated alkanethiol ($HS(CH_2)_{11}(OCH_2CH_2)_3OH$, ProChimia, Poland) was put onto the stamp surface and incubated for 10 min, and the solution was then removed and the stamp was dried. The PDMS stamp was then gently pressed onto the slide (**Figure 45g**), and after 1 min, the stamp was removed from the glass substrate. A self-assembled monolayer was formed at the region where tris(ethylene glycol)-terminated alkanethiol was stamped (**Figure 45h**). The substrate was then rinsed with ethanol and dried with a steam of air. The self-assembled monolayer of tris(ethylene glycol)-terminated alkanethiol can resist the protein adsorption. Therefore, cells only adhere to the non-tris(ethylene glycol)-terminated alkanethiol-stamped region.

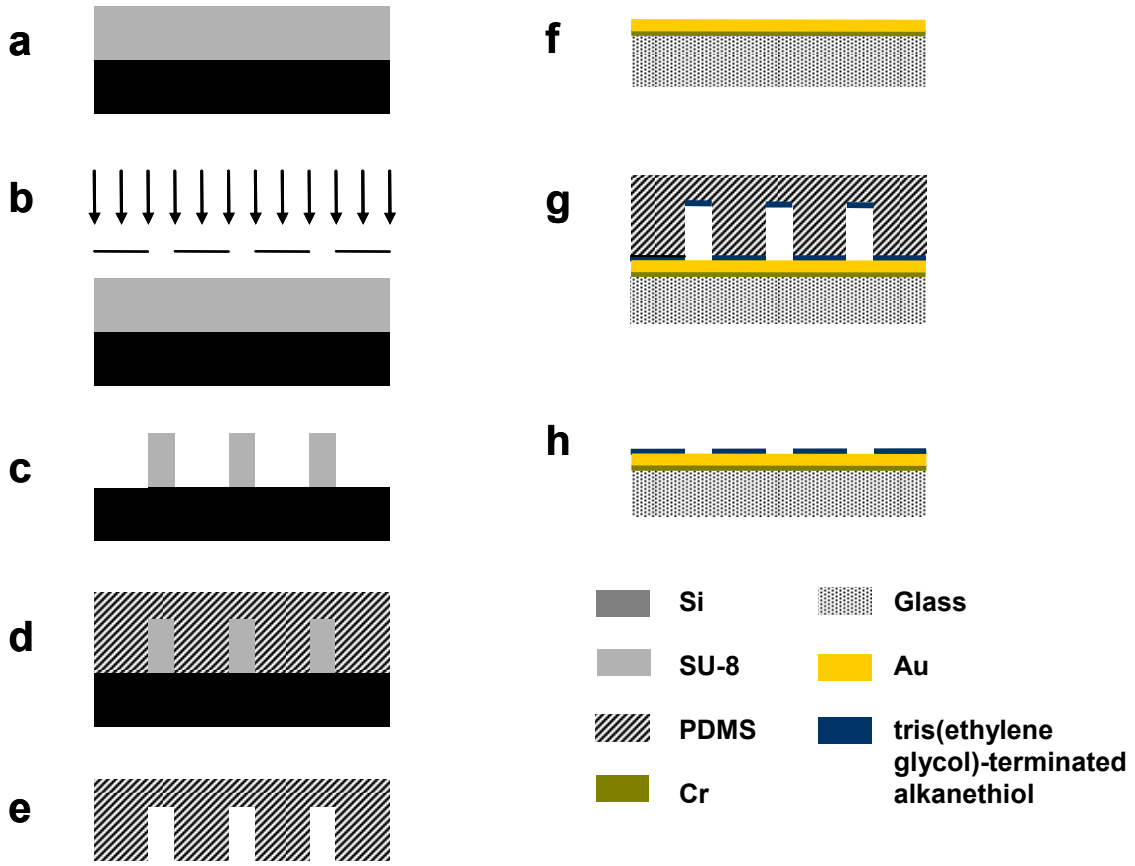

Figure 45. A schematic of microcontact printing method used for micropatterning gold surfaces in this study.

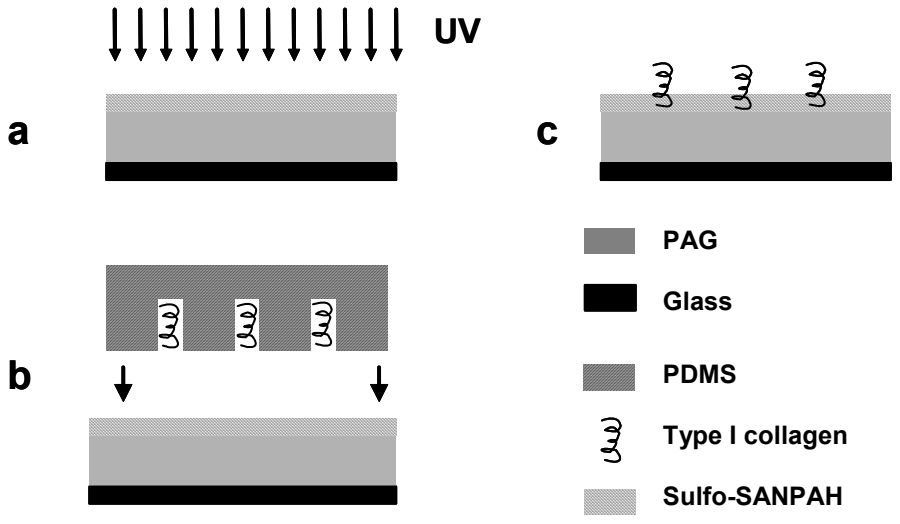

Figure 46. A schematic of microcontact printing method used for micropatterning PA gel in this study.

Microcontact printing method was also been used for fabrication of adhesive islands on polyacrylamide (PA) gel according to a method modified from the literature [118]. Briefly, after the PA gel was fully cross-linked, Sulfo-SANPAH (Pierce, Rockford, IL), a heterobifunctional cross-linker, was applied onto the gel surface and linked to the gel by exposing it to UV light (**Figure 46a**). The PDMS stamps were treated with oxygen plasma and then dipped in 100 μg/ml collagen type I solution (Angiotech Biomaterials, Palo Alto, CA). After carefully scraping the solution off the top surface of stamp, the stamp with the solution of collagen filled in the holes was gently pressed onto the PA gel overnight to allow conjugation of collagen type I to PA gel surface (**Figure 46b**). The stamp was removed from gel surface and the gel was then rinsed with PBS prior to cell seeding (**Figure 46c**).

6.2.2 Cell culture experiments

Human tendon fibroblast culture was established according to the published protocol [119]. For immunofluorescence assays, human tendon fibroblasts (HTFs) were seeded onto patterned gold-coated glass slides in cell growth medium (DMEM, 10% FBS and 1% penicillin/streptomycin). After HTFs (passage 5 or 6) were cultured on the patterned surface for 36 hrs, cells were fixed with 4% paraformaldehyde and then proceeded for immunostaining. For measuring CTFs, after collagen type I was patterned onto the PAG, 3000 HTFs were plated onto each gel disk in DMEM with 1% FBS and 1% penicillin/ streptomycin. Non-adhered cells were removed 1 hr later, and fresh cell growth medium was added. Cells were then allowed to spread on PAG for 6 hr prior to image acquisition for CTF measurement. During cell culture, cells were maintained at 37 ^{o}C in humidified atmosphere with 95% air and 5% carbon dioxide.

6.2.3 Immunofluorescence assays for collagen type I, GAPDH, actin filaments, and vinculin

Collagen type I, actin filaments, vinculin, and glyceraldehyde 3-phosphate dehydrogenase (GAPDH) were stained using the following protocols. Cells were fixed in 4% paraformaldehyde (FD NeuroTechnologies, Ellicott City, MD) for 15 min and then blocked with a Blotto buffer (4% dry milk and 0.4% Triton X-100 in PBS) for 45 min. For staining collagen type I and GAPDH, the sample was incubated with goat polyclonal anti-type I collagen antibody (Santa Cruz Biotechnology, Santa Cruz, CA) overnight or monoclonal antibody for GAPDH (Biogenesis, UK) for 1h with a dilution ratio 1:100 and 1:300, respectively, and then washed with block solutions. FITC-conjugated donkey anti-goat antibodies (Santa Cruz Biotechnology, Santa Cruz, CA) were then applied at a dilution ratio of 1:250 for 1 hr. The sample was washed extensively with block solutions and PBS to remove excess antibody. A FAK100 kit (Chemicon International, Temecula, CA) was used to stain actin filaments and vinculin. Samples were incubated with anti-vinculin with a dilution ratio 1:100 for 1 hr after cells were fixed and blocked with a Blotto buffer. After samples were washed with block solutions, secondary antibody (goat anti-mouse, FITC-conjugated, dilution 1:200) and TRITC-conjugated phalloidin (dilution 1:200) were applied simultaneously for 1 hr at room temperature. Cell nuclei were then stained with DAPI. Afterward, the sample was mounted and examined using fluorescence microscope or laser confocal microscope.

6.2.4 Cell traction force microscopy (CTFM)

The determination of CTFs by CTFM was described previously [116]. It is based on the deformations in the surface of a thin elastic substrate induced by cells cultured on it. The

fluorescent beads embedded in a thin PAG serve as markers for determining substrate displacements by image analysis, which are then used to compute CTFs based on continuum mechanics [76].

The PAG embedded with 0.5 μm red fluorescent micro-beads (Molecular Probes, Eugene, OR) was prepared first. The gel disk was 120 μm in thickness, 10 mm in diameter, and attached to the bottom of a 35 mm dish (MatTek, Ashland, MA), which had a circular glass area with a diameter of 14 mm. The gel stiffness was controlled by changing the relative concentration of acrylamide (Sigma, St. Louis, MO) and N, N'-methylenebisacrylamide (bis-acrylamide, Sigma, St. Louis, MO). In this study, gel containing 5% acrylamide and 0.1% bis-acrylamide with a Young's modulus of 3 kPa and a Poisson's ratio of 0.48 was used [57]. After collagen type I was patterned onto the PAG using microcontact printing method and HTFs were cultured on those gels for 6 h, phase contrast images of individual cells that were fully spread on single collagen-coated islands and fluorescence images of the embedded fluorescent beads were taken. After cells on the gel disk were trypsinized, fluorescence images of the fluorescent beads in the same view were taken. The CTFs were then computed using a MATLAB program based on a published method [116].

6.2.5 Quantification of collagen type I expression levels

The total collagen type I expression level per cell was quantified as follows. The immunofluorescence microscopy images of cells with different shapes were taken under the same conditions, including the same exposure time and gain factor. Cells that were fully spread on entire islands, as confirmed by phase contrast images, were selected for analysis. Using the image analysis software, (MetaMorph software. Molecular Devices, Sunnyvale, CA), the

boundary of the chosen cell was defined manually first. The intensities per pixel in fluorescence microscopy image were automatically measured and the average intensity over the defined cell area was computed. To subtract the background noise, we defined four small areas near cell boundary. By subtracting the average intensity over these the four small areas, we obtained the immunofluorescence intensity level for each chosen cell. A total of 20 cells from each group were chosen for measurement. To verify that cell shape affected the collagen type I synthesis, we also performed immunocytochemistry for GAPDH and measured its fluorescence intensity of each cell for four different shapes.

6.2.6 Statistical analysis

A one-way analysis of variance (ANOVA) was used to analyze the effect of cell shape on collagen type I expression level and CTF magnitude, followed by Duncan's test for multiple comparisons with the significance level set at $\alpha = 0.05$.

6.3 RESULTS

6.3.1 Micropatterning human tendon fibroblasts with different shapes

Micropatterned substrates containing an array of cell-adhesive islands surrounded by PEG-covered non-adhesive regions were fabricated using microcontact printing technique. The adhesive islands were designed to be of the same area (1.96×10^3 μm^2) but in different geometric forms (rectangular with aspect ratios of 19.6, 4.9 and 2.2, respectively, and circular). This area is

comparable with typical spreading area of human tendon fibroblasts (HTFs) on a smooth surface. To prevent cells from spreading across multiple islands, the non-adhesive spacing between islands was designed to be 50 μm. When HTFs were seeded onto the patterned substrates, they preferentially attached to adhesive islands and were confined within the boundaries of these islands. Therefore, the shape of cells was as precisely controlled as that of adhesive islands (**Fig. 47A**). In order to measure traction forces of micropatterned cells, type I collagen-coated adhesive islands on PAGs were fabricated. The shape of cells was seen to be well controlled on PAG surface (**Fig. 47B**).

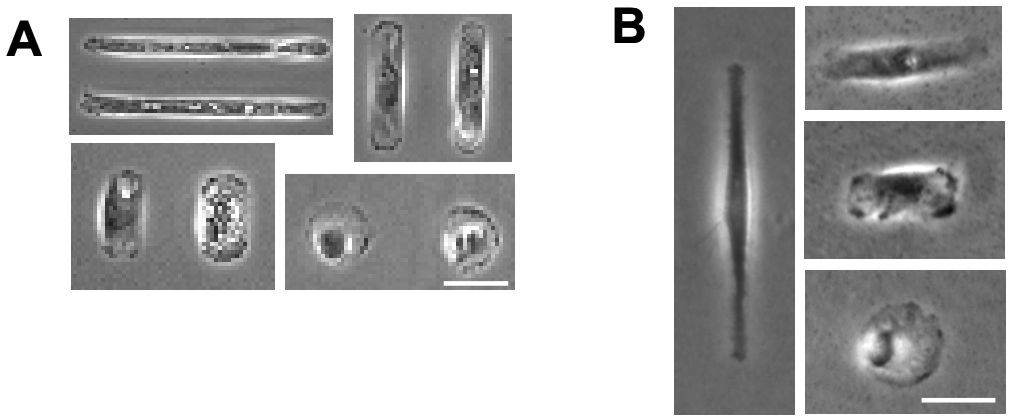

Figure 47. HTFs on (A) Micropatterned gold-coated substrates and (B) micropatterned polyacrylamide gel. (Scale bars: 50 μm).

6.3.2 Expression levels of collagen type I in micropatterned HTFs

Expression of collagen type I in HTFs with different shapes was determined by immunofluorescence assay. The fluorescence microscopy images of collagen type I for cells with different shapes **(Fig. 48**) showed that fluorescence intensity decreased with decreasing the aspect ratio of cells. This observation was confirmed by quantification by using image analysis

(Fig. 49). Compared to rectangular cells with an aspect ratio of 19.6 (i.e. the most elongated cells), cells with an aspect ratio of 4.9 expressed about 10% lower collagen type I, while cells with an aspect ratio of 2.2 expressed more than 20% lower. For circular cells, whose aspect ratio is 1, the collagen expression was 40% lower than that of the most elongated cells with an aspect ratio of 19.6. However, we found that GAPDH expression levels were not significantly different among cells with the four shapes (data not shown).

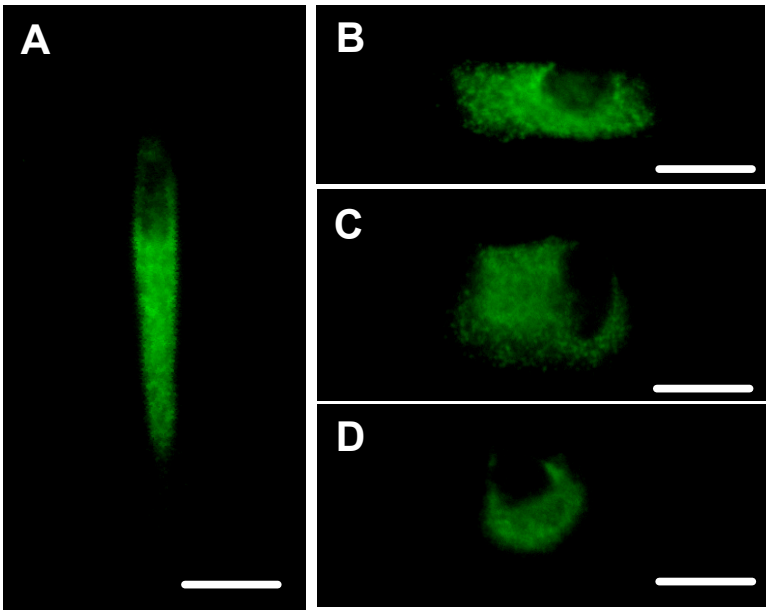

Figure 48. Immunofluorescence microscopy images of collagen type I expression in rectangular HTFs with aspect ratios of 19.6 (A), 4.9 (B), and 2.2 (C), respectively, and circular HTF (D). (Scale bars: 20 μm).

6.3.3 Organization of actin filaments and focal adhesions in micropatterned HTFs

Long and parallel actin filament bundles were formed in elongated cells, with aspect ratios of 19.6 and 4.9, respectively, along the longitudinal direction, while in short cells with an aspect ratio of 2.2 and circular cells, they were along the circumference of cells, and several bundles

were formed from the nuclear area to the edge of cells **(Figure 49)**. Focal adhesions, revealed by staining vinculin, were concentrated at the two ends of elongated cells or corners of short cells. In circular cells, however, focal adhesions were uniformly distributed along the edge of cell. Merged images of F-actin and vinculin showed that F-actin filaments (or stress fibers) at their ends linked with focal adhesions, where cells anchor to underlying substrate and hence exert traction forces.

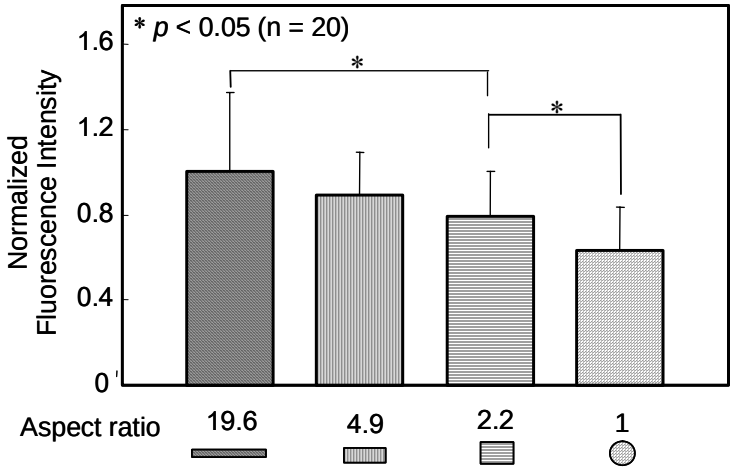

Figure 49. Effect of cell shape on collagen type I expression level.

6.3.4 Cell traction forces in micropatterned HTFs

For all cells examined in this study, the largest CTFs were located at the two ends of elongated cells, at the corner regions of short cells, and along the outer edge of the circular cells. The traction force directions appeared to be parallel to stress fibers. For example, the directions of the largest CTFs were in parallel to the long axis in elongated cells, along the diagonal in short cells, and along the radial in circular cells **(Fig. 50)**. The magnitude of CTFs decreased with increasing the aspect ratio of cell shape (**Fig. 51**).

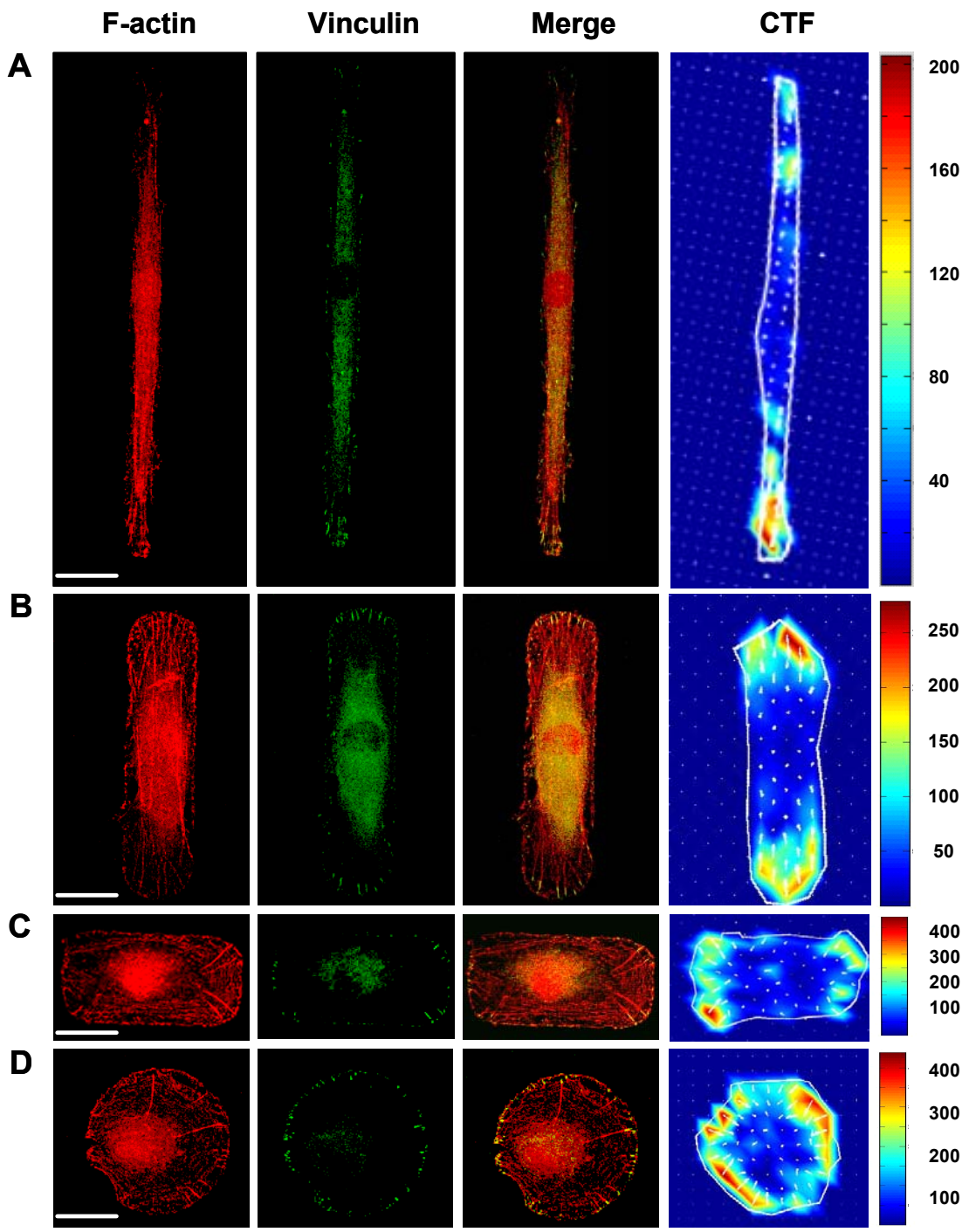

Figure 50. Immunofluorescence microscopy images of F-actin, vinculin, and the overlay of them, as well as CTFs in micropatterned HTFs. A-C. Rectangular HTFs with aspect ratios of 19.6, 4.9, and 2.2, respectively; D circular HTF. (Scale bars: 20 μm).

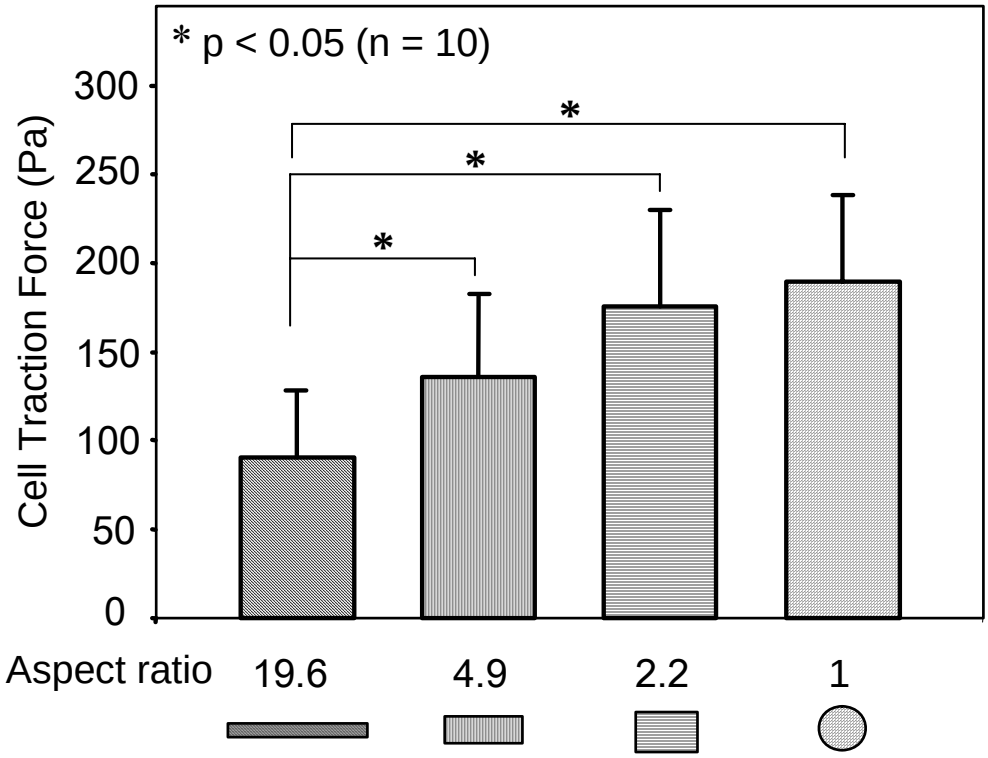

Figure 51. The effect of cell shape on CTF magnitude. It increased with decreasing aspect ratio of the cell.

6.4 DISCUSSION

Micropatterned substrates allow us to control the shape and projection area of cells precisely. As shown in this study, human tendon cells can be confined on micropatterned adhesive islands of any shape and size as desired. Therefore, micropatterned cell-adhesive surface provides an ideal experimental platform for studying functions of cells that have specific shapes *in vivo* at whole cell and sub-cellular levels [34]. Moreover, precisely controlling cell shape reduces cell variability as opposed to a cell population such that the biological response of the single cell can be investigated, instead of "averaged response" of a heterogeneous cell population. For example, micropatterned substrates have been used to create cell-based sensors in which cells exhibit a

more reproducible and defined phenotype [67, 120]. It should be noted that, however, while micropatterning technology can control cell shape precisely and therefore creates a more uniform cell group compared to cells on non-micropatterned surfaces, it cannot control cell cycle; in other words, these micropatterned cells may be in different cell cycles; as a result, these micropatterned cells can still differ in their functions.

In vivo, tendon cells, which are aligned with the collagen fibers in the longitudinal direction of the tendons, are highly elongated in shape [116]. By producing collagen type I and other matrix proteins, tendon cells *in vivo* function to maintain, repair, and remodel tendon matrix [119]. Using micropatterned HTFs, this study was able to show collagen type I expression levels at single cell level. Furthermore, collagen type I expression was the highest in the most elongated cells, which have shape most similar to those tendon cells *in vivo*, suggesting that normal tendon fibroblasts *in vivo* have an "optimal shape" for maximizing synthesis of type I collagen, a major function of these cells. For those HTFs assuming circular shape, their collagen type I expression levels were, on average, only ~65% compared to that of those elongated cells. The reduction in collagen expression in tendon cells of circular shape may contribute to the development of tendinopathy (Wang et al. 2006). Based on these data, it is also tempting to suggest that these circular cells may behave like fibrocartilage cells, as they are round *in vivo* and are known to produce low level of collagen type I but high level of collagen type II instead [34, 121].

An immediate question is: How does cell shape link to the biochemical process of protein synthesis in a cell? It is known that mechanical stresses generated by cells within cytoskeleton play important roles in the control of cell shape as well as cell function [50, 117]. Many signaling molecules bind to the cytoskeleton and/or link with integrins at focal adhesion

complexes, both of which are highly mechanical deformation-sensitive [43, 122-124]. Therefore, deformation in cytoskeleton, regulated by the mechanical stresses in it, provides a physical basis for transducing mechanical signals into biochemical signals [125]. In addition, because of the physical linkage between cytoskeleton (e.g. intermediate filaments) and nuclear matrix, deformation of nuclear matrix caused by cytoskeleton reorganization will alter DNA topography and transcription and consequently affect cell functions, such as gene expression and protein synthesis [123].

Besides the cytoskeleton, cell-generated cytoskeletal tension influences cell fate and functions [43, 51]. The changes in cell-generated forces have been shown to be responsible for the effect of cell spreading area on cell proliferation [39, 41, 126]. Cells with larger spreading area generate stronger tension and have an enhanced ability to proliferate [39, 41, 46]. Tension in the cytoskeleton has also been shown to be critical in the commitment of human mesenchymal stem cells into adipocyte or osteoblast lineages [43]. Using cells populated in collagen gels, Agarwal et al. showed that higher contraction was related to higher levels of collagen production in fibroblasts [127]. In this study, we found that changes in cell shape resulted in different organizations in cytoskeletal structures and altered the direction and spatial CTF distribution. This may be responsible for our finding that tendon cells with various aspect ratios expressed different levels of collagen type I. In addition, given the fact that cells can use traction forces to reorganize collagen fibers [128, 129] and elongated cells produced traction forces along their long axis, we speculate that this may be one reason why these elongated tendon cells produce aligned collagen matrix in vivo and in vitro [116].

In this study, we have also demonstrated that cell shape, controlled by micropatterned adhesive islands on substrate, influenced spatial distribution of actin cytoskeleton, focal

adhesions, and direction and spatial CTF distribution. The mechanisms by which cell shape alters actin filament organization and spatial arrangement of focal adhesions and traction forces might be due to the regulation of mechanical signals from the ECM-coated islands with various shapes during cell spreading. As shown in this study, the largest traction stresses occurred at the two ends of highly elongated rectangular cells, at corners of shortened rectangular cells, or around the edge of circular cells. These mechanical stresses may promote integrin clustering and focal adhesion complex formation, resulting in cytoskeletal realignment in the formation of bundles of contractile stress fibers along the directions of stresses stretching from focal adhesions, as well as recruitment of myosin to generate cell contraction [115, 117]. Finally, cells establish a stabilized structure of cytoskeleton and focal adhesions against ECM and achieve force balance between cells and ECM. Physical connections between integrins, cytoskeletal filaments, and nuclear scaffolds, which have been observed in our immunostaining results and also demonstrated in previous studies [50, 117], may provide a pathway for the mechanical signal transfer throughout cells, thereby producing integrated changes in cellular structure in response to changes in cell-ECM adhesion [123]. However, the exact molecular mechanisms that are responsible for cell shape-regulated cellular function seen in this study are not known. It could be that alterations in CTFs and other physical effects resulting from the imposed shape serve as the actual signals that trigger a cascade of molecular events leading to changes of cellular function. Further studies are required to control cell cycle and probe those molecular signals that account for alteration of cellular function with different shapes.

In summary, using micropatterning techniques, we have investigated the effect of cell shape on the level of collagen type I expression as well as on the changes of actin cytoskeleton, focal adhesions, and CTFs. We have shown that elongated tendon cells expressed higher

collagen type I than those shorter cells even though cell spreading area was constant, indicating tendon cells *in vivo*, which assume an elongated shape in normal tendons, has an "optimal shape" to perform their major function, that is, to synthesize collagen type I. We have also shown that changes in cell shape induced alterations in actin cytoskeletal structure, spatial arrangement of focal adhesions, direction and spatial distribution of traction forces in tendon cells, which may collectively affect the observed differential collagen type I expression in tendon cells with different shapes. Future studies are necessary to investigate the molecular signaling events that are responsible for cell shape-regulated cellular function.

7.0 CONCLUDING REMAKS

The research in this dissertation is focused on investigating the cell biological applications of acoustic wave sensors and the effects of cell shape on cell structure and function. Both of these two parts of research are very important to the realization of cell-based biosensors in various applications.

The thickness shear mode acoustic wave cytosensor system is developed to monitor the procedure of cell attachment, spreading and formation of focal adhesion to solid surface after cells added into the cell medium and cell detachment under cytoskeleton disruption, and to characterize the viscoelastic properties of cell monolayer after cell adhesion to sensor surface reaches the steady state. This part of work includes theoretical modeling, design of the sensor system and the experimental studies for biological application of this sensor system. Our studies expanded the cell biological applications of thickness shear mode acoustic wave sensors.

It has been recognized that acoustic wave devices with a higher operation frequency have a higher sensitivity. Surface acoustic wave devices are able to obtain high frequency more easily than bulk acoustic wave devices. Therefore, in this dissertation, besides the bulk acoustic wave sensors, we studied the surface acoustic wave sensors. Our studies are focused on the theoretical modeling of Love mode surface acoustic wave biosensors. Basically, we developed a theoretical model to describe how electrical signals of the Love mode acoustic wave sensors change with various multilayer loadings. Our experimental results demonstrated the validity of

our model. Through our theoretical models, we discussed how to optimize the design of Love mode acoustic wave sensors in order to obtain high sensitivity and predicted the electrical signal change when the surface of the device is attached with a cell layer. This part of research is critical to the future experimental studies of Love mode acoustic wave devices as cell-based biosensors.

In terms of the studies on controlling cell function, we precisely controlled cell shape using soft lithography, which is a technique derived from the microfabrication technology. By micro-patterning cells, we studied the effects of cell shape on cytoskeleton structure, focal adhesion morphology, cell traction force and protein synthesis by cells. This part of research is critical to improving the sensitivity and reliability of cell-based biosensors and developing engineered tissues for biomedical applications.

7.1 SUMMATY OF ACCOMPLISHMENTS

The primary accomplishments of this dissertation are listed below.

- Theoretical models of uniform cell monolayer and non-uniform cell adhesion to the thickness shear mode resonator were developed. These models first time predict the relationship between the electrical signals of the device (resonate frequency, motional resistance and electrical impedance or admittance) and mechanical properties and thickness of the interfacial layer and the cell layer. They are critical to explaining the experimental data, which allows us to obtain more information on cell-substrate contact and cell viscoelasticity. In addition, using these theoretical models, we first time characterized the viscoelasticity of cell monolayer by thickness shear mode acoustic wave sensors.

- The procedure of cell attachment, spreading and formation of focal adhesion with different cell seeding densities to solid surface is monitored by using the thickness shear mode acoustic wave sensor system. Our results showed that thickness shear mode acoustic wave devices could be used to monitor the procedure of cell attachment and spreading. The alterations in viscoelastic properties and cell-substrate contact during the formation of focal adhesion can be detected by the thickness shear mode sensors also.
- Changes in cell adhesion with cytoskeleton disruption are investigated using the thickness shear mode acoustic wave cytosensor system. Our results showed that changes in motional resistance are dependent on the concentration of cytochalasin D, which demonstrated that the thickness shear mode sensors can be used to quantify the effect of drug on cell behaviors.
- The viscoelastic properties of cell monolayer are determined based on the theoretical model of the uniform cell adhesion and curve-fitting algorithmic strategy. Our research first time demonstrated that thickness shear mode acoustic wave sensor provided a reliable tool to characterized cell viscoelasticity in a non-invasive, fast and simple way.
- A theoretical model of the Love mode surface acoustic wave sensor to predict the changes in phase velocity and loss in the acoustic waves with the thickness and viscoelasticity of loading layers is developed. Our experimental studies demonstrated the validity of our model. Based on the theoretical model, the wave-guiding layer can be optimized to obtain the high sensitivity of the device. Changes in phase velocity and loss of the acoustic waves in the wave-guided shear-horizontal surface acoustic wave sensor with cell monolayer adhesion are predicted based on the theoretical model. This part of research will be critial to the future experimental studies on Love mode acoustic wave sensors for cell biological applications.

- Adhesive proteins are micro-patterned on various substrates by soft lithography techniques. The effect of cell shape on cytoskeleton structure, focal adhesion morphology, cell traction force and protein synthesis is investigated experimentally. It has been found that the elongated tendon cells express higher collagen type I than those shorter cells even though cell spreading are is constant. It has also shown that changes in cell shape induced alterations in cytoskeleton structure, spatial arrangement of focal adhesions, traction forces in tendon cells, which may collectively affect the observed differential collagen type I expression in tendon cells with different shapes. The techniques of controlling cell shape on various substrates can be used in the development of cell-based biosensors in the future. The regulation mechanism of cell shape on cell function provides design criteria for the development of cell-based biosensors to preserve the biological response of interests.

7.2 FUTURE PERSPECTIVE

The work on the TSM devices for characterizing cell mechanical properties could be continued in the future. Based on our current model for cells adhered to the TSM resonator, there are too many unknown parameters in this model. Therefore, I propose to combine the TSM resonator with electric cell-substrate impedance sensing or surface plasmon resonance technology to measure the cell-substrate interaction, which will help us obtain enough information for extracting cell mechanical properties. This sensor system could be used for characterizing mechanical properties for different cell lines, normal or diseased cells and cells under various biological environments, which have potential applications in biomedical research, drug screening etc.

According to our current results, the Love mode acoustic wave devices could be used for measuring the interfacial layer between cells and substrate. It is expected that this device can be used to monitor the assembling of cell focal adhesion and extracellualr matrix production in real time, which is critical in the physiological and pathological processes.

Based on our previous studies, we demonstrated that understanding the relationship between cell shape and cellular function is important for study of cell biology in general and for regulation of cell phenotype in tissue engineering in particular. In the future work, cell shape will be controlled using soft lithography on the sensor surface; therefore, the effect of cell shape on cell behaviors can be studied using our sensor systems. The results will be compared with those by conventional biological techniques, such as immunoassaying, western blot etc. Compared with those conventional biological techniques, the sensor system has advantages of fast, simple, real-time and quantitative in measurements.

BIBLIOGRAPHY

1. Schultz, J., et al., *WTEC Panel Report on INTERNATIONAL RESEARCH AND DEVELOPMENT IN BIOSENSING.* 2004.

2. Ballantine, D.S. and R.M. White, *Acoustic Wave Sensors: Theory, Design, and Physico-Chemical Applications.*

3. Li, Z., *Guided shear-horizontal surface acoustic wave (SH-SAW) chemical sensors for detection of organic contaminants in aqueous environments. Ph.D thesis.* 2005.

4. Bunde, R.L. and E.J. Jarvi, *Piezoelectric quartz crystal biosensors.* Talanta., 1998. **46**: p. 1223-1236.

5. Rogers, K.R.a.C.L.G., *Environmental Biosensors: A Status Report.* http://pubs.acs.org/hotartcl/est/96/nov/envir.html.

6. Beck, K., et al., *Contactless surface acoustic wave gas sensor* Sensors and actuators A: Physical, 1999. **76**(1-3): p. 103-106.

7. Cheeke, J., N. Tashtoush, and N. Eddy, *Surface Acoustic Wave Humidity Sensor Based on the Changes in the Viscoelastic Properties of a Polymer Film.* Proc Ultrasonics Symposium, , 1996. **1**: p. 449-452.

8. Thompson, M., Stone, D. C., *Surface-launched acoustic wave sensors: chemical sensing and thin film characterization.*

9. Larson, P.H., *The Use of Piezoelectric Material in Creating Adaptive Shell Structures." Ph. D. thesis.* 1994.

10. Herrmann, F. and B. Jakoby, *Microacoustic sensors for liquid monitoring.* sensor update 2001. **9**: p. 105-160.

11. Vellekoop, M.J. and A.J. Van Rhijn, *All-silicon plate wave oscillator system for sensors.* Sensor and actuators A, 1991. **27**: p. 699-703.

12. Lucklum, R. and P. Hauptmann, *Transduction mechanism of acoustic-wave based chemical and biochemical sensors.* Meas. Sci. Technol, 2003. **14**: p. 1854-1864.

13. Berzina, T.S., L. Piras, and V.I. Troitsky, *Study of horseradish peroxidase activity in alternate-layer Langmuir–Blodgett films.* Thin Solid Films, 1998. **327–329** p. 621-626.

14. Rickert, J., A. Brecht, and W. Gopel, *Quartz crystal microbalances for quantitative biosensing and characterizing protein multilayers.* Biosens. Bioelectron. , 1997. **12**: p. 567–575.

15. Lvov, Y., et al., *Formation of ultrathin multilayer and hydrated gel from montmorillonite and linear polycations.* Langmuir, 1996. **12**: p. 3038–3044.

16. Ko¨nig, B. and M. Gra¨tzel, *A quartz crystal microbalance assay for detection of antibodies against the recombinant African swine fever virus attachment protein p12 in swine serum.* Anal. Chem., 1994. **66**: p. 341–344.

17. Koenig, B. and M. Graetzel, *A novel immunosensor for herpes viruses.* Anal. Chem. , 1994. **66**: p. 341-344.

18. Nakanishi, K., H. Muguruma, and I. Karube, *A novel method of immobilizing antibodies on a quartz crystal microbalance using plasma-polymerized films for immunosensors.* Anal. Chem. , 1998. **68**: p. 1695–1700.

19. Carter, R.M., et al., *Quartz crystal microbalance detection of Vibrio cholerae O139 serotype.* J. Immunol. Methods 1995. **187**: p. 121–125.

20. Fredriksson, C., et al., *The piezoelectric quartz crystal mass and dissipation sensor: a means of studying cell adhesion.* Langmuir 1998. **14**(2): p. 248 -251. .

21. Zhou, T., et al., *The quartz crystal microbalance as a continuous monitoring tool for the study of endothelial cell surface attachment and growth.* Biotechnology Progress, 2000. **16**(2): p. 268-277.

22. Marx, K.A., et al., *Quartz crystal microbalance study of endothelial cell number dependent differences in initial adhesion and steady-state behavior: evidence for cell-cell cooperativity in initial adhesion and spreading.* Biotechnology Progress, 2003. **19**: p. 987-999.

23. Wegener, J., et al., *Analysis of the composite response of shear wave resonators to the attachment of mammalian cells.* Biophysical Journal, 2000 **78**: p. 2821–2833.

24. Redepenning, J., et al., *Osteoblast attachment monitored with a quartz crystal microbalance.* Anal Chem, 1993. **65**(23): p. 3378-81.

25. Wegener, J. and A. Janshoff, *Cell adhesion monitoring using a quartz crystal microbalance: comparative analysis of different mammalian cell lines.* The European Biophysics Journal, 1998. **28**: p. 26-37.

26. Kalantar-Zadeh, K., et al., *A Novel Love mode surface acoustic wave based immunosensors.* Sensors and Actuators B: Chemical, 2003. **91**(143-147).

27. McHale, G., M.I. Newton, and F. Martin, *Theoretical mass sensitivity of Love wave and layer guided acoustic plate mode sensors.* J. Appl. Phys., 2002. **91**(12): p. 9701-9710.

28. Li, Z., et al., *Design Considerations for High Sensitivity Guided SH-SAW Chemical Sensor for Detection in Aqueous Environments.* 2004 IEEE International Ultrasonics, Ferroelectrics, and Frequency Control Joint 50th Anniversary Conference, 2004: p. 185-192.

29. Martin', S.J. and G.C. Frye, *Dynamics and Response of Polymer-Coated Surface Acoustic Wave Devices: Effect of Viscoelastic Properties and Film Resonance.* Anal. Chem., 1994. **66**: p. 2201-2219.

30. Oliner, A.A., *Microwave network methods for guided elastic waves.* IEEE Transactions on microwave theory and techniques, 1969. **MTT-17**(11): p. 812-826.

31. Francis, L.A., *Thin film acoustic waveguides and resonators for gravimetric sensing applications in liquid.* Ph. D. Thesis, Universit´e catholique de Louvain, Louvain-la-Neuve, Belgium, 2006.

32. Xia, Y. and G.M. Whitesides, *Soft lithography.* Annu. Rev. Mater. Sci., 1998. **28**: p. 153-84.

33. Whitesides, G.M., et al., *Soft lithography in biology and biochemistry.* Annu Rev Biomed Eng, 2001. **3**: p. 335-73.

34. Lehnert, D., et al., *Cell behaviour on micropatterned substrata: limits of extracellular matrix geometry for spreading and adhesion.* J Cell Sci, 2004. **117**(Pt 1): p. 41-52.

35. Xia, Y., et al., *Complex Optical Surfaces Formed by Replica Molding Against Elastomeric Masters.* Science, 1996. **273**(5273): p. 347-9.

36. Kim, E., Y. Xia, and G.M. Whitesides, *Polymer microstructures formed by moulding in capillaries.* Nature, 1995. **376**: p. 581-584.

37. Joon, N.L., et al., *Patterning of dielectric oxide thin layers by microcontact printing of self-assembled monolayers.* J. Mat. Res., 1995. **10**: p. 2996-99.

38. Wang, D., et al., *Nanometer scale patterning and pattern transfer on amorphous Si, crystalline Si, and SiO2 surfaces using self-assembled monolayers.* Appl. Phys. Lett., 1997. **70**: p. 1593-95.

39. Singhvi, R., et al., *Engineering cell shape and function.* Science, 1994. **264**(5159): p. 696-8.

40. Chen, C.S., et al., *Micropatterned surfaces for control of cell shape, position, and function.* Biotechnol Prog, 1998. **14**(3): p. 356-63.

41. Chen, C.S., et al., *Geometric control of cell life and death.* Science, 1997. **276**(5317): p. 1425-8.

42. Chen, C.S., et al., *Cell shape provides global control of focal adhesion assembly.* Biochem Biophys Res Commun, 2003. **307**(2): p. 355-61.

43. McBeath, R., et al., *Cell shape, cytoskeletal tension, and RhoA regulate stem cell lineage commitment.* Dev Cell, 2004. **6**(4): p. 483-95.

44. Thomas, C.H., et al., *Engineering gene expression and protein synthesis by modulation of nuclear shape.* Proc Natl Acad Sci U S A, 2002. **99**(4): p. 1972-7.

45. Brock, A., et al., *Geometric determinants of directional cell motility revealed using microcontact printing.* Langmuir, 2003. **19**(5): p. 1611-7.

46. Parker, K.K., et al., *Directional control of lamellipodia extension by constraining cell shape and orienting cell tractional forces.* Faseb J, 2002. **16**(10): p. 1195-204.

47. Bray, D., *Cell Movements.* 1992.

48. Lodish, H. and D. Baltimore, *Molecular Cell Biology.* 1995.

49. Ingber, D.E., *Tensegrity I. Cell structure and hierarchical systems biology.* J Cell Sci, 2003. **116**(Pt 7): p. 1157-73.

50. Maniotis, A.J., C.S. Chen, and D.E. Ingber, *Demonstration of mechanical connections between integrins, cytoskeletal filaments, and nucleoplasm that stabilize nuclear structure.* Proc Natl Acad Sci U S A, 1997. **94**(3): p. 849-54.

51. Wang, N., et al., *Mechanical behavior in living cells consistent with the tensegrity model.* Proc Natl Acad Sci U S A, 2001. **98**(14): p. 7765-70.

52. Ingber, D.E., *The riddle of morphogenesis: a question of solution chemistry or molecular cell engineering?* Cell, 1993. **75**(7): p. 1249-52.

53. Ingber, D.E., *Tensegrity II. How structural networks influence cellular information processing networks.* J Cell Sci, 2003. **116**(Pt 8): p. 1397-408.

54. Agutter, P.S., *Cell mechanics and stress: from molecular details to the 'universal cell reaction' and hormesis.* Bioessays, 2007. **29**(4): p. 324-33.

55. Wang, J.H. and B.P. Thampatty, *An introductory review of cell mechanobiology.* Biomech Model Mechanobiol, 2006. **5**(1): p. 1-16.

56. Khatiwala, C.B. and S.R. Peyton, *The intrinsic mechanical properties of the extracellular matrix affect the behavior of preosteoblastic cells.* Am. J. Physiol., in press.

57. Liu, W.F. and C.S. Chen, *Cellular and multicellular form and function.* Adv Drug Deliv Rev, 2007. **59**(13): p. 1319-28.

58. Geiger, B. and A. Bershadsky, *Transmembrane extracelluar matrix-cytoskeleton crosstalk.* Nature review, 2001. **2**: p. 793.

59. Sniadecki, N.J. and R.A. Desai, *Nanotechnology for Cell–Substrate Interactions.* Annals of Biomedical Engineering, 2006. **34**(1): p. 59–74.

60. Murphy-Ullrich, J.E., *The de-adhesive activity of matricellular proteins: is intermediate cell adhesion an adaptive state?* J Clin Invest, 2001. **107**(7): p. 785-90.

61. Lo, C.-M. and J. Ferrier, *Impedance analysis of fibroblastic cell layers measured by electric cell-substrate impedance sensing.* Physical Review E., 1998. **57**(6): p. 6982-6987.

62. Lo, C.M., et al., *Cell-substrate separation: effect of applied force and temperature.* European Biophysics Journal 1998. **27**(1): p. 9-17.

63. *http://www.btxonline.com/products/ecis/.*

64. Yamada, S., D. Wirtz, and S.C. Kuo, *Mechanics of living cells measured by laser tracking microrheology.* Biophysical Journal, 2000. **78**(4): p. 1736-47.

65. Bausch, A.R., et al., *Local measurements of viscoelastic parameters of adherent cell surfaces by magnetic bead microrheometry.* Biophys J, 1998. **75**(4): p. 2038-49.

66. Maksym, G.N., et al., *Mechanical properties of cultured human airway smooth muscle cells from 0.05 to 0.4 Hz.* Journal of Applied Physiology 2000. **89**(4): p. 1619-32.

67. Park, S., et al., *Cell motility and local viscoelasticity of fibroblasts.* Biophys J, 2005. **89**(6): p. 4330-42.

68. Trepat, X., et al., *Viscoelasticity of human alveolar epithelial cells subjected to stretch.* Am J Physiol Lung Cell Mol Physiol, 2004. **287**(5): p. L1025-34.

69. Wu, Z.Z., et al., *Comparison of the viscoelastic properties of normal hepatocytes and hepatocellular carcinoma cells under cytoskeletal perturbation.* Biorheology, 2000. **37**(4): p. 279-90.

70. Loh, O., A. Vaziri, and H.D. Espinosa, *The Potential of MEMS for Advancing Experiments and Modeling in Cell Mechanics.* Experimental Mechanics, 2007. **DOI 10.1007/s11340-007-9099-8**.

71. Rand, R.P., *Mechanical Properties of the Red Cell Membrane. Ii. Viscoelastic Breakdown of the Membrane.* Biophys J, 1964. **4**: p. 303-16.

72. Suresh, S., et al., *Connections between single-cell biomechanics and human disease states: gastrointestinal cancer and malaria.* Acta Biomaterialia, 2005. **1**: p. 15-30.

73. Thoumine, O. and A. Ott, *Time scale dependent viscoelastic and contractile regimes in fibroblasts probed by microplate manipulation.* J Cell Sci, 1997. **110 (Pt 17)**: p. 2109-16.

74. Mahaffy, R.E., et al., *Quantitative analysis of the viscoelastic properties of thin regions of fibroblasts using atomic force microscopy.* Biophys J, 2004. **86**(3): p. 1777-93.

75. Fabry, B., et al., *Scaling the microrheology of living cells.* Phys Rev Lett, 2001. **87**(14): p. 148102.

76. Wang, J.H. and J.S. Lin, *Cell traction force and measurement methods.* Biomech Model Mechanobiol, 2007. **6**(6): p. 361-71.

77. Harris, A.K., D. Stopak, and P. Wild, *Fibroblast traction as a mechanism for collagen morphogenesis.* Nature, 1981. **290**(5803): p. 249–251.

78. Galbraith, C.G. and M.P. Sheetz, *A micromachined device provides a new bend on fibroblast traction forces.* Proc Natl Acad Sci USA, 1997. **94**(17): p. 9114–9118.

79. du Roure, O., et al., *Force mapping in epithelial cell migration.* Proc Natl Acad Sci U S A, 2005. **102**(7): p. 2390-5.

80. Tan, J.L., et al., *Cells lying on a bed of microneedles: an approach to isolate mechanical force.* Proc Natl Acad Sci U S A, 2003. **100**(4): p. 1484-9.

81. Munevar, S., Y. Wang, and M. Dembo, *Traction force microscopy of migrating normal and H-ras transformed 3T3 fibroblasts.* Biophys J, 2001. **80**(4): p. 1744-57.

82. Lee, J., *The use of gelatin substrates for traction force microscopy in rapidly moving cells.* Methods Cell Biol, 2007. **83**: p. 297-312.

83. Lombardi, M.L., et al., *Traction force microscopy in Dictyostelium reveals distinct roles for myosin II motor and actin-crosslinking activity in polarized cell movement.* J Cell Sci, 2007. **120**(Pt 9): p. 1624-34.

84. Kino, G.S., *Acoustic Waves: Devices, Imaging and Analog Signal Processing, Prentice-Hall Englewood Cliffs, NJ.* 1987.

85. Lucklum, R. and P. Hauptmann, *Generalized acoustic parameters of non-homogenous thin films.* 2002 IEEE international frequency control symposium and PDA exhibition, 2002: p. 234-241.

86. Rosenbaum, J.F., *Bulk Acoustic Wave Theory and Devices Artech House Publishers, Boston, MA.* 1988.

87. Chen, Q. and Q.-M. Wang, *The effective electromechanical coupling coefficient of piezoelectric thin film resonators.* Applied Physics Letters 2005. **86**: p. 022904

88. Behling, C., R. Lucklum, and P. Hauptmann, *The non-gravimetric quartz crystal resonator response and its application for polymer shear moduli determination.* Measurement Science and Technology, 1998. **9**: p. 1886-1893.

89. Lucklum, R., C. Behling, and P. Hauptmann, *Role of mass accumulation and viscoelastic film properties for the response of acoustic-wave-based chemical sensors* Analytical Chemistry, 1999. **71** p. 2488-2496.

90. Lucklum, R. and P. Hauptmann, *Transduction mechanism of acoustic-wave based chemical and biochemical sensors* Measurement Science and Technology 2003. **14**: p. 1854-1864.

91. Becker, W.M. and D.W. Deamer, *The World of the Cell, 2nd ed.* 1991.

92. Giebel, K., et al., *Imaging of cell/substrate contacts of living cells with surface plasmon resonance microscopy.* Biophysical Journal, 1999. **76**(1 Pt 1): p. 509-16.

93. Wu, H.W., T. Kuhn, and V.T. Moy, *Mechanical properties of L929 cells measured by atomic force microscopy: effects of anticytoskeletal drugs and membrane crosslinking.* Scanning, 1998. **20**(5): p. 389-97.

94. Girard, K.D., et al., *Dynacortin contributes to cortical viscoelasticity and helps define the shape changes of cytokinesis.* The EMBO Journal, 2004. **23**(7): p. 1536-46.

95. Sapper, A., J. Wegener, and A. Janshoff, *Cell motility probed by noise analysis of thickness shear mode resonators.* Analytical Chemistry, 2006. **78**(14): p. 5184-91.

96. Smith, B.A., et al., *Probing the viscoelastic behavior of cultured airway smooth muscle cells with atomic force microscopy: stiffening induced by contractile agonist.* Biophys J, 2005. **88**(4): p. 2994-3007.

97. Bausch, A.R., W. Moller, and E. Sackmann, *Measurement of local viscoelasticity and forces in living cells by magnetic tweezer.* Biophys. J. , 1999. **76**: p. 573-579.

98. Hochmuth, R.M., *Measuring the mechanical properties of individual human blood cells.* J Biomech Eng, 1993. **115**(4B): p. 515-9.

99. Felder, S. and E.L. Elson, *Mechanics of fibroblast locomotion: quantitative analysis of forces and motions at the leading lamellas of fibroblasts.* J. Cell. Biol. , 1990. **111**: p. 2513-252.

100. Petersen, N.O., W.B. McConnaughey, and E.L. Elson, *Dependence of locally measured cellular deformability on position on the cell, temperature, and cytochalasin B.* Proc Natl Acad Sci U S A, 1982. **79**(17): p. 5327-31.

101. Jimenez, Y., et al., *A contribution to solve the problem of coating properties extraction in quartz crystal microbalance applications.* IEEE Trans Ultrason Ferroelectr Freq Control, 2006. **53**(5): p. 1057-72.

102. Feneberg, W., M. Aepfelbacher, and E. Sackmann, *Microviscoelasticity of the apical cell surface of human umbilical vein endothelial cells (HUVEC) within confluent monolayers.* Biophys J, 2004. **87**(2): p. 1338-50.

103. Izzard, C.S. and L.R. Lochner, *Cell-to-substrate contacts in living fibroblasts: an interference reflexion study with an evaluation of the technique.* J Cell Sci, 1976. **21**(1): p. 129-59.

104. Alcaraz, J., et al., *Microrheology of human lung epithelial cells measured by atomic force microscopy.* Biophys J, 2003. **84**(3): p. 2071-9.

105. Srivastava, A. and G. Krishnamoorthy, *Cell type and spatial location dependence of cytoplasmic viscosity measured by time-resolved fluorescence microscopy.* Arch Biochem Biophys, 1997. **340**(2): p. 159-67.

106. Bicknese, S., et al., *Cytoplasmic viscosity near the cell plasma membrane: measurement by evanescent field frequency-domain microfluorimetry.* Biophys J, 1993. **65**(3): p. 1272-82.

107. Sato, M., et al., *Application of the micropipette technique to the measurements of cultured porcine aortic endothelial cell viscoelastic properties.* J. Biomech. Eng., 1990. **112**: p. 263-268.

108. Desprat, N., et al., *Creep function of a single living cell.* Biophys J, 2005. **88**(3): p. 2224-33.

109. Palmer, A., et al., *Diffusing wave spectroscopy microrheology of actin filament networks.* Biophys J, 1999. **76**(2): p. 1063-71.

110. Li, F., J.H. Wang, and Q.M. Wang, *Monitoring cell adhesion by using thickness shear mode acoustic wave sensors.* Biosens Bioelectron. , 2007. **23**(1): p. 42-50.

111. Harding, G.L., *Mass sensitivity of Love-mode acoustic sensors incorporating silicon dioxide and silicon-oxy-fluoride guiding layers.* Sensors and Actuators A, 2001. **88**: p. 20-18.

112. Lee, J.Y., et al., *Analysis of local tissue-specific gene expression in cellular micropatterns.* Anal Chem, 2006. **78**(24): p. 8305-12.

113. Langer, R. and J.P. Vacanti, *Tissue engineering.* Science, 1993. **260**(5110): p. 920-6.

114. Mrksich, M., et al., *Controlling cell attachment on contoured surfaces with self-assembled monolayers of alkanethiolates on gold.* Proc Natl Acad Sci U S A, 1996. **93**(20): p. 10775-8.

115. Thery, M., et al., *Cell distribution of stress fibres in response to the geometry of the adhesive environment.* Cell Motil Cytoskeleton, 2006. **63**(6): p. 341-55.

116. Hu, S., et al., *Intracellular stress tomography reveals stress focusing and structural anisotropy in cytoskeleton of living cells.* Am J Physiol Cell Physiol, 2003. **285**(5): p. C1082-90.

117. Chicurel, M.E., C.S. Chen, and D.E. Ingber, *Cellular control lies in the balance of forces.* Curr Opin Cell Biol, 1998. **10**(2): p. 232-9.

118. Engler, A.J., et al., *Myotubes differentiate optimally on substrates with tissue-like stiffness: pathological implications for soft or stiff microenvironments.* J Cell Biol, 2004. **166**(6): p. 877-87.

119. Li, B., et al., *Development of micropost force sensor array with culture experiments for determination of cell traction forces.* Cell Motil Cytoskeleton, 2007. **64**(7): p. 509-18.

120. Fujimoto, H., et al., *Fabrication of cell-based arrays using micropatterned alkanethiol monolayers for the parallel silencing of specific genes by small interfering RNA.* Bioconjug Chem, 2006. **17**(6): p. 1404-10.

121. Benjamin, M. and J.R. Ralphs, *Biology of fibrocartilage cells.* Int Rev Cytol, 2004. **233**: p. 1-45.

122. Geiger, B. and A. Bershadsky, *Exploring the neighborhood: adhesion-coupled cell mechanosensors.* Cell, 2002. **110**(2): p. 139-42.

123. Ingber, D.E., *Tensegrity: the architectural basis of cellular mechanotransduction.* Annu Rev Physiol, 1997. **59**: p. 575-99.

124. Zhu, C., G. Bao, and N. Wang, *Cell mechanics: mechanical response, cell adhesion, and molecular deformation.* Annu Rev Biomed Eng, 2000. **2**: p. 189-226.

125. Matthews, B.D., et al., *Mechanical properties of individual focal adhesions probed with a magnetic microneedle.* Biochem Biophys Res Commun, 2004. **313**(3): p. 758-64.

126. Wang, N., et al., *Micropatterning tractional forces in living cells.* Cell Motil Cytoskeleton, 2002. **52**(2): p. 97-106.

127. Agarwal, C., et al., *Healing and normal fibroblasts exhibit differential proliferation, collagen production, alpha-SMA expression, and contraction.* Ann Biomed Eng, 2006. **34**(4): p. 653-9.

128. Eastwood, M., et al., *Effect of precise mechanical loading on fibroblast populated collagen lattices: morphological changes.* Cell Motil Cytoskeleton, 1998. **40**(1): p. 13-21.

129. Huang, D., et al., *Mechanisms and dynamics of mechanical strengthening in ligament-equivalent fibroblast-populated collagen matrices.* Ann Biomed Eng, 1993. **21**(3): p. 289-305.